MICROWAVE MICROMACHINED CAVITY FILTERS

by

Lee Harle

A dissertation submitted in partial fulfillment
of the requirements for the degree of
Doctor of Philosophy
(Electrical Engineering)
in The University of Michigan
2003

Doctoral Committee:
Professor Linda P.B. Katehi, Chair
Professor Jessy W. Grizzle
Professor Kamal Sarabandi
Professor Kensall D. Wise

To my husband, Randall Leigh Beckner,

Fair winds and following seas.

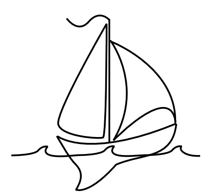

ACKNOWLEDGEMENTS

. . . I find frank acknowledgement of one's ignorance is not only the easiest way to get rid of a difficulty, but the likeliest way to obtain information, and therefore I practice it: I think it an honest policy. Those who affect to know every thing, and so undertake to explain every thing, often remain long ignorant of many things that others could and would instruct them in, if they appeared less conceited.

Benjamin Franklin

Frank acknowledgement of one's ignorance is just the first step, and must be followed by the difficult but rewarding cultivation of friendships and associations with colleagues, from which mutual benefit must arise. I have been blessed with many such associations while at the University of Michigan, and I hope that my associates have benefited from the relationships as much as I have. For in the end, that's what really matters.

I would first like to thank my advisor, Dean Linda P. B. Katehi, for her support, encouragement, and unfailing professionalism in the face of every assault. I appreciate her steadfast support of student groups such as Grad-SWE, and her acknowledgement of the important roles these groups play in strengthening the student community. I consider it a privilege to have known and worked with Linda, and I thank her for seeing me through to the end.

I also thank my dissertation committee, Prof. Jessy W. Grizzle, Prof. Kamal Sarabandi and Prof. Kensall D. Wise for their participation, support and feedback. I wish to acknowledge three other faculty: Prof. Tony England, Dean Stella Pang, and

Assistant Research Scientist Leland Pierce. Prof. England was a valuable teacher and mentor to me early in my tenure here, and I believe he is partly responsible for my continued presence in the program. I thank Dean Pang for her frankness and support, both as a teacher and as a Dean. Dr. Pierce was kind enough to read my thesis in its entirety, appendices included, in less than 24 hours upon receipt of same, and provide helpful suggestions for its improvement.

Recognition is also due to my mentors from my undergraduate days, Dr. Ken Lyons of Bell Laboratories and Prof. Steven Girvin of Indiana University, whose friendship, intelligence and thoughtful guidance inspired me to stick around for the Ph.D.

I would like to acknowledge the generous financial support that I have received in the course of my studies here at Michigan. I thank the Office of Naval Research (grant no. 00014-95-1-1299), the Department of Defense Research and Engineering and the Army Research Office (grant no. DOD-G-DAAH04-96-1-0377), the Jet Propulsion Laboratory's Center for Integrated Space Microsystems/System-on-a-Chip Project (grant no. 961301), and the U.S. Department of Education and Motorola Corp. for fellowship support. In particular, I would like to thank Dr. Marty Herman and Dr. Sam Valas of JPL for their continued support and feedback.

My experiences with the Graduate Committee of the Society of Women Engineers have made my time here most worthwhile and enjoyable. I hope that we have achieved some small but measurable improvement in the College of Engineering community. I wish my Grad-SWE friends the best of luck in their careers and in life: Amy, Tracy, Karla, Ksenia, both Stephanies, Joyce, Anna, Valerie, Jayshri, Carrie, Debby and Madhu. Good luck, Marissa. Grad-SWE could not exist without the continued support of the Women in Engineering office: Debbie Taylor, Sue Burke, Bonnie Curely and Dr. Cinda-Sue Davis. These women have never failed to give whatever was asked of them, and have always made themselves available whenever we called upon them for advice and direction.

Many thanks are due to the Rad Lab and department staff for their help and support over the years, most notably Beth Stalnaker and Karen Liska, as well as Dennis Grimard and the SSEL staff, without whom nothing would be possible.

I hope that the friends I have made while in Ann Arbor will continue for years to come. I wish them all the best of luck in everything that they do. For their friendship and support, both personal and professional, I would like to thank my friends and colleagues in what I fear will be a woefully incomplete list. For training and guidance, Rashaunda Henderson, Katherine Herrick, Jeremy Muldavin, and John Papapolymerou. For valuable advice, technical support and lending a sympathetic ear, Jim Becker, Bill Chappell, Yongshik Lee and Tim Hancock. For comradeship, my office-mates Kavita Goverdhanam, Zhifang Li, Noel Baisa, Saqib Jalil and Todd Clancy. For empathy and like-mindedness on music, Mike Nuremberger. Mark Casciato and Leo DiDomenico for good talks and unique perspectives on the world. For lively conversation, unfailing willingness to help in the lab, and as patient sounding boards, Dimitri Peroulis, Alex Margomenos and Ron Reano. Brian and Jalene Hornbuckle, and Mike and Mindy Carr, for many wonderful dinners and Thanksgivings. For good conversation and trips to Washtenaw Dairy and Seva, Nigel and Katie Hinds, Jasmeet Judge and Jimmy Harnsberger, and Kathleen Bergen. Lars Andersen, for always telling it like it is. Ed Kim, for being an outstanding sailing partner and a patient teacher. Hua Xie, Charlie Brown, Wayne Walker and Leland Pierce, for chats on everything from Chinese cuisine to robots and buckeye trees. Helena Chan, for being the rebel who puts her money where her mouth is. Stéphane Legault, for being a kindred spirit and a good friend, long on class. Merci, cher ami.

I would also like to thank my friends and family, near and distant, who have kept me in their thoughts and prayers.

To my daughter, Victoria, I hope that I have been an inspiration. The world is waiting, my love. You need only open your heart and your mind, and reach for it.

For years of single-handedly managing life's day-to-day details with patience and charisma, I thank my husband and soul-mate Randy. For his undying support and love, I owe a debt that I can never repay.

If you come to a fork in the road, take it.

Yogi Bera

TABLE OF CONTENTS

LIST OF TABLES

LIST OF FIGURES

LIST OF APPENDICES

Appendix

CHAPTER 1

Introduction

Life need not be easy, provided only that it is not empty.

Lise Meitner

1.1 Motivation

RECENT advances in RF technology, dominated by defense, national security and scientific research systems such as radar, communications, electronic warfare and radiometry, have occurred in the 1-100 GHz frequency band. With the advent of affordable systems, improved performance with continued affordability is in demand. Reduced size and weight for mobile and airborne platforms, and reliability for long-term satellite platforms, require innovation in RF system architecture. Traditional waveguides and coaxial lines are large and difficult to integrate with monolithic integrated circuits (MIC) and passive devices. While MIC devices offer major reductions in volume and weight, they often are worse in terms of power handling capabilities and loss, compared to the traditional systems. Some of these issues must be taken as trade-offs, but other areas of MIC performance can be improved over traditional systems and current MIC status [2, 3].

The current satellite voice communication system channelized architecture can

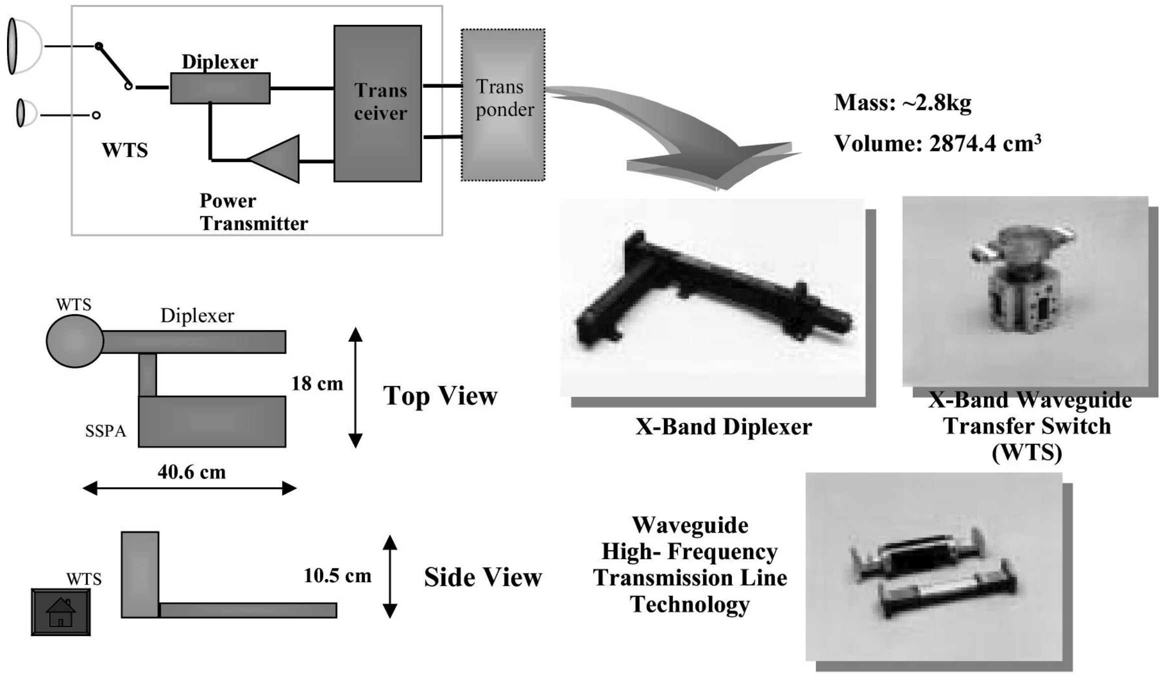

Figure 1.1: X-band waveguide based communication system.

trace its roots to the Intelsat IV series launched in 1971 [4]. Presently, in a typical millimeter-wave satellite communication system the received signal is directed from the antenna to a low-noise amplifier (LNA) via the diplexer, and the transmit signal is directed from a power amplifier via the diplexer to the antenna, see Fig. 1.1 [5]. Noise and power leakage between the two amplifiers can cause increased noise figure, intermodulation distortion and decrease in gain. High isolation and low insertion loss (IL) filters, which comprise the diplexer, mean power conservation on the transmit side and minimized noise figure for the receive side [6].

Typically, transfer switches and the diplexer components in the system are based on waveguides, and all the devices are connected by waveguide sections and packaged in a metal cavity. The communication subsystem can account for 15% or more of the total spacecraft dry mass. The overall dimensions of one such system are 18 cm x 40.6 cm x 10.5 cm, see Fig. 1.1. Metallic waveguide has a low-loss advantage, resulting in overall system loss of less than 2 dB. However, NASA is currently seeking to reduce spacecraft mass and volume so that smaller launch vehicles may be used, saving on mission costs and enabling an increase in launch frequency. This reduction will require high-density integrated sensors and systems, advanced packaging, and a move to higher frequencies, such as Ka band (25-40 GHz). Under support from the Jet Propulsion Laboratory, **this thesis addresses the issues related to the development of novel, three-dimensional micromachined cavity filters, specifically the reduction of weight and volume and how loss and quality factor Q are consequently affected**. This filter could then be implemented in a single monolithic satellite communication system. The feasibility of the complete system will be examined by JPL as the basis for the development of flight hardware to be used in future JPL missions [7].

A figure of merit for resonant circuits is the quality factor Q, which is defined as

$$Q = \omega \frac{\text{average energy stored}}{\text{energy loss/second}} \tag{1.1}$$

Hence, lower energy loss implies a higher Q. Three-pole Chebyshev filter models are used to demonstrate the decrease in insertion loss with increasing Q value in Fig. 1.2. To get a sense of exactly what this means in terms of power delivered to the load, consider that a Q of 500 that has 2 dB of insertion loss translates to 63% of the available power delivered to the load, and 37% dissipated by the filter. In contrast, a filter with a Q of 1000 and 1 dB of insertion loss translates to 79% power delivered to the load, and only 21% dissipated by the filter. The difference between 2 dB and 1 dB IL means a 25% increase in power delivered to the load by the filter. Microwave filters are traditionally made of metallic rectangular or cylindrical waveguides that yield a high quality factor Q and excellent performance. Micromachining techniques have been

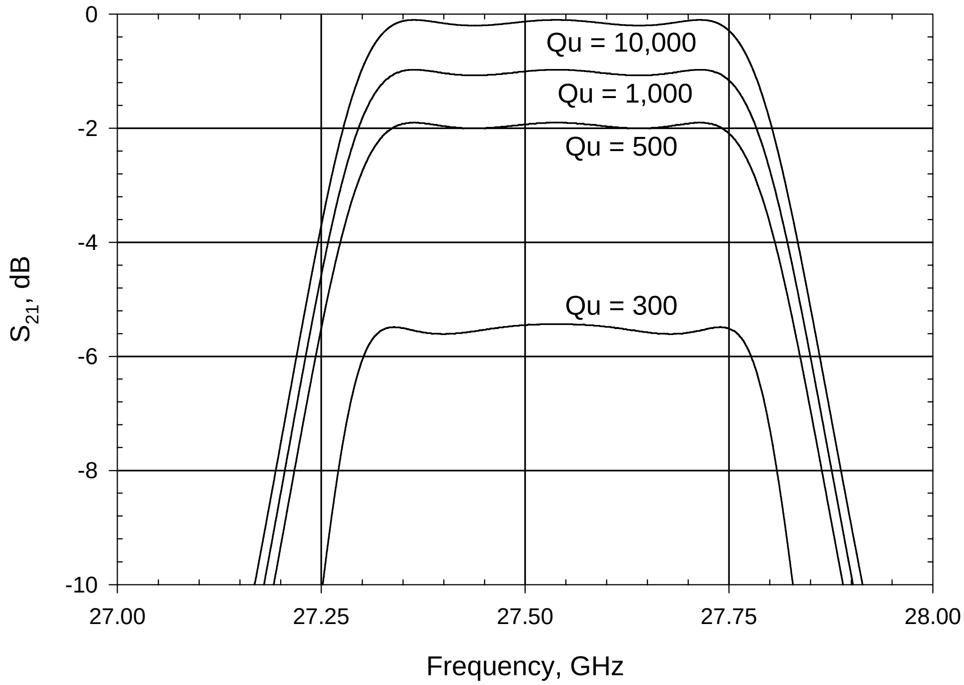

Figure 1.2: Comparison of varying Q_u values for 3-pole, 0.1 dB ripple, 2% bandwidth Chebyshev filters.

developed to reduce the size and weight of the traditional waveguide, as well as a variety of other devices. Micromachining of silicon makes it easy to create switches, phase shifters, directional couplers, membrane-supported microstrip, waveguide transformers, waveguide-to-planar circuit transitions, rectangular and conical feedhorns, and device packaging. Components can be built from these devices for ground-based and space-based radar, communications, and remote sensing applications. These components are monolithic, lightweight, compact and relatively inexpensive to produce [3, 6, 8, 9, 10, 11, 12, 13, 14].

1.2 Approach

The initial work done to reduce filter size and weight involved the use of lightweight materials such as graphite, dual-mode filtering, folded waveguide structures, and high-permittivity dielectric-loaded waveguides [4, 15, 16, 17]. For example, in [17] a dual-mode dielectric-loaded cavity was used to produce a temperature-stable filter with up to 80% weight reduction over previous techniques with comparable Q values.

Planar filter configurations have been investigated in the past few years and have been found to have a performance limited only by conductor losses of the resonator sections, but are limited to relatively wide bandwidth [7, 18, 19, 20, 21, 22]. For a generalized transmission line, the unloaded quality factor is given by

$$Q_u = \frac{\pi}{\lambda_g \alpha} \tag{1.2}$$

where λ_g is guide wavelength and α is total attenuation constant in Np/m. Transmission lines tend to be lossy in planar form and hence have a low Q_u [23]. For a high Q_u, small guide wavelength is needed, which requires higher dielectric constants. To avoid loss to substrate modes due to higher dielectric constants, thinner substrates and narrower transmission lines must be used. However, the narrower the transmission line, the higher the ohmic loss. Options include cavity-backed microstrip resonators and micromachined cavity resonators. Excellent work has been done in the area of micromachined planar filters, where the micromachining has been employed to produce membrane supported microstrip lines and micropackaging. These techniques yield reduced dielectric loss, reduced dispersion, reduced radiation loss and better isolation between circuits [21, 22, 24, 25, 26, 27]. In this work however, the micromachining technique is used to produce the 3-dimensional cavity, which is the resonant component of the filter, see Fig. 1.3.

The unloaded Q for an air-filled cavity resonator is given by the Q due to the lossy conducting walls,

$$Q_{cond} = \frac{(kad)^2 b\eta}{2\pi^2 R_s} \frac{1}{(2l^2a^3b + 2bd^3 + l^2a^3d + ad^3)} \tag{1.3}$$

where k is the wavenumber, η is the free-space impedance R_s is the surface resistivity

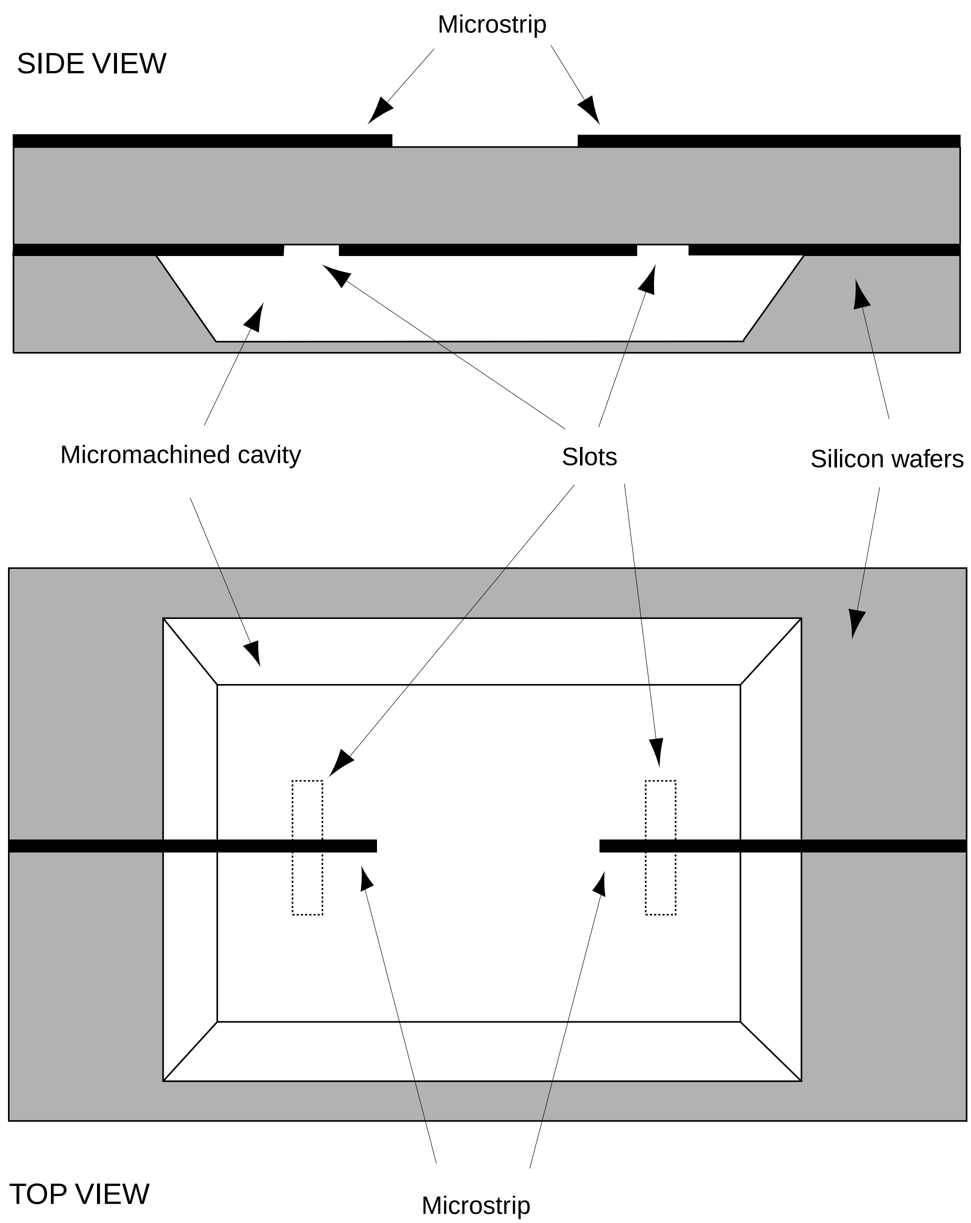

Figure 1.3: Microstrip-fed, slot-coupled, micromachined cavity.

of the metal cavity walls, the index $l = 1$ for the dominant mode (l being the index for the number of half-wavelengths in the z direction), a, b and d are the cavity width, height and length, respectively. Obviously, drastic reduction in volume will greatly reduce a resonator's Q_u. Full-size machined waveguide resonators have an unloaded $Q > 10,000$ in the microwave frequency range 1-100 GHz. Cavity resonators in silicon, for this same range, have unloaded $Q > 500$ [28]. This is a trade-off that cannot be avoided. For a filter made up of identical resonators, the filter Q can never be greater than that of a single one of those resonators.

In spite of this trade-off, micromachined resonators do show promise. A study at JPL has shown the ohmic loss of micromachined waveguides at 75-110 GHz to be 0.133 dB/cm, which is comparable to machined metallic waveguides [3]. Micromachined cavity resonators can be the building blocks for a filter design that is low loss, narrow bandwidth and small in size, and can be integrated into a monolithic diplexer design.

1.3 Dissertation Overview

This thesis presents novel micromachined cavity filters in the microwave frequency range. A number of unique contributions to the field have been made during the course of this work, including the following.

- A filter synthesis and design method for cavity resonators in silicon was established. Both vertical and horizontal integration designs will be demonstrated in this thesis. While the design of single cavity resonators is relatively simple, filter design using full-wave 3-dimensional modeling and analysis has proven to be quite difficult.
- The filter synthesis method was further improved with the addition of a time domain tuning technique.
- Fabrication technologies were applied in a novel way to create multiple, direct-

and cross-coupled, micromachined cavity filters in silicon that are unique in the microwave field, to the best of the author's knowledge.

The details supporting each of these contributions will be discussed in the subsequent chapters. In Chapter 2, an overview of the simulation, measurement and micromachining fabrication techniques employed in this work are presented. Also, transmission line transitions necessary to the measurements are discussed.

Chapter 3 presents the fundamental work upon which this thesis is built and gives a brief discussion of recent micromachined circuits. A study of the filter building block is included: a single micromachined cavity resonator slot-coupled to microstrip feeding lines. It is an extension of the work presented in [1], and shows how coupling to the fields in the cavity resonator, which changes with slot position, affects the bandwidth. By moving the slots closer together by half again the original distance from the cavity edge, the bandwidth is reduced by 58% and the loss is increased 0.74 dB, resulting in an unaffected unloaded Q. This is expected as the cavity size and not the slot positions determine the unloaded Q.

Chapter 4 presents an implementation of the micromachined cavity resonator in a vertically integrated 3-pole filter. Measured and HFSS simulated results are presented. The simulated and de-embedded measured results are 4% and 3.7% bandwidth and 0.855 dB and 1.97 dB insertion loss at 10 GHz, respectively. The overall circuit dimensions are 5 cm long $\times$ 3 cm wide $\times$ 2.6 mm high, a significant reduction in size compared to the traditional waveguide filter discussed above. Power handling capabilities are improved over the microstrip resonator as the surface currents are spread over a larger conductor surface area. However, this design format leads to several measurement and fabrication difficulties, including the use of fragile, 100 μm wafers, alignment and bonding problems, and the need for multiple feed line transitions for measurement purposes. These issues are not insurmountable, but some are the cause of losses that must be taken into account.

Chapter 5 presents an implementation of the micromachined cavity resonator in a horizontally integrated 2-pole filter. The investigation into a horizontally integrated design was undertaken to demonstrate the flexibility necessary for cross-coupled filters, including elliptic and linear phase models. Also, the 100 μm wafers were eliminated and the measurement method was simplified. As the cavities are horizontally integrated, the wafer stack thickness is reduced over the vertically integrated model. Two wafers are used to produce the cavities, doubling the cavity resonator volume and increasing the Q_u. The overall circuit dimensions were 18 mm long $\times$ 6.629 mm wide $\times$ 1.6 mm high. The filter was designed for a 2.3% bandwidth at 31.74 GHz with 1.2 dB insertion loss. The measured filter yielded a 2.2% bandwidth at 31.75 GHz and exhibited 1.6 dB insertion loss. A very good Q_u of 1422 was measured at 31.7635 GHz, compared to a calculated theoretical value of 1670 at this frequency and a modeled theoretical value of 1659 at 31.68 GHz.

Chapter 6 presents an implementation of the micromachined cavity resonator in a cross-coupled, horizontally integrated 4-pole linear phase filter. This filter demonstrates the linear phase characteristic achieved by cross-coupling nonadjacent resonators. A new design technique employing lumped element models and time-domain analysis using inverse FFT was developed. The overall circuit dimensions were 19.5 mm long $\times$ 15.4 mm wide $\times$ 1.9 mm high. The filter was designed for a 2.2% bandwidth at 27.48 GHz with 1.4 dB of insertion loss. The measured filter exhibited a 1.9% bandwidth at 27.604 GHz with 1.6 dB of de-embedded insertion loss. An excellent Q_u of 1465 at 27.8838 GHz was measured, compared to a calculated theoretical value of 1614 at this same frequency.

Chapter 7 summarizes the work presented in this thesis, suggests improvements on the current methods and discusses future work that might be explored with the micromachined cavities.

CHAPTER 2

Experimental Techniques

You cannot hope to build a better world without improving the individual.

Marie Sklodowska Curie

2.1 Simulation Techniques

A NUMBER of circuit and electromagnetic simulation packages were used in the course of this work to model lumped element, planar, and three-dimensional electromagnetic circuits. The workhorse of the group is Ansoft's High Frequency Structure Simulator (HFSS) [29]. This software package was used to model all of the cavity resonator circuits. HFSS uses the Finite Element Method to model electromagnetic fields of three dimensional structures. A geometric model can be constructed of a variety of materials, and can be excited by a well-defined electromagnetic source. A tetrahedra mesh of the geometric model of the structure is generated and a local function represents the field in each tetrahedra element. Maxwell's equations are then transformed into matrix equations for each element and are solved by traditional numerical methods. The solved S-parameters, the fields and the currents can be displayed.

The other simulation tools that were used are Agilent's Advanced Design System

(ADS) for lumped element circuit design and Zeland's IE3D for planar transmission line design [30, 31]. ADS was used to design equivalent lumped element filter circuits, and IE3D was used to model various coplanar waveguide (CPW) to microstrip transitions.

2.2 Measurement Techniques

The circuits presented in this work were measured using an HP8510 Vector Network Analyzer (VNA) test setup, see Fig 2.1. The system is comprised of an HP8350B sweep oscillator, HP8516A or Agilent 8517B S-Parameter test set (45 MHz to 40 or 50 GHz), HP85105A millimeter-wave controller, HP83640L swept CW generator (10 MHz to 40 GHz) and an Alessi probe station. For on-wafer probing, GGB Industries Picoprobes model 40A with 150 μm pitch designed for up to 40 GHz were used [32]. Coaxial cables with K-connectors attach the probes to the 8516A/17B test set. The probes have three probe tips, a center signal tip and two outer ground tips for probing CPW lines. The probe pitch refers to the distance between the inner and outer tips, and governs the design of the CPW probe area on the circuit.

In order to accurately predict how an individual device will perform in its intended system environment, it is necessary to remove the effects of measuring the device, i.e., calibrate out the errors and impedance discontinuities introduced by the probes, the cables, the adaptors and the test setup, and the connections between each. For monolithic circuits this is typically done using the Thru-Reflect-Line (TRL) calibration technique, which is accomplished by measuring a non-zero length through line, a reflect line, and at least one delay line of known length not equal to the through length. The reflect line is either an open or a short, and is one half the length of the through line. The measurement reference plane is moved past the probe tips to a point equal to half the length of the through line. By comparing the known to

Figure 2.1: Microwave measurement setup.

the measured responses of the standards, the full 12-term error signal flow model is developed and used to mathematically remove the repeatable systematic effects of leakage, port mismatch and frequency response [33].

The TRL calibration is accomplished with the aid of the software program MultiCal developed at the National Institute of Standards and Technology (NIST) [34]. This program uses the de-embedding algorithms developed by Marks [35] based on multiline Thru-Reflect-Line measurements. Physical lengths of all of the lines and estimated effective dielectric constant are provided to the program. MultiCal calculates the error coefficients and loads them directly into the VNA. Characteristic impedance, dielectric, propagation and attenuation characteristics of the calibration lines are also calculated. One thru/line pair covers an 8:1 bandwidth, where bandwidth is defined as the frequency span/start frequency. The optimal line length is $\lambda_g/4$ at the span center frequency, and multiple lines can be used to cover greater bandwidths. MultiCal optimally weights the solution if multiple delay lines are used [33].

2.3 Silicon Micromachining

Silicon is the mechanical substrate of choice for the work presented here. It is strong yet slightly flexible, has a high-quality, thermally stable native oxide, has crystal plane topography that is well suited to micromachining, has desirable electrical properties, and the processing technology is well-established. Micromachining of silicon is the process of forming three-dimensional structures in and out of the silicon. The techniques used in this thesis are bulk wet and dry anisotropic etching. Bulk refers to the removal of the silicon, i.e., the creation of holes in the substrate. Several processing techniques are discussed here; more detailed processing steps may be found in the Appendices.

2.3.1 Wet Etching

Silicon etching is, generally speaking, either isotropic or anisotropic, which refers to the degree and nature of undercut from the perpendicular to the substrate surface. Wet isotropic etching tends to progress equally in all directions if the solution is agitated. Anisotropic etching is more directional, producing more vertical sidewalls, with selectivities to particular crystal planes of the substrate or some other limiting factor depending on the mechanism of the etch. As may be inferred, the orientation of the mask pattern also influences the pattern etched. To produce an etched rectangle for example, it is desirable to align the edges of the mask rectangle pattern parallel to the crystal planes. If the pattern is not parallel, the etch will proceed to remove material up to the crystal planes defined by the outermost points of the mask pattern as shown in Fig. 2.2. Four inch diameter silicon wafers were used in this work, scribed into quarters by hand. The wafer is cleaved along the (110) family of crystal planes, providing a straight edge for which to align mask patterns to the crystal orientation.

The silicon wafers used here have a (100) crystal plane surface orientation. Wet

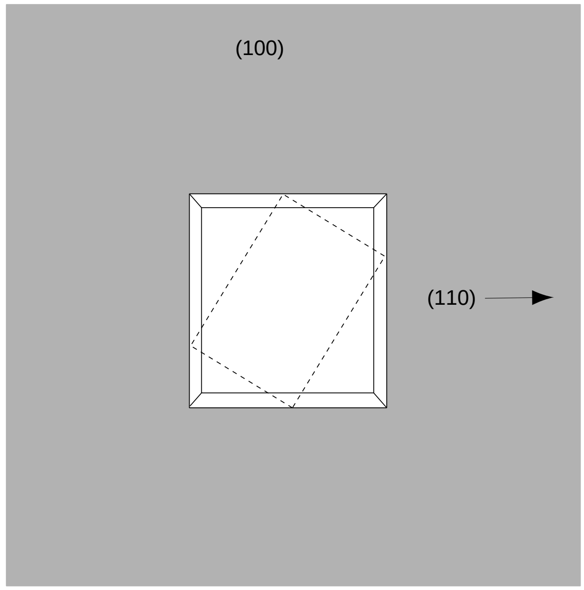

Figure 2.2: Sketch of anisotropic etch with crystal plane orientation selectivity. Original mask pattern is shown by the dashed line.

chemical solutions used to etch this orientation will have certain selectivities to the other crystal planes; a 1/10 ratio for (111)/(100) for example would yield an undercut of the etch mask of 1 μm for every 10 μm of vertical etch, exposing the slower etching (111) plane on the sidewalls as the etch progresses as sketched in Fig. 2.3. The 54.7° orientation of the sidewall to the horizontal is dictated by the orientation of the crystal planes.

The wet anisotropic etchants used in this work are tetramethyl ammonium hy-

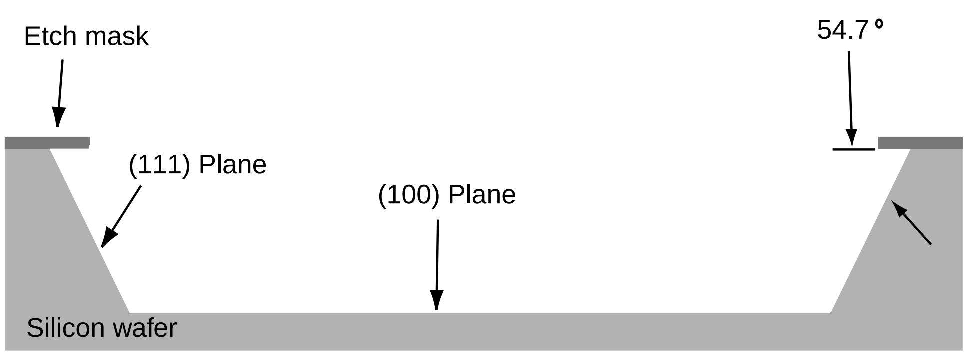

Figure 2.3: Cross sectional view of anisotropic etching of (100) silicon.

droxide (TMAH) in water, and potassium hydroxide (KOH) in water. The crystal plane selectivity is decided in part by concentration and temperature of the solution being used. The etching action for hydroxides of alkali metals, of which KOH is one, can be stated as the chemical reaction created as the surface silicon atoms react with the hydroxyl ions, eventually forming silicate etch products and hydrogen.

KOH has the highest (111)/(100) selectivity ratio, typically around 400:1. When a solution of 300 g of KOH dissolved in 60 mL of water is agitated and maintained at 65° C, the solution yields about 30 μm etch per hour. TMAH selectivity ranges from 10:1 to 35:1, yielding a larger undercut of the etch mask. When 1 L of 25 wt% TMAH is maintained at 85° C, the solution yields 27-33μm etch per hour.

The author found that KOH was best at etching fine features. Silicon dioxide (SiO_2) was often used as an etch mask for both KOH and TMAH, which have certain selectivities to dielectric thin films. As KOH etches the SiO_2 faster than does TMAH, KOH was reserved for the etching of particularly small features such as vias, and also wafers of sufficient thinness that the wafer etch completed before the SiO_2 was depleted.

The etch rate of thermal SiO_2 is 0.05 to 0.25 nm/min, so that several thousand angstroms of SiO_2 may be used as a sufficient etch mask for hours-long TMAH etches [36]. Previous work has shown that surface roughness of the etched surfaces decreases with increasing TMAH concentration, and that 25 wt% yielded the smoothest sidewalls [37]. Both 12 wt% and 25 wt% concentrations were used in this work.

2.3.2 Deep Reactive Ion Etching

The fabrication of sensors and MEMS (micro-electro-mechanical systems) typically requires a more precisely controlled etched profile than can be achieved through wet chemical etching. The need for high aspect ratio etching and critical dimension control has in large part been met by the recent advances in deep reactive ion etching plasma technology. The dry anisotropic etching performed in this work was accomplished with the use of a Surface Technology Systems (STS) Reactive Ion Etcher System (RIE), which provides a nearly vertical sidewall etch [38]. A schematic of the system is presented in Fig. 2.4. The wafer is loaded onto a movable stage in the load/lock chamber, which is then pumped down. After pumping is complete, the stage moves the wafer into the process chamber and places it onto the wafer platen chuck. The wafer is clamped, atmospheric pressure is applied and helium gas is flowed to check for leaks around the wafer and the wafer chuck. Once this step has completed successfully, the etching process can begin.

An RF-induced, inductively coupled, high density, low pressure plasma accelerates electrons to energy levels capable of breaking chemical bonds in the plasma gases, yielding ions and additional electrons. DC bias across the sheath, which is the dark region between the plasma glow and the electrodes, accelerates the ions to bombard the target wafer positioned on the platen electrode. The high density, low pressure plasma increases ion directionality, which improves profile controllability.

With a fluorinated chemistry, the etch mechanism is a combination of ion bombardment, thermal reaction between the fluorine gas used, and physical sputtering of the substrate. The etch rate, uniformity, anisotropy (profile) and etch mask selectivity are controlled by the process parameters chosen for the etch. Platen power and temperature (and hence wafer temperature), coil power, pressure, gas flow, etch time, wafer size, and exposed etch area all affect the parameters. The process used here is a time-multiplexed gas flow approach, whereby etching and passivating gas flows are alternated. The first step is the etch step, which forms a shallow etch in the silicon. The second step is the passivation step where a fluorocarbon film is deposited on the sidewalls and base of the etched feature, protecting it from further etch. Then another etch step occurs, where increased ion energy in the vertical direction removes the protective film from the horizontal surfaces only and further etches the feature. In this

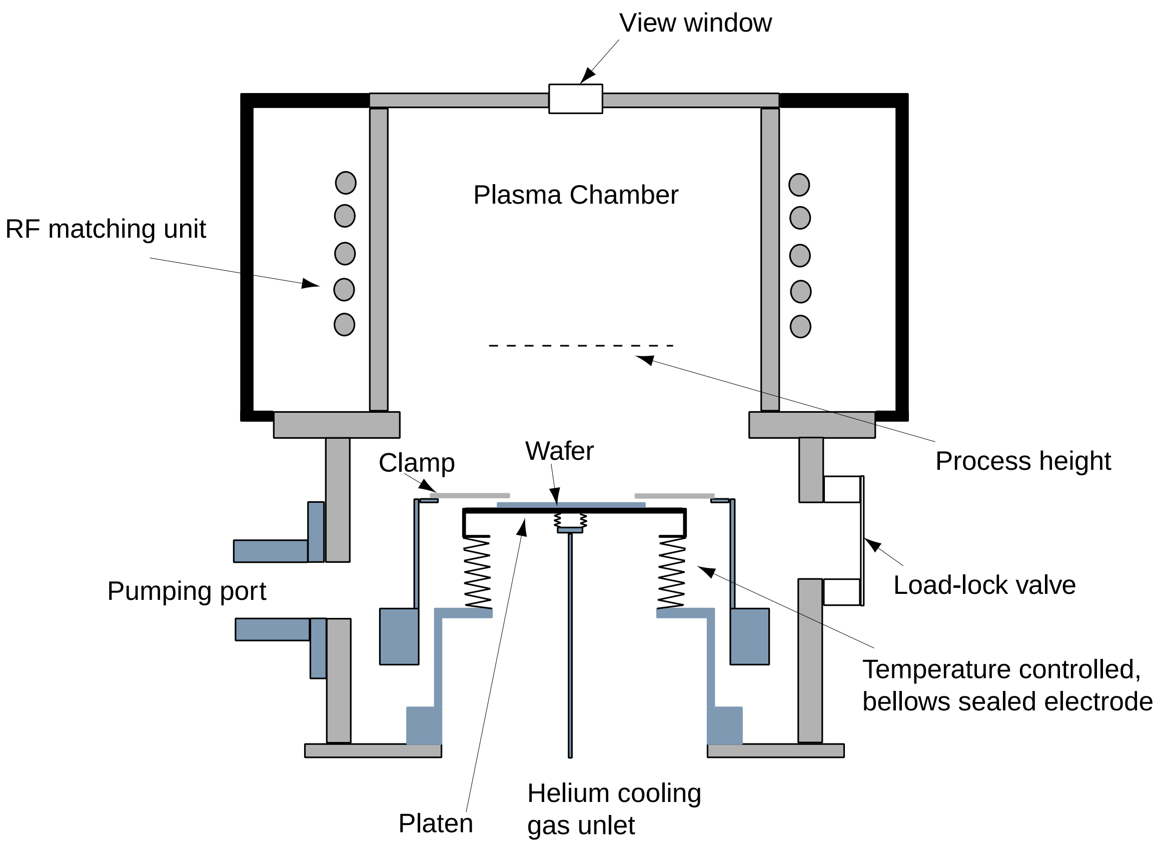

Figure 2.4: Schematic of STS Deep Reactive Ion Etch system.

manner an anisotropic etch is performed, yielding vertical sidewalls. For this work, a 12 or 13 second SF_6 flow provides the etching action and a 7 or 8 second C_4F_8 flow provides the passivation action. The steps are alternated repeatedly until the feature is completely etched. A detailed description of the process parameters can be found in Appendix A. A thick photoresist etch mask was used in all cases [39, 40, 41, 42]. An SEM (scanning electron microscope) micrograph of both a TMAH etched pyramidal pit and RIE etched cavities is shown in Fig. 2.5.

Surface roughness is one issue that must be considered when using RIE etching techniques. Because the passivating and etching steps are alternated in the time-multiplexed system, a horizontal scalloping of the sidewall can occur. Scalloping depths of 50 to 300 nm may be seen. Additionally, soft etch masks such as photoresist can be attacked and thinned at the defined feature edges. The rate at which the photoresist is worn away is not perfectly consistent across the feature, and vertical striations, also known as “roughening bands”, can be transferred to the etched sidewalls as a consequence [40]. An example of these vertical striations can be seen in Fig. 2.6, which shows an etched cavity sidewall. Etching has been done from both the top and bottom of the wafer shown in the figure, and “roughening bands” can be seen at both the top and bottom surfaces.

2.4 Thermocompression Gold-to-Gold Bonding

The quality of the bond between the wafers is largely responsible for the performance of the filters presented in this work. The resonant cavities consist of multiple wafers that must be aligned and bonded. The breaks between each wafer are perpendicular to the surface currents in the cavity, and therefore even a small gap between the wafers will result in a degradation in the filter performance and Q_u. Earlier work has been done investigating the efficacy of gold-to-gold wafer bonds produced by ther-

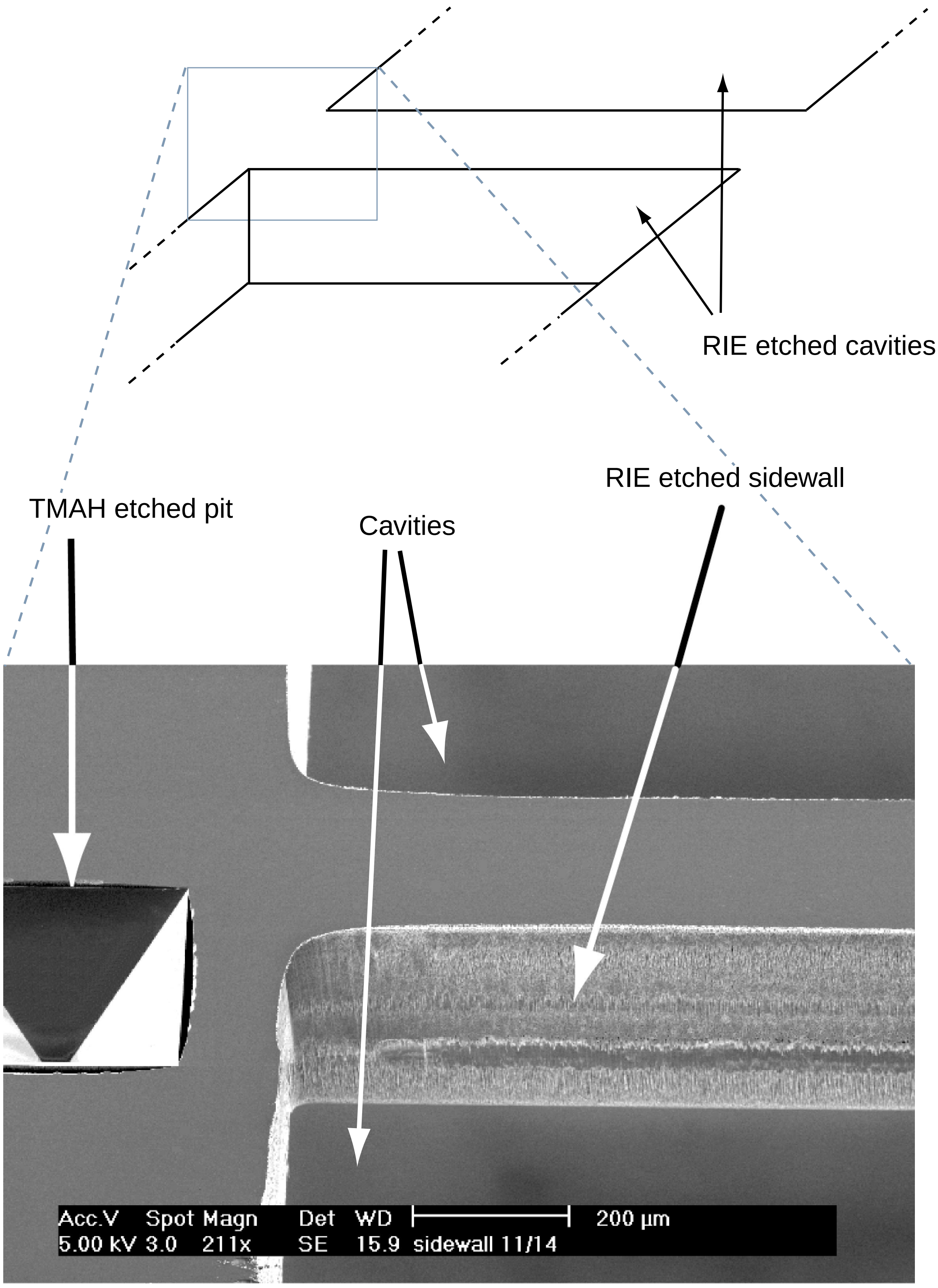

Figure 2.5: SEM micrograph illustrating anisotropic wet TMAH and dry RIE etched features.

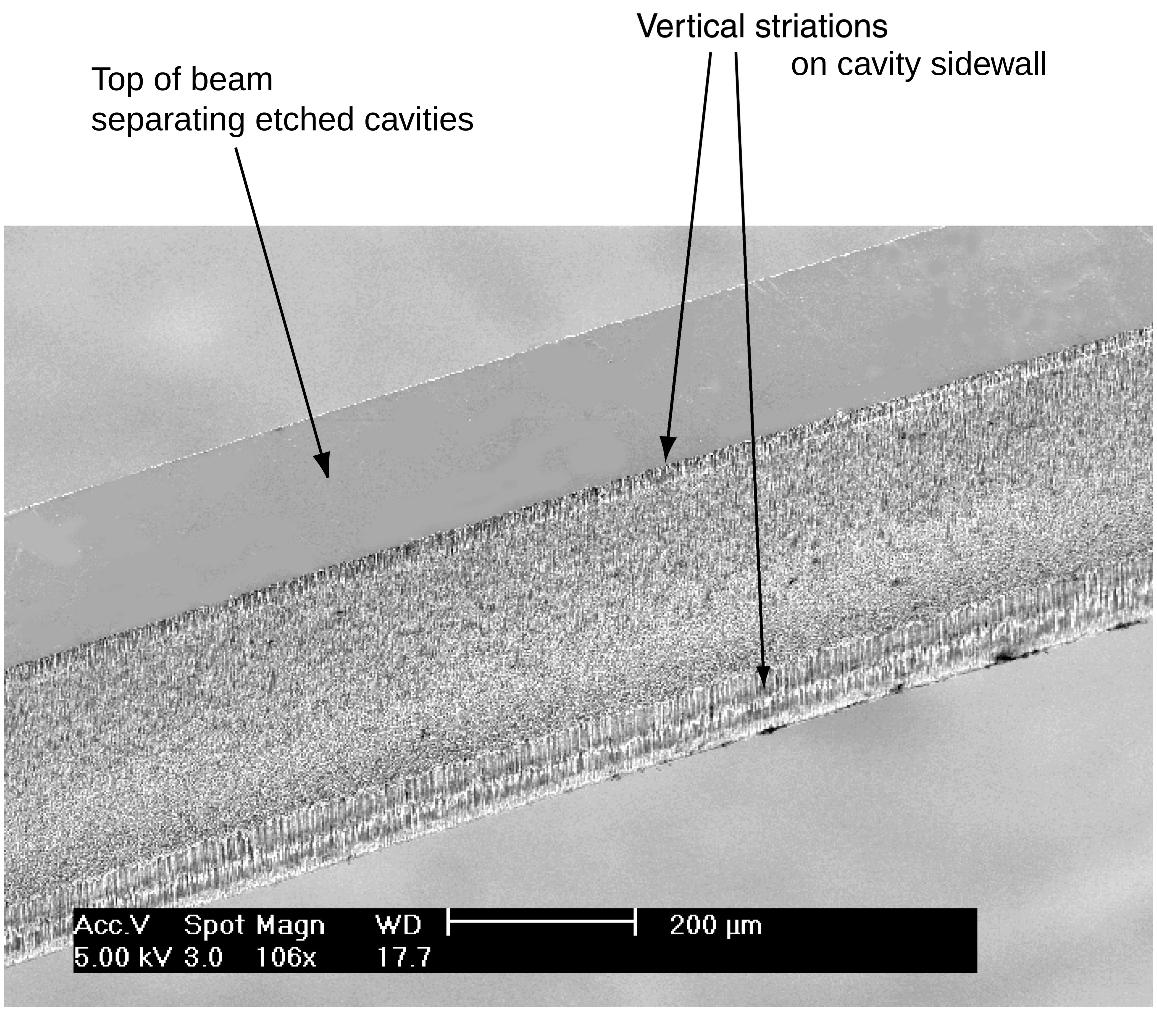

Figure 2.6: SEM micrograph illustrating the vertical striations that occur with soft etch masks.

mocompression bonders, a summary of which appears in [10]. Prolonged exposure to applied pressure and increased temperature are the parameters used to produce gold-to-gold bonds between wafers. The short range attractive force between the positive ions and the free electrons in the conductive gold lattice provides the bonding. Pressure brings the gold atoms into intimate contact, increased temperature excites the atoms and diffuses them, and prolonged subjection to pressure and temperature ensures the quality of the bond. The quality of the metal surface affects the bond as well. Removal of contaminant particles and films is accomplished through solvent cleaning, dehydrate baking, and UV exposure to remove adsorbed organics such as nitrogen and carbon. For part of this work, solvent cleaning and dehydration was followed by UV exposure of 15-30 minutes per bonding surface to improve the quality of the gold-to-gold bonds.

2.5 CPW to Microstrip transitions

As stated earlier, the test setup incorporates three point CPW probes for microwave measurements. Hence, all circuit feed lines must begin with CPW probe areas. The resonant cavities are designed to be fed by 50 Ω microstrip lines on varying substrate thicknesses, so a variety of CPW-to-microstrip transitions were designed.

2.5.1 Front-to-Back Wafer Transition

In one particular filter design, the output microstrip was printed on the backside of the wafer. The CPW probes cannot probe the underside of a wafer, so it was necessary to design a front-to-back wafer transition, with the CPW probe area on the front or topside of the wafer transitioning to a microstrip line on the back of the wafer after the fashion of [43] and as shown in Fig. 2.7. The CPW probe area is tapered into a slotline, and the slotline is then electromagnetically coupled into the microstrip

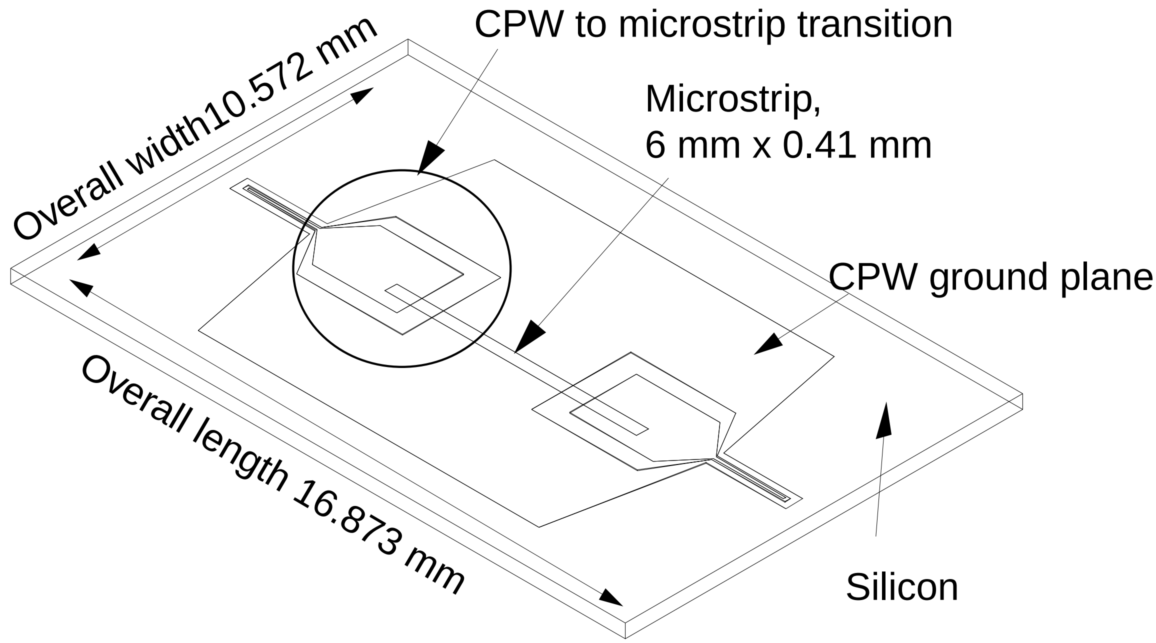

Figure 2.7: CPW to microstrip transition in a back-to-back, through-line configuration. The CPW is on the top of the wafer, the microstrip is on the bottom of the wafer.

on the backside of the wafer. The major electric field component in both the CPW mode and the slotline mode is transverse across the gap, so the transition from one mode to the other is fairly seamless. Because it is a two-conductor transmission line, the slotline has a zero cut-off frequency.

The microstrip stub length, from the slotline center to the open end of the microstrip, was designed to be approximately $\lambda_g/4$ at 10 GHz, the resonant frequency of the filter. It is reasonable to expect that an open end of a quarter wavelength microstrip stub extension would present a short (current maxima) to the slot center, allowing for strong magnetic coupling to the slot. However, fringing fields of the microstrip open end effect mediates this to a length slightly less than $\lambda_g/4$.

To the microstrip, the slotline appears to be two transmission lines in parallel. Therefore, a matched 50 Ω impedance is achieved by designing the slotline to have a 100 Ω impedance. Closed-form expressions for slotline impedance given in [44] are obtained by curve fitting results based on analysis by Cohn in [45], with a 2% accuracy. For $0.2 \leq W/h \leq 1.0$, where W is the slot width and h is the substrate thickness, the expressions are

$$\begin{aligned}
\lambda_s/\lambda_o &= 0.987 - 0.483\log\epsilon_r + W/h(0.111 - 0.0022\epsilon_r) \\
&\quad - (0.121 + 0.094W/h - 0.0032\epsilon_r)\log(h/\lambda_o) \times 10^2 \\
Z_{0s} &= 113.19 - 53.55\log\epsilon_r + 1.25W/h(114.59 - 51.88\log\epsilon_r) \\
&\quad + 20(W/h - 0.2)(1 - W/h) \\
&\quad - [0.15 + 0.23\log\epsilon_r + W/h(-0.79 + 2.07\log\epsilon_r)] \\
&\quad \cdot [10.25 - 5\log\epsilon_r + W/h(2.1 - 1.42\log\epsilon_r) \\
&\quad - h/\lambda_o \times 10^2]^2
\end{aligned} \tag{2.1}$$

Using these expressions, a slotline width for 100 Ω was determined.

Starting with 50 Ω CPW and microstrip lines, a $\lambda_g/4$ microstrip open end stub length and a 100 Ω slotline width, the design was constructed in IE3D. After fine-tuning these parameters, as well as the slotline length and the taper length, it was found that a $\lambda_g/6$ microstrip stub length of 1800 μm and a 112 Ω slotline width of 777 μm provide a relatively good match on a 400 μm silicon substrate.

Several back-to-back through-line transitions (CPW to microstrip to CPW) were fabricated on high-resistivity 400 μm silicon wafers in order to determine the loss per transition. The simulated and measured results for the filter frequency range of interest are shown in Fig. 2.8. The loss per transition was found to be 1.2 dB at 10 GHz.

The difference between measured and simulated results for the back-to-back through-line is partially explained by the way in which IE3D models ohmic loss. To confirm this theory, a 50 Ω through-line was modeled in IE3D and found to have a predicted loss of 0.16 dB/cm at 90 GHz. However, the same through-line was fabricated,

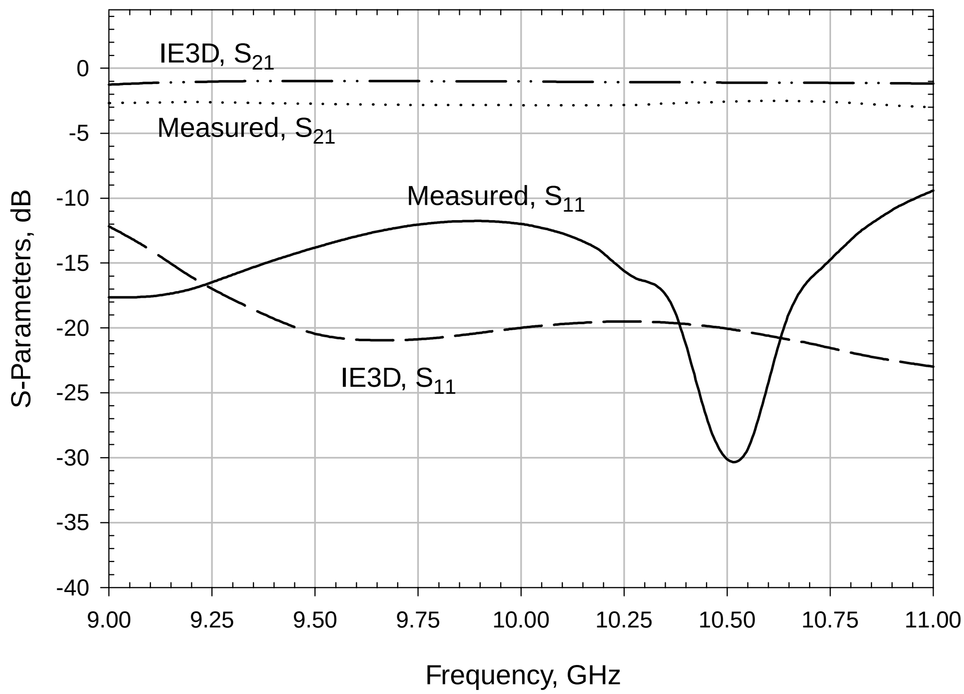

Figure 2.8: Comparison of modeled and measured results for CPW to slotline to microstrip transition in a back-to-back, through-line configuration.

measured and found to have 0.28 dB/cm loss at 90 GHz [10]. Although a finite conductivity of 4.1×10^7 S/m is used in the model presented here, the program models the conductors by using the surface impedance of an infinite conductor and approximations to account for skin depth, and does not attempt to compute the fields inside the conductors [10, 46]. In addition, 4.1×10^7 S/m is the theoretical maximum value for the conductivity of gold. Any surface roughness or imperfection will degrade this value. Indeed, the processes used in this work to produce metallized surfaces all produce some degree of surface roughness. Therefore, although this value was used as a reference point for modeling the circuits presented here, it is known to be an optimistic assessment of the fabricated gold conductivity [47, 48].

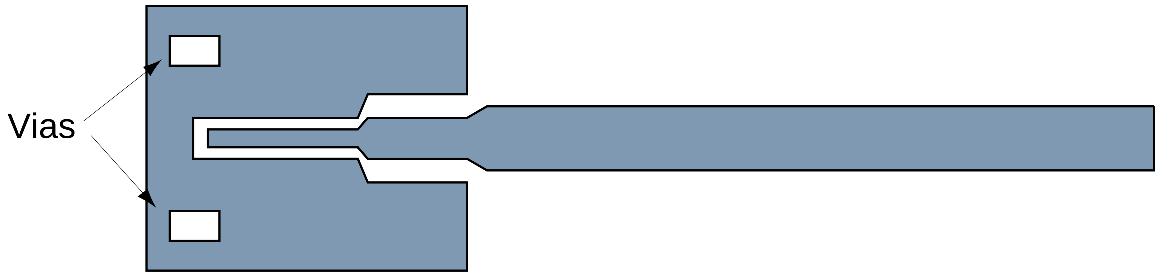

Figure 2.9: CPW to microstrip taper transition using potential equalizing vias. The microstrip ground plane is everywhere, including under the CPW lines.

2.5.2 Via-less Transition

A very simple CPW to microstrip transition involves vertical through-wafer metallized vias that connect the CPW ground planes to the microstrip ground plane on the backside of the wafer as illustrated in Fig. 2.9. This design was used initially in the work presented in [49] and for the input feed line in the 10 GHz filter model discussed above [50]. For ease of fabrication it was desired to eliminate the via and rely on electromagnetic coupling, where the mode transitions smoothly from CPW to microstrip propagation. Wideband W-band transitions were demonstrated in [51], where the implementation followed the design procedure of [52], which considers the transition as a six-port network of three coupled microstrip lines operating in the even and odd CPW modes and the microstrip mode. The design involves determining the 2-D quasi-static mode capacitances as in [53], from capacitances the mode impedances and the effective dielectric constants are found, from the mode impedances the geometries of the lines are calculated, and the guide wavelength is found from the effective dielectric constant of the three coupled lines.

A variation of the radial stub transition is developed for the filters presented here. The transition length should be $\lambda_g/4$ at the frequency of interest. With the CPW ground plane open radial stub at this length, a short to the microstrip ground plane is presented at the start of the transition, providing a means to shift the propagating

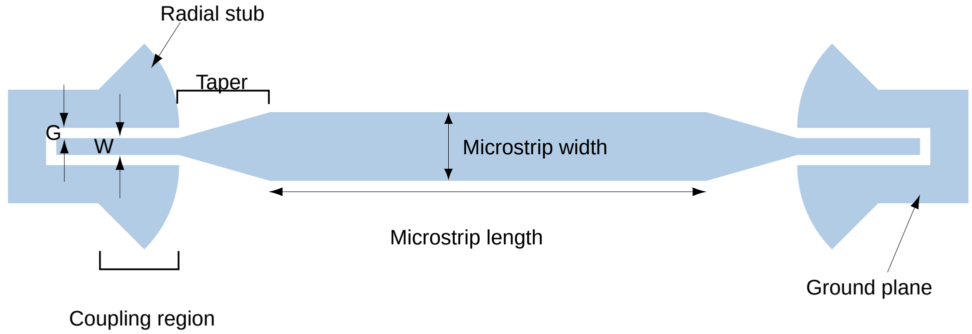

Figure 2.10: CPW to microstrip radial stub transition. The microstrip ground plane is everywhere, including under the CPW lines.

mode. A simple implementation is to model the transition as a CPW $\lambda_g/4$ and fine-tune it in IE3D. This was done on both 200 μm and 400 μm silicon substrates.

The model on 200 μm substrate has a 50 Ω CPW pitch of 70-90-70 μm (G-W-G), a 45° radial stub (coupling region) length of 420 μm, a taper length of 250 μm and a 50 Ω microstrip width of 164.76 μm as shown in Fig. 2.10. The response for this model with a 3 mm long microstrip exhibits a usable bandwidth of approximately 15 to 45 GHz (2:1), shown in Fig. 2.11. A comparison of measured and simulated results for a back-to-back model with 926 μm long microstrip is shown in Fig. 2.12. The loss per transition is 0.2 dB, and the microstrip loss is 1.0 dB/cm at 32 GHz.

The model on 400 μm substrate has a 50 Ω CPW pitch of 58.56-90-58.56 μm, a 45° radial stub length of 443 μm, a taper length of 500 μm and a 50 Ω microstrip width of 374 μm. The response for this model with a 2.4 mm long microstrip exhibits a usable bandwidth of approximately 15 to 35 GHz (1.3:1), as shown in Fig. 2.13. A comparison of the measured and simulated results for a back-to-back model with 500 μm long microstrip is shown in Fig. 2.14. The loss per transition is 1.2 dB, and the microstrip loss is 0.7 dB/cm at 27.6 GHz.

The difference in the performances of the 2 models is partially explained by dielectric loss. The effective dielectric constant of a given 50 Ω microstrip line will increase

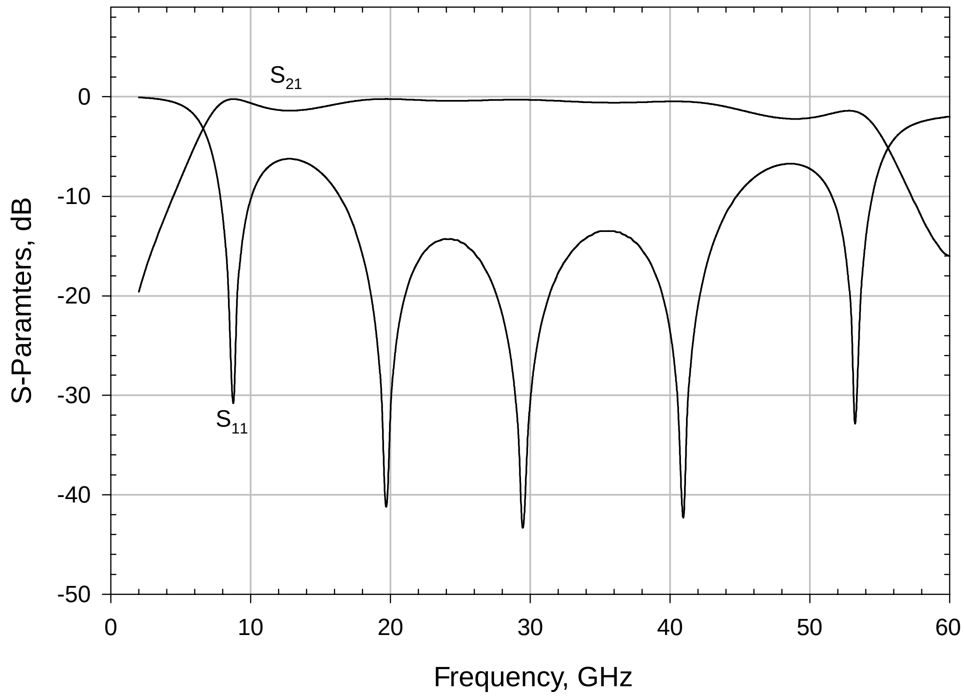

Figure 2.11: Modeled response of the CPW to microstrip radial stub transition in back-to-back formation on 200 μm silicon.

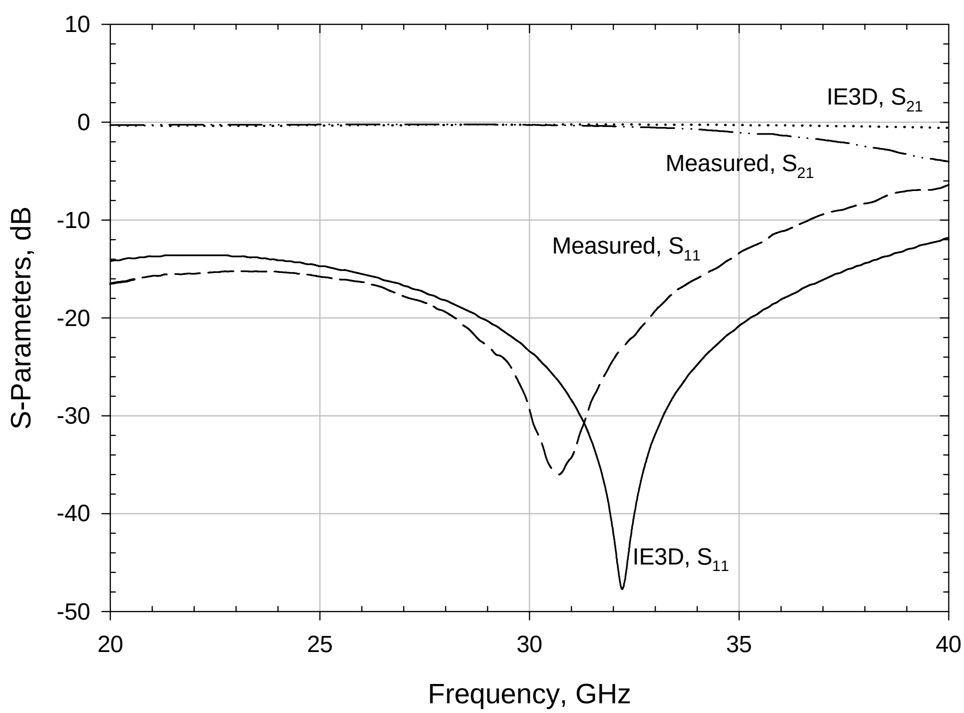

Figure 2.12: Comparison of modeled and measured CPW to microstrip radial stub transition in back-to-back formation on 200 μm silicon.

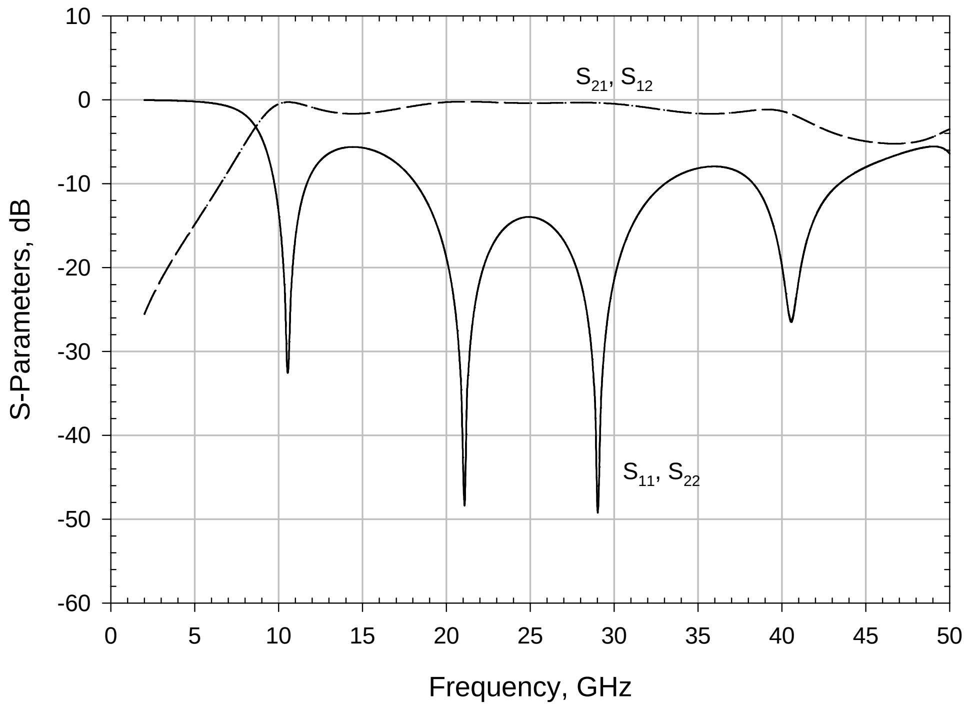

Figure 2.13: Modeled response of the CPW to microstrip radial stub transition in back-to-back formation on 400 μm silicon.

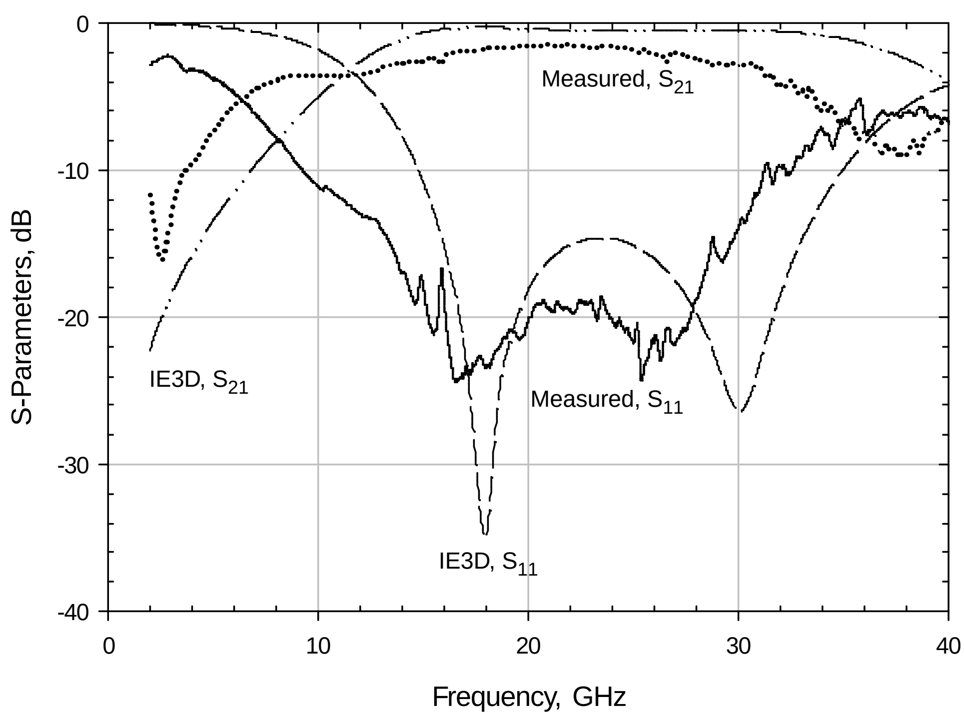

Figure 2.14: Comparison of modeled and measured CPW to microstrip radial stub transition in back-to-back formation on 400 μm silicon.

with increasing substrate thickness and is given approximately by [23]

$$\epsilon_{re} = \frac{\epsilon_r + 1}{2} + \frac{\epsilon_r - 1}{2} \frac{1}{\sqrt{1 + 12d/W}} \tag{2.2}$$

where ϵ_r is the dielectric constant, d is the thickness of the substrate and W is the width of the microstrip line. Dielectric loss for microstrip on silicon is significant, and is given by [44]

$$\alpha_d = 4.34 \frac{1}{\sqrt{\epsilon_{re}}} \frac{\epsilon_{re} - 1}{\epsilon_r - 1} \sqrt{\frac{\mu_o}{\epsilon_o}} \sigma \tag{2.3}$$

in dB/unit length, where σ is the conductivity of the dielectric. An increase in substrate thickness therefore increases dielectric loss. The expression for dielectric loss in CPW is the same as that given for microstrip.

To minimize dielectric losses, it is necessary to keep the substrate electrically thin. A substrate thickness d less than $\lambda_g/10$ at the frequency of interest is a good rule of thumb. For the model on 400 μm silicon discussed above, the substrate thickness is $\lambda_g/9.6$ at 28 GHz, which is at the limit of electrical thinness.

Radiation loss in CPW lines is attributed to parasitic modes, among them the odd mode (where slot voltages are opposite in phase), which can be excited at discontinuities and which can be circumvented by providing air bridges to equalize the ground planes, or by bridging the ground planes on the surface of the substrate behind the center conductor and using a relatively short length of CPW line as was done in the models presented here. Grounded CPW can also exhibit a parasitic parallel-plate mode. As the ground plane in this work extends everywhere under the circuit and the measured circuits are rather large, parallel-plate modes may contribute to the losses seen in the measurements [44].

2.6 Summary

This chapter presented some of the tools and techniques used to design and model, fabricate and measure the transitions and filters presented in this thesis. The transitions necessary for measuring the filters were presented, and the contributing losses summarized. Chapter 3 continues with a discussion on work by previous authors upon which this research based, recent micromachining research, and the preliminary studies conducted by this author.

CHAPTER 3

Previous Work

For a successful technology, reality must take precedence over public relations, for Nature cannot be fooled.

Richard Feynman

3.1 Background

LIKE all research, the development of a micromachined cavity filter has its basis in the work of others. Norm VandenBerg developed a very wide band vertical transition between two microstrips via a slot aperture in their common ground plane, see Fig. 3.1 [54]. The transition had just 1 dB of insertion loss from 6.5 to 18 GHz. This transition has been used to couple feeding microstrip lines to a single, micromachined resonant cavity, see Fig. 3.2 [1]. The circuit consists of input and output microstrip lines printed on top of a silicon wafer, coupling energy into a micromachined cavity formed on a second wafer via slots. The theoretical modeling of the fields inside the cavity was performed using a hybrid FEM-MoM technique that compared favorably to FDTD results [55]. The fabricated, measured cavity resonated at 10.3 GHz with 0.4 dB of insertion loss. It was proposed that the cavity resonator be used as a building element for the design and fabrication of narrow-band, low-loss filters and multiplexers with multiple cavities of the same or different size coupling

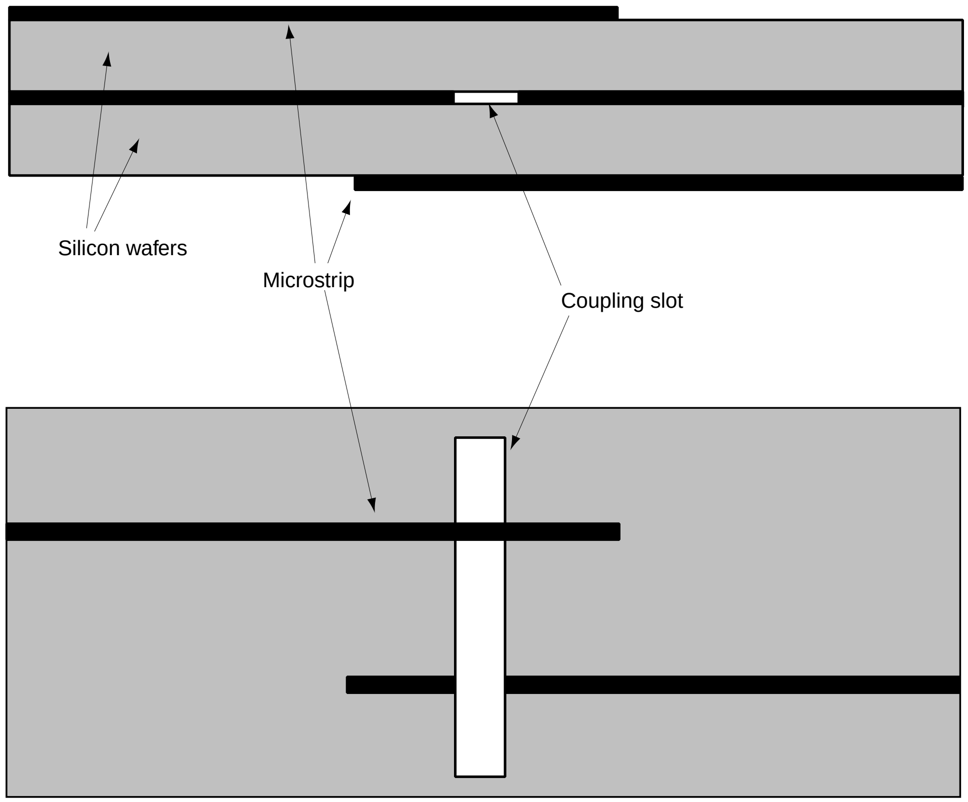

Figure 3.1: Microstrip-to-microstrip transition via a slot in their common ground plane.

energy to each other via slots of different shapes and positions.

It is instructive to give a brief summary of the nature of the microstrip-slot aperture coupling and the field theory behind the waveguide eigenmodes. Illustrated in Fig. 3.3 is the microstrip mode, with electric and magnetic field lines in the substrate between the microstrip and an infinitely thin ground plane. If a slot aperture is opened in the ground plane, the field lines will fringe through the slot as shown. Now consider a closed ground plane and first, an infinitesimal electric polarization current, perpendicular, on either side of the ground plane, and second a similar but parallel magnetic polarization current. Now consider the similarities between the fields generated by the polarization currents above and below the ground plane, and the fields due to the microstrip mode fringing through and around a slot opened in the ground plane. Hence, the slot can be replaced by polarization currents $\bar{P}_E$ and $\bar{P}_M$ that are

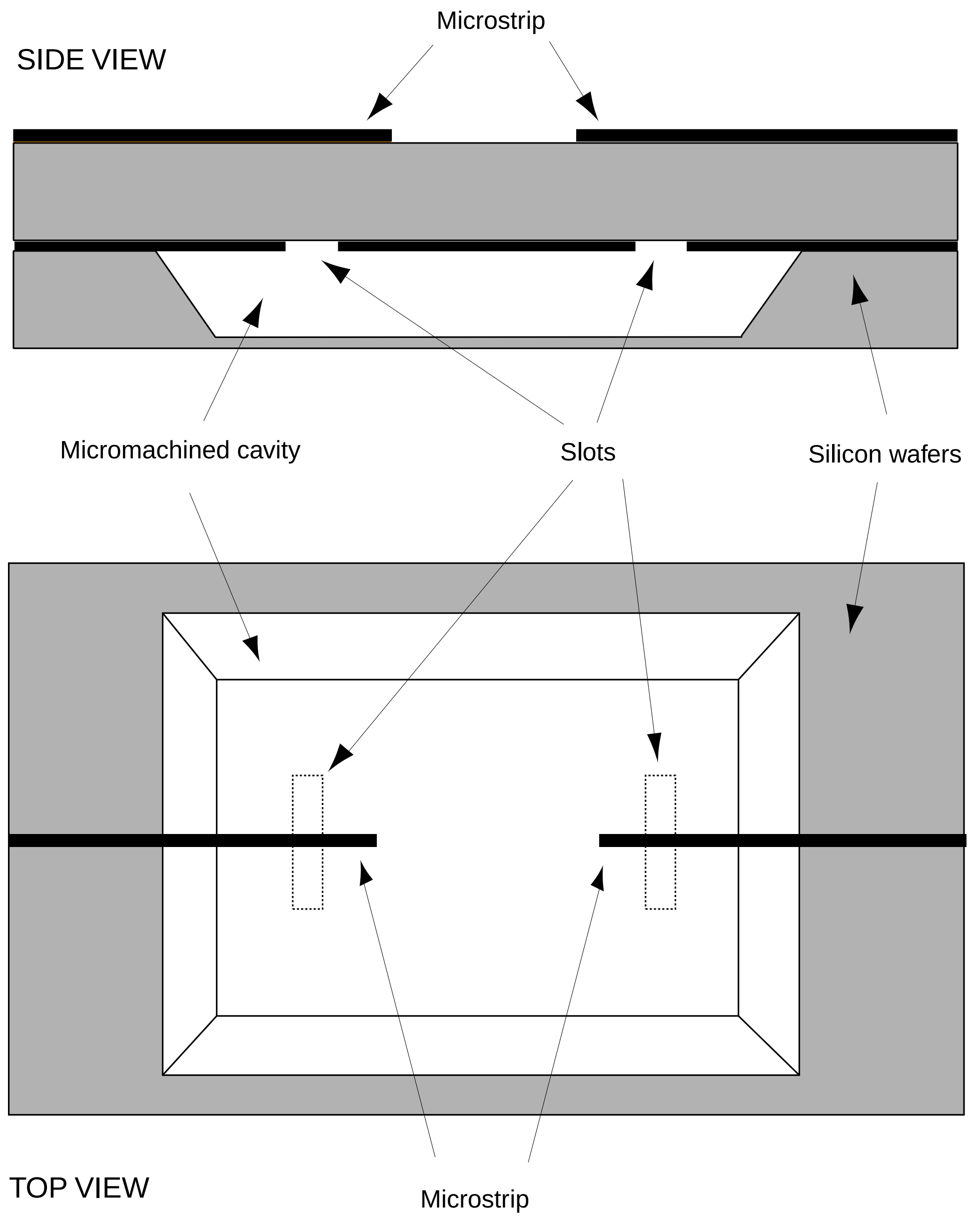

Figure 3.2: Microstrip-fed, slot-coupled, micromachined cavity.

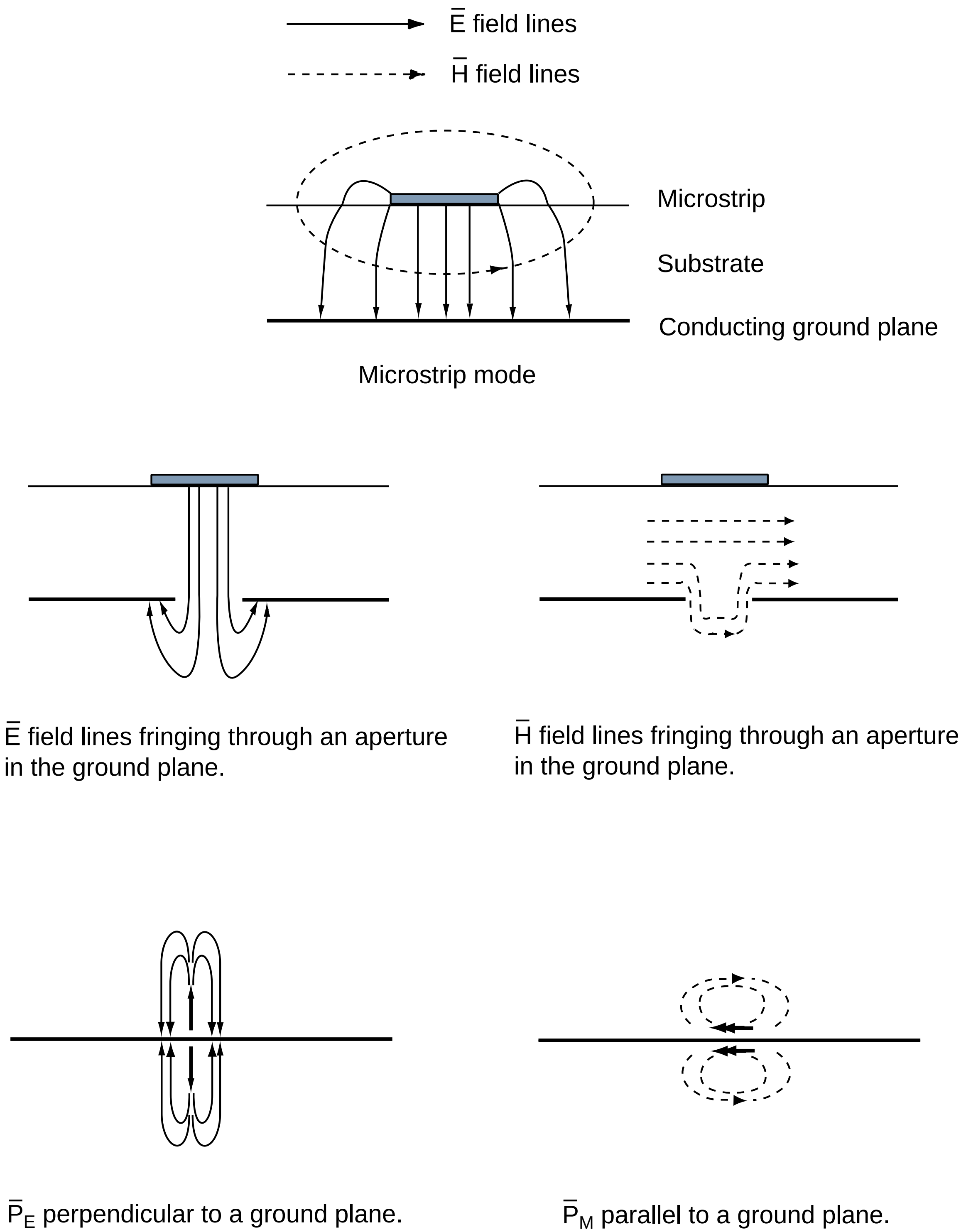

Figure 3.3: Schematic illustrating equivalent electric and magnetic polarization currents for an aperture in a conducting ground plane.

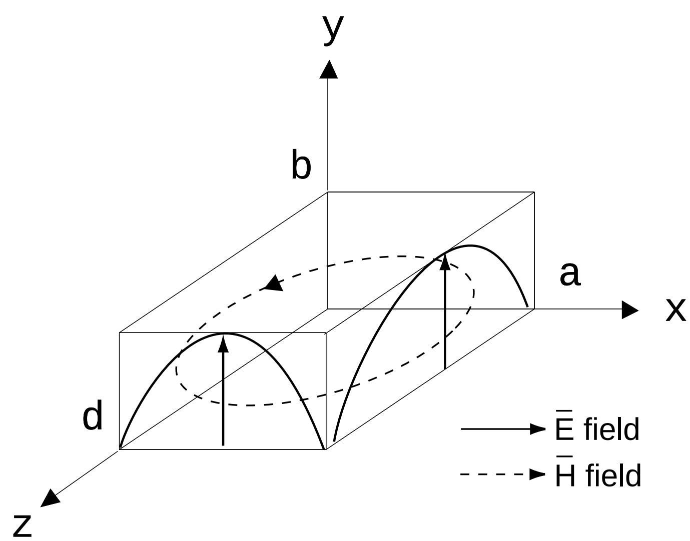

Figure 3.4: Resonant waveguide cavity.

proportional to the fields. $\bar{P}_E$ and $\bar{P}_M$ can be related to the current sources $\bar{J}$ and $\bar{M}$ which can be used to compute the fields on both the input and output sides of the aperture, and continuity of the tangential fields is preserved across the slot. The slot is therefore the source of the fields in a cavity placed below the microstrip ground plane, an impedance transformer whose coupling is proportional to its geometry. In order to prevent unwanted fields and power radiating from the slot, it is operated below cutoff, or in evanescent mode, where it can still couple to the cavity but does not back-radiate into the substrate [23, 56].

A resonant cavity as illustrated in Fig. 3.4 is a waveguide with propagation direction z, width $x = a$, height $y = b$ and shorted at $z = (0, d)$. The transverse electric (TE) and transverse magnetic (TM) to z modes satisfy the boundary conditions on the sidewalls such that $\mathrm{E_{tan}} = 0$. The modes and the boundary conditions provide the information necessary for determining the fields in the cavity.

The rectangular waveguide mode for $\bar{E}$ transverse to z ($\mathrm{TE_{mn}}$) is given by

$$\bar{E}(x, y, z) = \bar{e}(x, y)[A^{+}e^{-j\beta_{mn}z} + A^{-}e^{j\beta_{mn}z}] \tag{3.1}$$

where A^+ and A^- are amplitudes for forward and reverse travelling waves, respectively, and where the $\bar{e}(x, y)$ term encompasses the transverse variations in x and y. The propagation constant β_{mn} is given by

$$\beta_{mn} = \sqrt{k^2 - \left(\frac{m\pi}{a}\right)^2 - \left(\frac{n\pi}{b}\right)^2} \tag{3.2}$$

with the wavenumber $k = \omega\sqrt{\mu\epsilon}$, and μ and ϵ the permeability and permittivity of the waveguide filling material.

The boundary conditions of the cavity require that $\bar{E}(x, y, z) = 0$ at $z = (0, d)$. The boundary condition at $z = 0$ yields $A^+ = A^-$. The boundary condition at $z = d$ yields $\beta_{mn}d = l\pi$, where $l = 1, 2, 3\ldots$, which implies that the cavity must be an integer multiple of a $\lambda_g/2$ at the resonant frequency to support a resonant mode. The cutoff wavenumber is given by

$$k_{mnl} = \sqrt{\left(\frac{m\pi}{a}\right)^2 + \left(\frac{n\pi}{b}\right)^2 + \left(\frac{l\pi}{d}\right)^2} \tag{3.3}$$

where the indices l, m and n are the number of half wavelength variations in the x, y and z directions respectively. The $\mathrm{TE_{mnl}}$ and $\mathrm{TM_{mnl}}$ resonant frequencies are given by

$$f_{mnl} = \frac{ck_{mnl}}{2\pi\sqrt{\mu_r\epsilon_r}} = \frac{c}{2\pi\sqrt{\mu_r\epsilon_r}}\sqrt{\left(\frac{m\pi}{a}\right)^2 + \left(\frac{n\pi}{b}\right)^2 + \left(\frac{l\pi}{d}\right)^2} \tag{3.4}$$

If $a < b \leq d$, the dominant or lowest order cutoff mode will be TE_{101}. For a square cavity $a = d$, and the resonant frequency for TE_{101} becomes

$$f_{101} = \frac{1}{\sqrt{2}a}\frac{c}{\sqrt{\mu_r\epsilon_r}} \tag{3.5}$$

From the total fields of the $\mathrm{TE_{mn}}$ waveguide mode subject to these conditions, the fields of the TE_{101} resonant cavity mode are determined to be

$$\begin{aligned}
E_y &= E_o \sin\left(\frac{\pi x}{a}\right) \sin\left(\frac{\pi z}{d}\right) && (3.6)\\
H_x &= \frac{E_o}{jZ_{TE}} \sin\left(\frac{\pi x}{a}\right) \cos\left(\frac{\pi z}{d}\right) && (3.7)\\
H_z &= \frac{j\pi E_o}{k\eta a} \cos\left(\frac{\pi x}{a}\right) \sin\left(\frac{\pi z}{d}\right) && (3.8)\\
\text{where} \quad E_o &= -2jA^+
\end{aligned}$$

and where Z_{TE} is the wave impedance. A simple illustration of the magnitude of the dominant mode $\bar{E}$ and $\bar{H}$ fields in two coupled square cavities is given in Fig. 3.5. The fields can be seen coupling between the cavities through the short coupling section connecting the cavities, at a location of strong magnetic field.

Using the perturbation method to determine the power dissipated in the cavity walls with finite conductivity, the Q of the resonator due only to the lossy walls is given by

$$Q_{cond} = \frac{(kad)^3 b\eta}{2\pi^2 R_s} \frac{1}{2l^2a^3b + 2bd^3 + l^2a^3d + ad^3} \tag{3.9}$$

where η is the intrinsic impedance and R_s is the conductor surface resistivity and is given by

$$R_s = \sqrt{\frac{\omega\mu_o}{2\sigma}} \tag{3.10}$$

Hence, a higher metal conductivity will result in a higher Q_{cond}. For the dominant mode, $l = 1$, and (3.9) reduces to

$$Q_{cond} = \frac{(kad)^3 b\eta}{2\pi^2 R_s} \frac{1}{2b(a^3 + d^3) + ad(a^2 + d^2)} \tag{3.11}$$

By the symmetry in a and b, it can be shown that the maximum Q can be achieved by a square cavity, $a = d$. The Q of a cavity due only to a lossy dielectric medium is

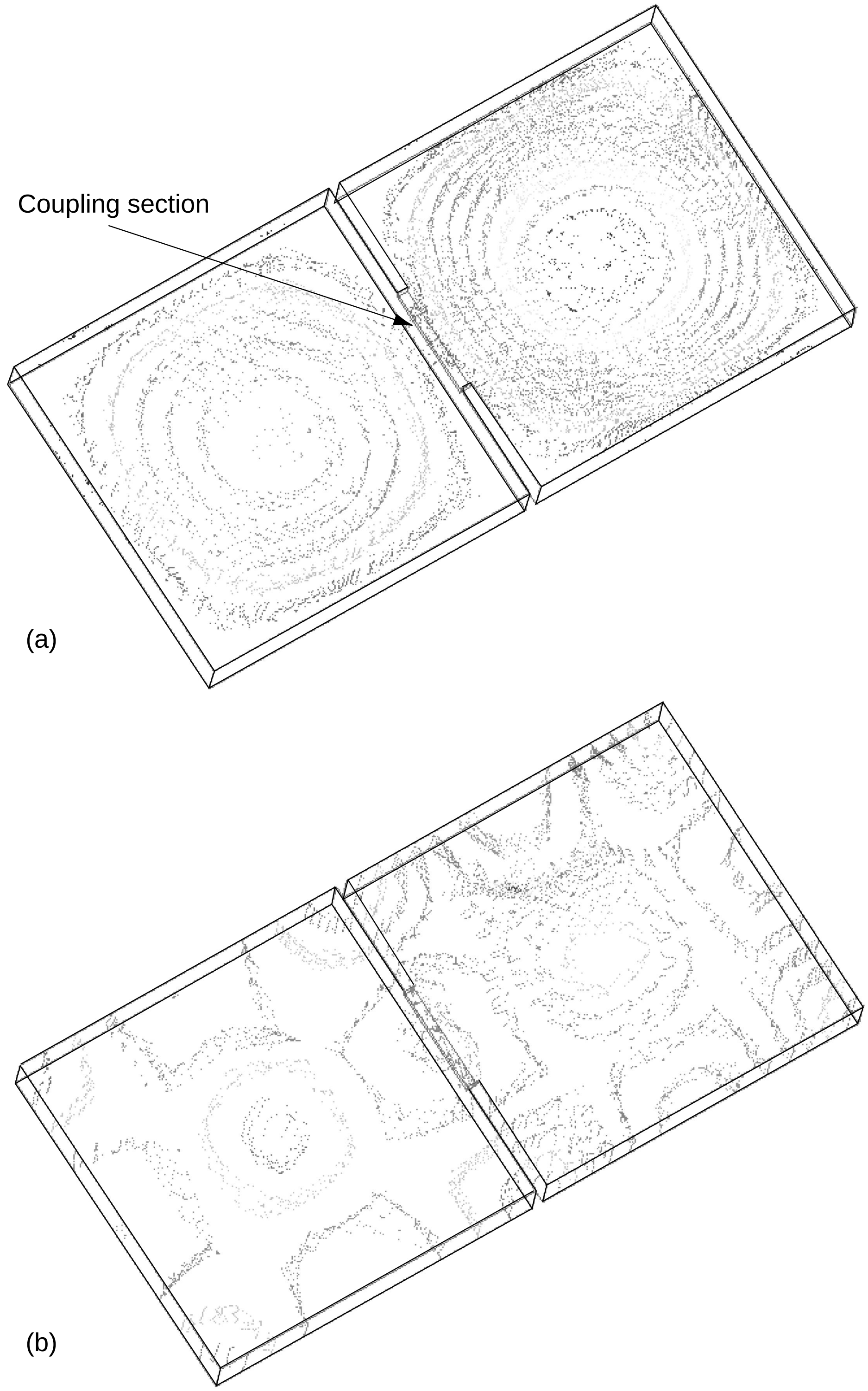

Figure 3.5: Magnitude of the (a) electric and (b) magnetic fields in two coupled cavities.

given by

$$Q_{diel} = \frac{\epsilon'}{\epsilon''} = \frac{1}{\tan\delta} \tag{3.12}$$

and the total unloaded Q is then

$$Q_u = \left(\frac{1}{Q_{cond}} + \frac{1}{Q_{diel}}\right)^{-1} \tag{3.13}$$

For an air-filled (lossless) cavity, the Q_u is simply equivalent to Q_{cond} [23, 57].

The definitions of the unloaded Q, the external Q, the loaded Q and their relationship are given in [58] as the following:

Unloaded Q, Q_u: The Q that would result if the external circuit were loss-free and only power loss due to the R_s of the resonant circuit were considered. The Q_u of a perfect electric conducting, air-filled cavity is infinite.

External Q, Q_e: The Q that would result if the resonant circuit were loss free and only loading by the external circuit were present.

Loaded Q, Q_l: The Q that would result if power loss due to both the external circuit and the resonator are considered. Q_l is smaller than Q_u, where the loading effect can be represented by an additional R_{load} in parallel with R_s of the resonator.

Their relationship is given by

$$\frac{1}{Q_l} = \frac{1}{Q_e} + \frac{1}{Q_u} \tag{3.14}$$

3.2 Recent Micromachined Filter Work

At frequencies above several hundred GHz, machining traditional metal waveguides becomes prohibitive due to the size of the guides, which can be fractions of a millimeter in width and height. An early approach to micromachined rectangular waveguides was presented by McGrath, *et al.* in [59], where WR-10 (75-115 GHz) gold-plated waveguide was fabricated in (110) silicon. The transverse dimensions of the waveguide were 2.54 mm $\times$ 1.27 mm. Silicon nitride (Si_3N_4) was used as an etch mask in KOH anisotropic etching, and the sidewalls were metallized using evaporation of Cr/Au, followed by gold electroplating to 3 μm thick. The measured loss was found to be about 0.04 dB per wavelength at 100 GHz across most of the measured band from 75 to 110 GHz. It is the photolithographic techniques and the micromachining etching techniques that make these small dimensions possible.

Recent micromachined filters include other work in addition to those mentioned in Chapter 1. In [60], a 95 GHz bandpass filter constructed of a microstrip suspended on a dielectric membrane and shielded by a micromachined cavity yielded 3.4 dB insertion loss with a 6.1% bandwidth at 94.7 GHz. An example of a shielded, membrane supported microstrip is sketched in Fig. 3.6. An interdigital filter suspended on a micromachined membrane exhibited 1.7 dB insertion loss at 20.3 GHz with a 6.6% bandwidth in [61]. A micromachined cavity resonator fed by bond wires exhibiting a Q_u of 1117 (compared to 1237 theoretical) at 23.97 GHz, the TE_{011} mode, was demonstrated in [48]. More recently, a probe-fed micromachined cavity consisting of 5 stacked and soldered silicon wafers yielded a resonant cavity at 30 GHz with a measured Q_u of 2050, compared to a theoretical Q_u of 2600. These results, significant contributions to the field of micromachined circuits, demonstrate the feasibility of such work and promote the need to continue 'pushing the envelope' of realizable circuits.

3.3 Foundation: A Single Cavity Resonator

3.3.1 Introduction

The work presented in this thesis began with the investigation of how the bandwidth and the response of a single 10 GHz micromachined cavity resonator would

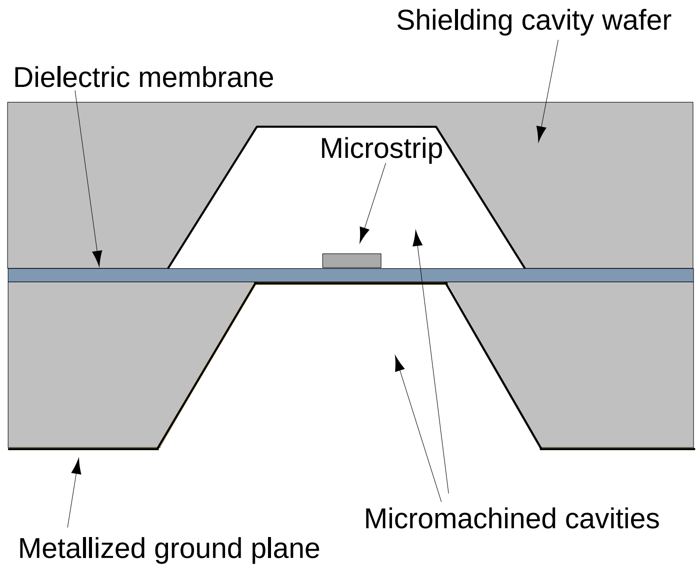

Figure 3.6: Dielectric membrane supported microstrip with shielding cavity wafer.

be affected by altering the positions of the coupling slots. Theory and experiment indicate that by changing the placement of the slots relative to the cavity, bandwidth and insertion loss are affected.

Originally in [1] the slots are placed at 1/4 and 3/4 of the cavity length, refer to Fig. 3.2. In [49], the slots were placed closer together, at 3/8 and 5/8 of the cavity length. The cavity is 16 mm $\times$ 32 mm and the slots are 7 mm $\times$ 0.7 mm approximately, placed 8 mm apart, center-to-center. Theoretical results for packaging of the resonator were presented and compared to the non-packaged case.

3.3.2 Simulations, Fabrication and Measurements

The resonator was fabricated using two high resistivity 500 μm thick silicon wafers, with plasma-enhanced chemical vapor deposition (PECVD) silicon nitride grown on the wafers front and back sides to be used as an etch mask. The microstrip lines were printed on the top surface of the first wafer by gold electroplating to a total thickness of 6 μm. CPW to microstrip transitions were included in order to measure the resonator with on-wafer probing. The ground planes of the CPW and microstrip lines are set at the same potential by via holes as described in Chapter 2. The cavity was fabricated on the second wafer by using TMAH anisotropic etching up to a depth of 470 μm and is then metallized and gold plated to a thickness of approximately 3 μm. The two wafers were finally bonded together using silver epoxy that was cured at 150° C.

The fabricated resonator was measured using a TRL (Thru-Reflect-Line) calibration referenced at the slots and the results are compared with theory in Figs. 3.7 and 3.8. The theoretical results were obtained by modeling in HFSS. There is very good agreement between the simulated and measured responses. The small discrepancy (0.95%) in the resonant frequency can be attributed to fabrication tolerances. The measured resonator exhibits a bandwidth of 2% (210 MHz) at a resonant frequency of 10.525 GHz. The insertion loss, after de-embedding the loss on the two open end stubs extending beyond the center of the slots, is 1.1 dB. Comparing these results to those presented in [1], we observe a 58% decrease in the bandwidth (from 500 to 210 MHz) and a 0.74 dB increase in insertion loss, see Fig. 3.9. These results indicate that by altering the positions of the coupling slots relative to the cavity we can change (narrow or widen) the bandwidth of the resonator at the price of changing the loss. This of course is expected since the Q_u of the cavity is determined by the geometry and conductivity of the cavity, and is the same in all cases. Hence, a narrowing in the bandwidth will result in a loss increase. This can be explained by the relationship between the Q_u and Q_e, which includes the loading due to the coupling slot. With some algebra, (3.14) can be re-written as

$$Q_u = \frac{1}{FBW}\frac{Q_e + Q_u}{Q_e} \quad \text{where} \quad Q_l = \frac{1}{FBW} \tag{3.15}$$

and FBW is the fractional bandwidth. If the Q_u is held constant and the external

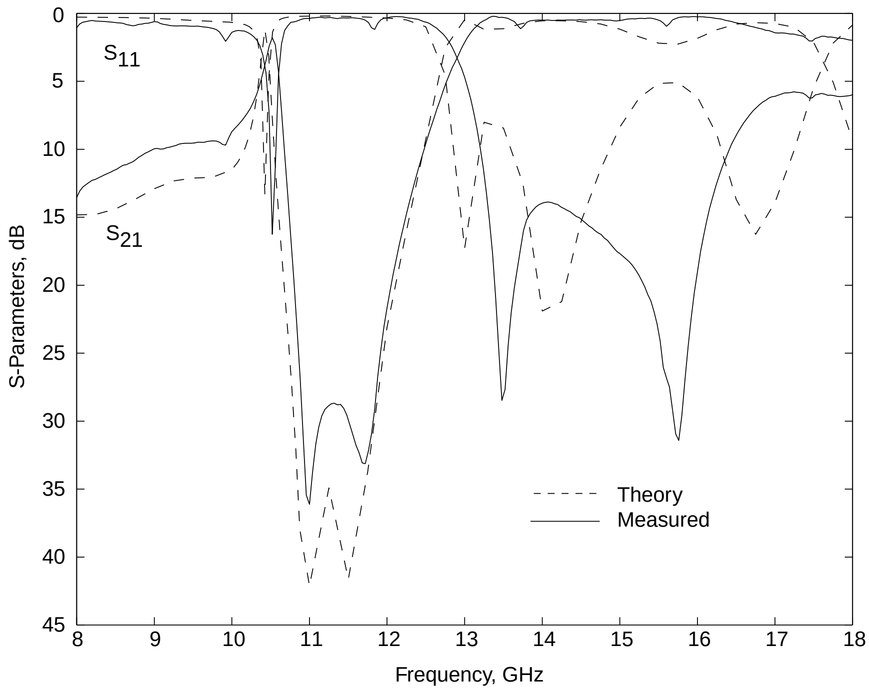

Figure 3.7: Comparison of the modeled and measured results of the micromachined resonator with altered slot positions.

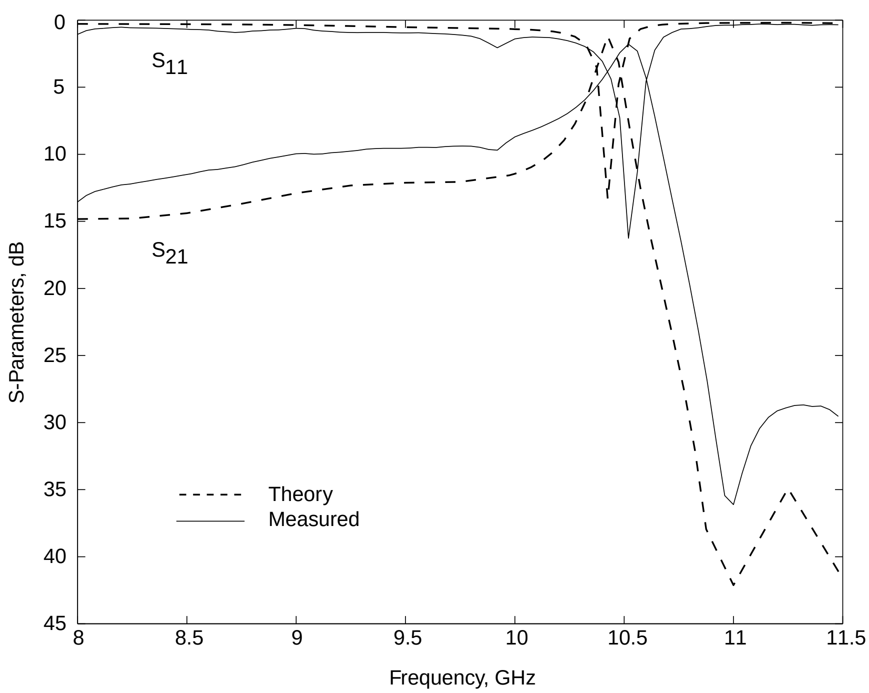

Figure 3.8: Close-up of the modeled and measured results.

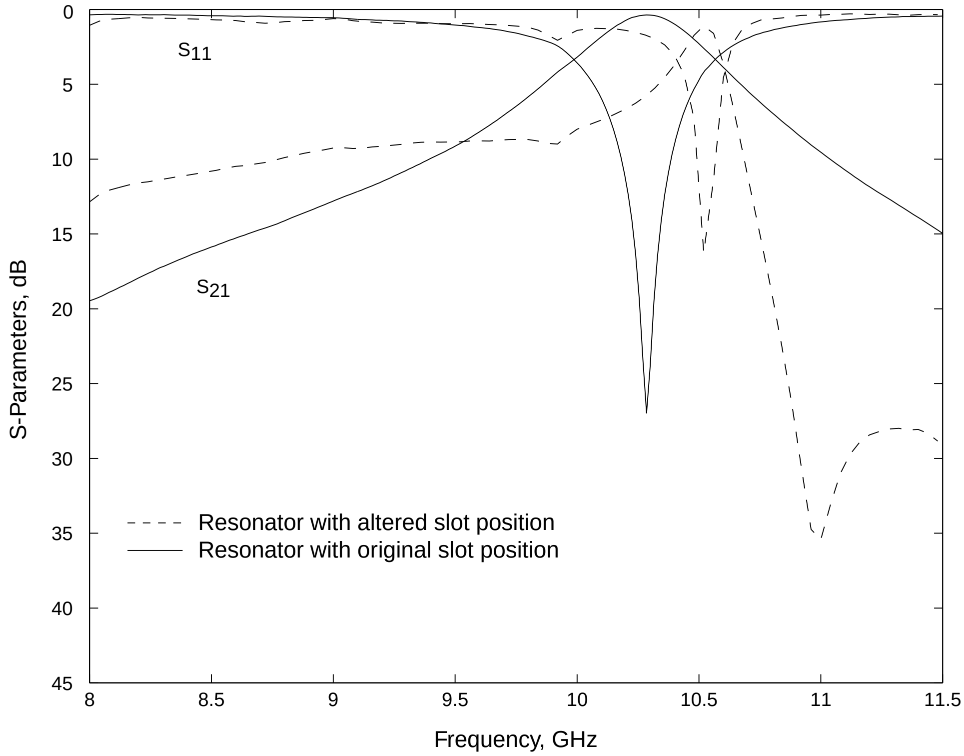

Figure 3.9: Comparison of the measured results for the resonator with altered slot positions and with original slot positions [1].

coupling (the slot in this case) is changed, then the Q_e and the bandwidth must change. Specifically, for an increase in the Q_e, a decrease in the fractional bandwidth will be seen.

From Fig. 3.8 a slight asymmetry in the response around the resonance is observed. This is due to power coupling from one microstrip to another directly and via substrate modes due to the proximity of the two lines (0.4 λ_g). In order to eliminate this effect and make the response more symmetric around resonance we can use standard packaging techniques [62] to isolate the microstrip lines from one another, both on top and inside the substrate. For this purpose an HFSS simulation was run where one perfect electric conductor (PEC) plane was placed on top of the structure and another was placed between the two lines shorting the top PEC to the slot plane. Results, shown in Fig. 3.10, demonstrate that packaging reduces the suspected coupling

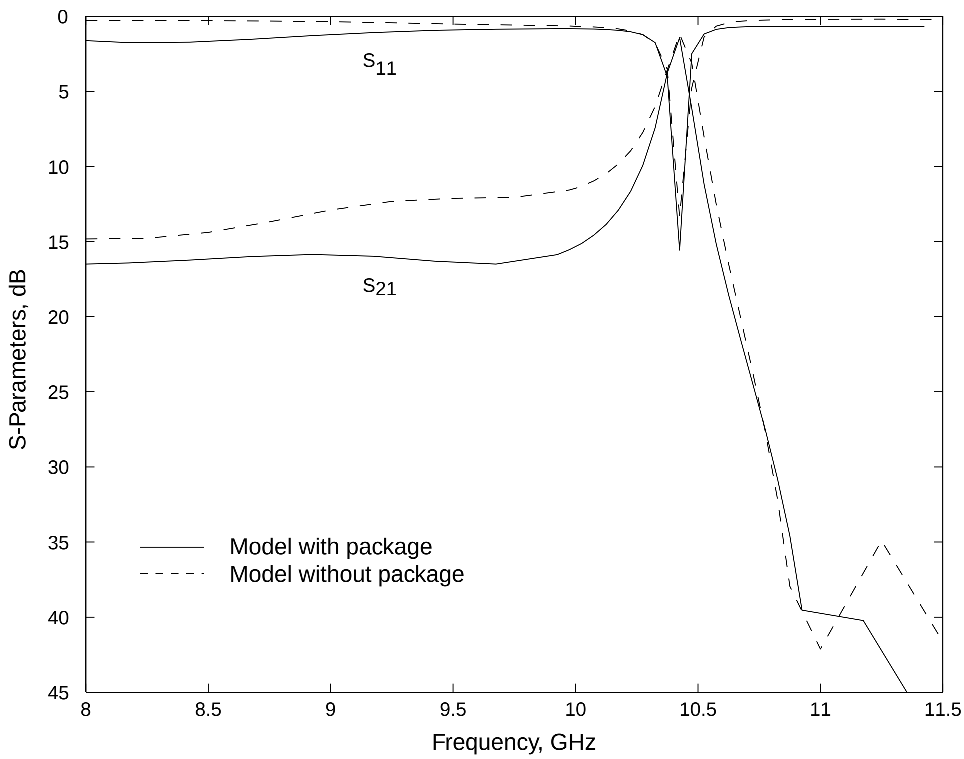

Figure 3.10: Modeled response of the resonator with and without packaging.

occurring below 10.3 GHz by as much as 4 dB. In addition, we observe that there is a small and flat coupling of about -16 dB below 10 GHz that can be attributed to evanescent modes that are significant when the slots are placed close together (0.75 λ_g).

3.4 Summary

In this chapter we have discussed the initial microstrip to slot to cavity modeling. The principles governing the excitation of resonant modes in the cavity, as well as the important quality factor Q and its definition in terms of power dissipation have been presented. The contributions of recent micromachined filters by other authors and the initial work by this author have been discussed. On the initial single micromachined resonator work, the effects of altering the slot positions have been presented. Although the Q_u is determined by the cavity itself, the bandwidth is determined by the relative position of the slots with a reduction in bandwidth and increase in loss occurring as the slots are placed close together. The close proximity of the slots also produces direct coupling between the microstrip lines that can be eliminated with appropriate packaging of the structure.

The next logical step is to demonstrate a multiple, micromachined cavity filter in silicon. The first of these filters, a 10 GHz filter constructed of slot-coupled micromachined cavities in silicon, is presented in Chapter 4. Well-established filter theory and design will first be discussed and then related to this novel synthesis format.

CHAPTER 4

A Vertically Integrated Micromachined Cavity Filter

The most exciting phrase to hear in science, the one that heralds new discoveries, is not "Eureka" but "That's funny..."

Isaac Asimov

4.1 General Filter Design

A FILTER is a linear time-invariant circuit whose primary purpose is to pass desired frequencies and reject all others. An ideal filter would have infinite transmission attenuation in the stopband, zero transmission attenuation in the passband, and a perfect linear phase response with respect to frequency, i.e., no phase distortion. Network synthesis methods of filter design typically start with a desired transfer function as a function of complex frequency. From the transfer function the input impedance is found, a bit of algebra such as partial-fraction expansion is performed, and hence the poles, zeros and prototype elements are determined. These elements will give exact responses for lumped element filters, but only approximations for microwave filters. Therefore some tuning of the microwave filter will be necessary [63, 64].

For example, the magnitude function of an all-pole (no finite zeros) low-pass transfer function is given by

$$|H(j\omega)| = \frac{1}{\sqrt{1+\epsilon^2\Psi_n^2(\omega)}} \tag{4.1}$$

where $0 < \epsilon < 1$ and $\Psi_n(\omega)$ is an n_{th} order polynomial of only even or only odd powers of ω. One kind of filter described by this transfer function is the Chebyshev, so named for the class of functions with an equiripple property. The function $\Psi_n(\omega)$ is replaced by the Chebyshev polynomials yielding

$$|H(j\omega)| = \frac{1}{\sqrt{1+\epsilon^2 C_n^2(\omega)}} \tag{4.2}$$

where ϵ now determines the passband ripple height.

The poles as determined by the Chebyshev polynomials are given by

$$P_1 = -\sin\left(\frac{2k-1}{2n}\pi\right)\sinh\left(\frac{1}{n}\sinh^{-1}\frac{1}{\epsilon}\right) + j\cos\left(\frac{1}{2n}\pi\right)\cosh\left(\frac{1}{n}\cosh^{-1}\frac{1}{n}\right) \tag{4.3}$$

where $k = 1, 2, 3 \ldots n$ and n is the number of reactive elements (resonators). The low-pass prototype element values are determined from the poles and the ripple level, and are tabulated in many sources including [63, 64]. From these element values a low-pass prototype filter can be constructed such as the schematic shown in Fig. 4.1.

In microwave filter design, it is convenient to use a modified prototype that consists of identical series resonators coupled by impedance inverters, such as that shown in Fig. 4.2 or its dual. It's dual is of course a circuit using shunt resonators and admittance inverters. Series resonators exhibit zero reactance at resonance, and shunt resonators exhibit zero susceptance at resonance. The conversion from Fig. 4.1 to Fig. 4.2 is accomplished by considering the following: a shunt capacitance with an impedance inverter on either side looks like a series inductance from the external

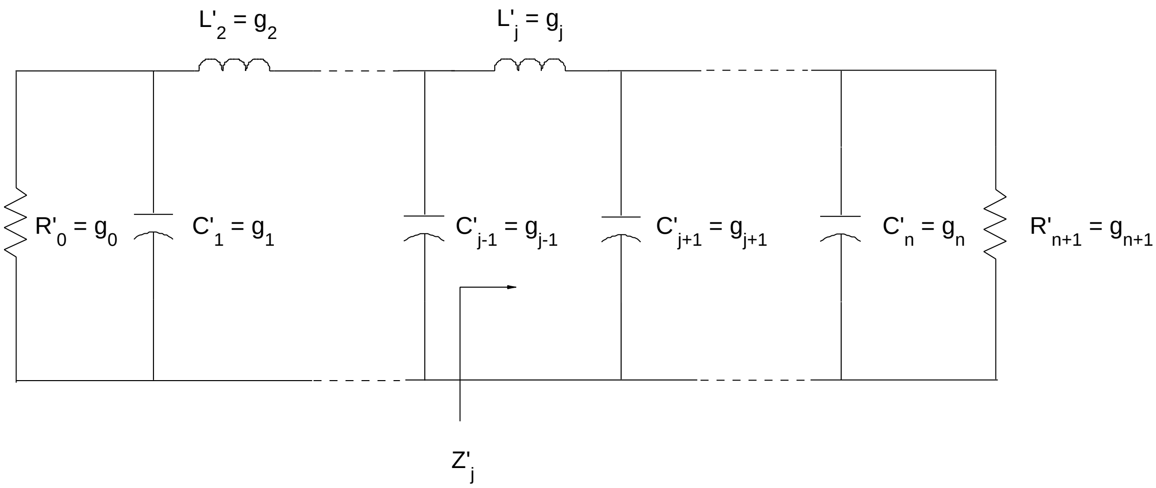

Figure 4.1: Low-pass prototype filter schematic.

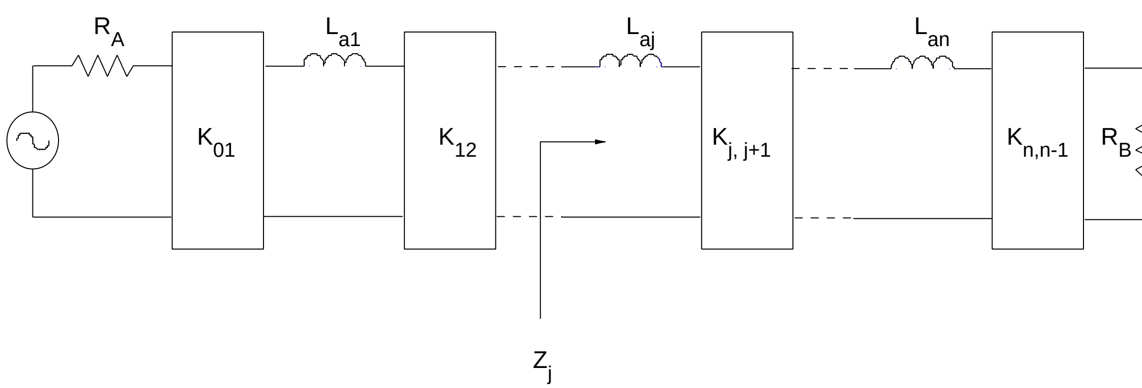

Figure 4.2: Modified low-pass prototype schematic using series resonators and impedance inverters.

terminals. Referring to Fig. 4.1

$$Z'_j = j\omega L_j + \frac{1}{j\omega C_{j+1}} \tag{4.4}$$

and referring to Fig. 4.2,

$$Z_j = j\omega L_{aj} + \frac{K^2_{j,j+1}}{j\omega L_{aj+1}} \tag{4.5}$$

Z'_j and Z_j must be the same save for an impedance scaling factor,

$$\begin{aligned} Z_j &= \frac{L_{aj}}{L_j} Z'_j \\ &= \frac{L_{aj}}{L_j}\left[j\omega L_j + \frac{1}{j\omega C_{j+1}}\right] \\ &= j\omega L_{aj} + \frac{L_{aj}}{j\omega L_j C_{j+1}} \end{aligned} \tag{4.6}$$

Hence we have

$$\begin{aligned} K_{j,j+1}|_{k=1 \text{ to } n-1} &= \sqrt{\frac{L_{aj} L_{aj+1}}{L'_j C'_{j+1}}} \\ &= \sqrt{\frac{L_{aj} L_{aj+1}}{g_j g_{j+1}}} \end{aligned} \tag{4.7}$$

and similarly we can determine

$$K_{01} = \sqrt{\frac{R_A L_{a1}}{g_0 g_1}} \tag{4.8}$$

$$K_{n,n+1} = \sqrt{\frac{L_{an} R_B}{g_n g_{n+1}}} \tag{4.9}$$

It simply remains to perform a frequency transformation to achieve a bandpass filter from the low-pass prototype. The transformation can be given by

$$\omega' = \frac{\omega'_1}{\Delta}\left(\frac{\omega}{\omega_o} - \frac{\omega_o}{\omega}\right) \quad \text{where} \quad \Delta = \frac{\omega_2 - \omega_1}{\omega_o} \quad \text{and} \quad \omega_o = \sqrt{\omega_1 \omega_2} \tag{4.10}$$

and where ω' is the frequency of the low-pass prototype to be replaced, ω_1' is the frequency of the ripple band edge of the low-pass prototype, Δ is the bandpass ripple bandwidth (corresponding to the prototype ω_1'), and ω_o is the resonance frequency, as defined by the geometric mean of ω_1 and ω_2, which are the lower and upper ripple band edge frequencies, respectively.

The reactance slope of any series resonator is given by

$$\alpha = \frac{\omega_o}{2} \frac{dX}{d\omega}\bigg|_{\omega_o} \tag{4.11}$$

where X is the reactance of the resonator. Then, performing the frequency transformation with the aid of (4.11),

$$jX_k = j\frac{\omega_1'}{\Delta}\left(\frac{\omega}{\omega_o} - \frac{\omega_o}{\omega}\right) L_k \tag{4.12}$$

and

$$\alpha_j = \frac{\omega_o}{2}\frac{d}{d\omega}\left[\frac{\omega_1'}{\Delta}\left(\frac{\omega}{\omega_o} - \frac{\omega_o}{\omega}\right) L_k\right]_{\omega_o} \tag{4.13}$$

yields

$$L_{a1} = \frac{\alpha_1 \Delta}{\omega_1'} \tag{4.14}$$

$$L_{an} = \frac{\alpha_n \Delta}{\omega_1'} \tag{4.15}$$

$$L_{aj} = \frac{\alpha_j \Delta}{\omega_1'} \tag{4.16}$$

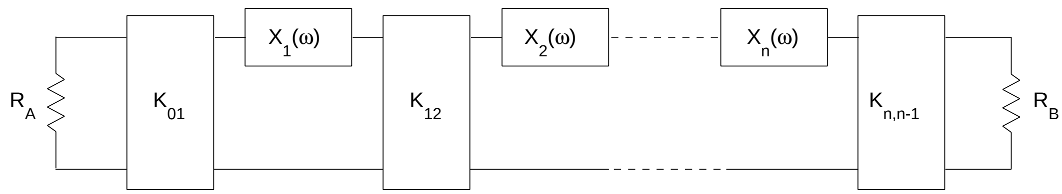

Figure 4.3: Generalized bandpass filter schematic.

and then

$$
\begin{aligned}
K_{01} &= \sqrt{\frac{R_A \alpha_1 \Delta}{g_0 g_1 \omega_1'}} && (4.17)\\
K_{j,j+1} &= \frac{\Delta}{\omega_1'}\sqrt{\frac{\alpha_j \alpha_{j+1}}{g_j g_{j+1}}} && (4.18)\\
K_{n,n+1} &= \sqrt{\frac{\alpha_n \Delta R_B}{g_n g_{n+1} \omega_1'}} && (4.19)
\end{aligned}
$$

A generalized bandpass filter is given by Fig. 4.3, as described by the equations above.

The use of the lumped element low-pass prototype to distributed element bandpass filter through the use of the network synthesis method and impedance and frequency transforms works well for planar transmission line filters. However, for direct-coupled cavity resonator filters, another approach is more convenient and requires knowledge of only the external Q, Q_e, and the coupling coefficients $k_{j,j+1}$ between each resonator. Both of these values can be described in terms of the prototype g_j values and the ripple bandwidth Δ.

The coupling coefficients are given by

$$k_{j,j+1} = \frac{K_{j,j+1}}{\sqrt{\alpha_j \alpha_{j+1}}} = \frac{\Delta}{\omega_1' \sqrt{g_j g_{j+1}}} \tag{4.20}$$

The Q of a series resonator with resistance R is given by

$$Q = \frac{\alpha}{R} \tag{4.21}$$

The inverter K_{01} from Fig. 4.2 reflects an impedance of K_{01}^2/R_A to the resonator. The loaded Q can be given by

$$Q_l = \frac{\alpha}{K_{01}^2/R_A + R} \tag{4.22}$$

If R=0 ($Q_u = \infty$), then Q_l becomes Q_e

$$Q_e = \frac{\alpha}{K_{01}^2/R_A} \tag{4.23}$$

Hence the input (A) and the output (B) Q_e are given by

$$Q_{eA} = \frac{\alpha_1}{K_{01}^2/R_A} = \frac{g_0 g_1 \omega_1'}{\Delta} \tag{4.24}$$

$$Q_{eB} = \frac{\alpha_n}{K_{n,n+1}^2/R_B} = \frac{g_n g_{n+1} \omega_1'}{\Delta} \tag{4.25}$$

If lumped element resonators and frequency-independent inverters were used in the practical realization of the filter, the above equations would be exact. However, for frequency dependent components such as coupling apertures and waveguides, the equations are good approximations only, and only for bandwidths of a few percent or less. The assumption that $Q_u = \infty$ also contributes to this approximation. Measured or modeled coupling coefficients and Q_e's can be tuned until they agree with the design goals given by these equations [63].

A model of two identical resonant cavities coupled by an aperture of arbitrary thickness in their common wall is shown in Fig. 4.4 [65, 66]. The equivalent circuit is also shown, as is a circuit with the coupling reactance divided into two parts

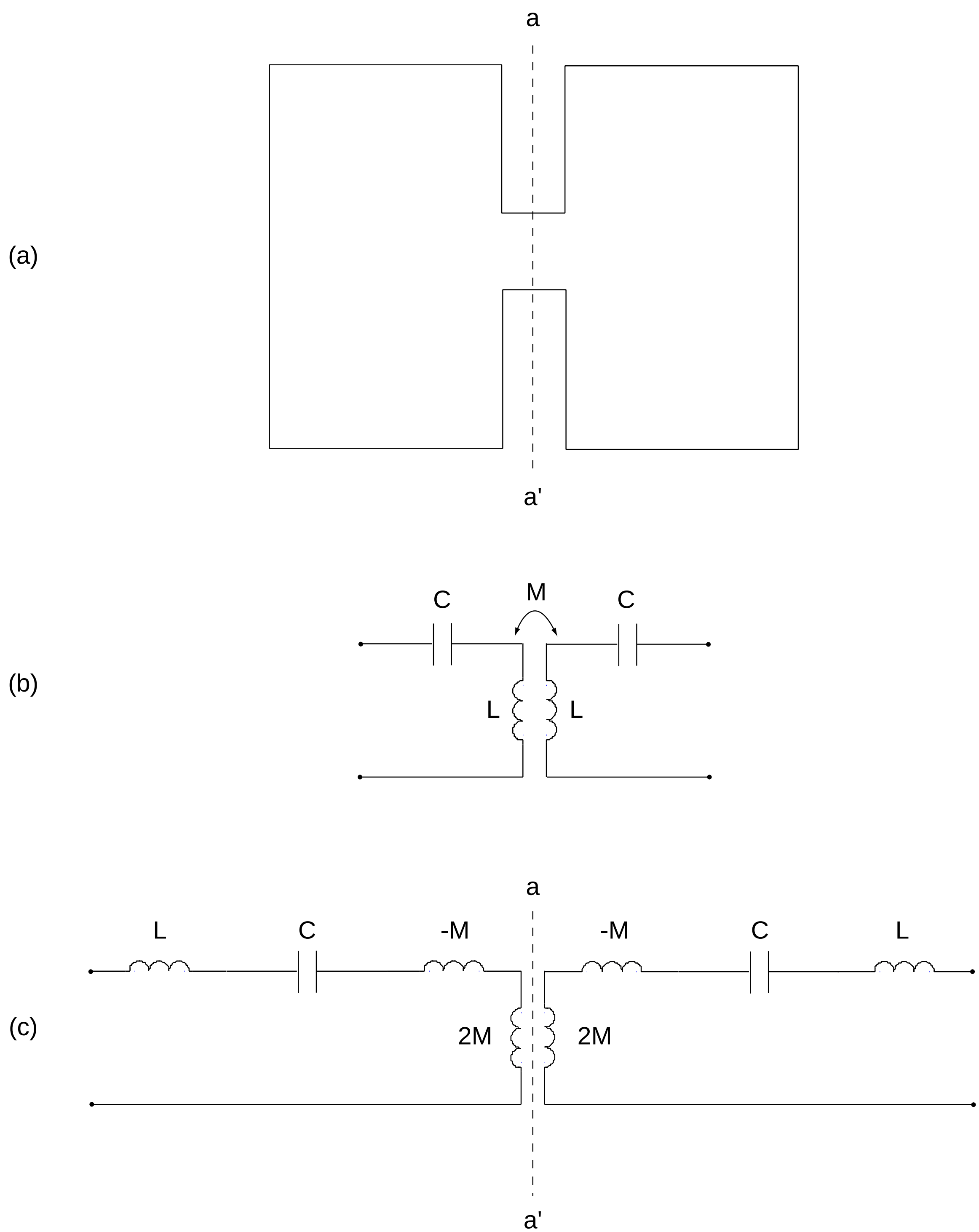

Figure 4.4: (a) Resonant cavities coupled by an aperture of arbitrary thickness in their common wall. (b) Equivalent circuit. (c) Equivalent circuit with coupling reactance divided in two. Symmetry plane $a - a'$ corresponds as shown to cavity structure.

with a symmetry plane at $a - a'$. Inductances used to represent coupling slots, as in a transformer, represent the self-inductances due to the fringing fields caused by the aperture discontinuity in the ground plane, the junction between the feeding transmission line and the cavity [67]. This characteristic, as is the active equivalent circuit, is independent of the type of coupling geometry. It has been stated [66] that for each cavity resonance, there are two oscillation states, one corresponding to an electric wall or short circuit at the symmetry plane and the other corresponding to a magnetic wall or open circuit at the symmetry plane. From the equivalent circuit, the following "oscillation state" resonances can be determined,

$$f_e = \frac{1}{2\pi\sqrt{(L-M)C}} \qquad \text{(electric wall)} \tag{4.26}$$

$$f_m = \frac{1}{2\pi\sqrt{(L+M)C}} \qquad \text{(magnetic wall)} \tag{4.27}$$

By solving for

$$\frac{f_e^2 - f_m^2}{f_e^2 + f_m^2} \tag{4.28}$$

we achieve

$$\frac{f_e^2 - f_m^2}{f_e^2 + f_m^2} = \frac{M}{L} = k \tag{4.29}$$

which is the definition of the coupling coefficient k as defined from the equivalent circuit. The uncoupled, identical resonators each have the same resonance frequency f_o defined by the same wavenumbers, or eigenvalues. When the cavities are coupled, the modes become degenerate and the frequencies split as determined by f_e, which shifts higher in frequency due to L-M and f_m, which shifts lower in frequency due to L+M. An illustration is given by coupling two cavities by a slot as illustrated in Fig. 4.10b, and which will be discussed in some detail in Section 4.2.2. Shown in Fig. 4.5 are the insertion loss curves, S_{21}, for two coupled cavities whose individual resonance frequency f_o is 10.12 GHz. The mode splitting is illustrated by the two

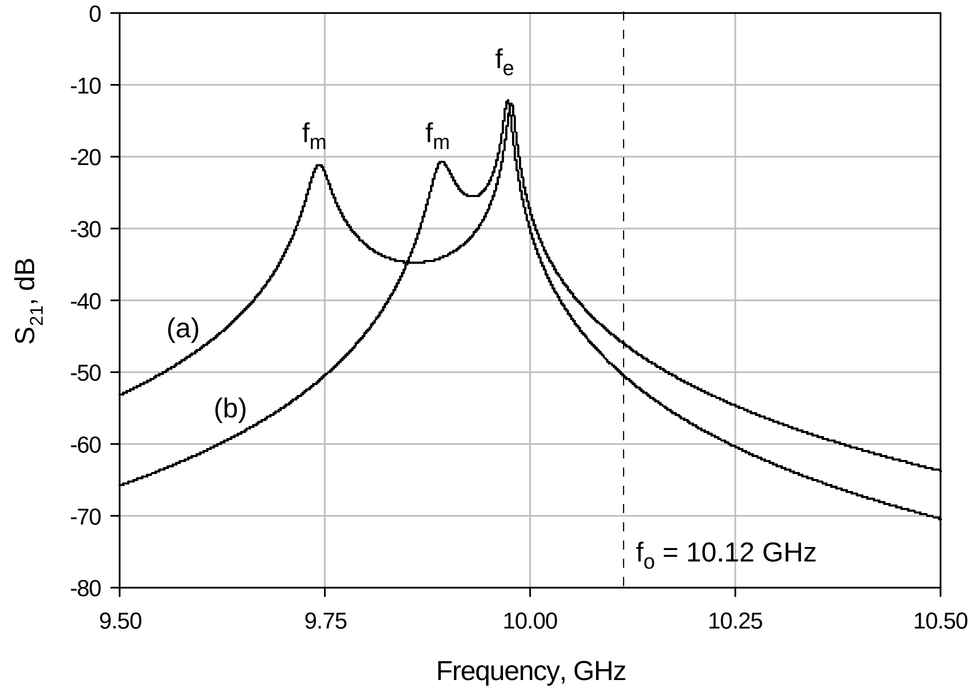

Figure 4.5: Insertion loss curves for two slot-coupled cavities. The slot length dimensions are 5.921 mm for curve (a) and 4 mm for curve (b). Resonance frequency f_o for both cavities is 10.12 GHz.

frequency peaks at 9.742 GHz (f_m) and 9.976 GHz (f_e) for one curve, and 9.892 GHz (f_m) and 9.972 GHz (f_e) for the second curve. Two curves are shown for different slot lengths, 5.921 mm and 4 mm, to demonstrate the shifting of the pole for different coupling strengths. The smaller slot yields weaker coupling, and its response shown by curve (b) approaches that which would be seen for a single cavity. The coupling is strongly magnetic as is evident by the proximity of the upper frequencies f_e to the resonance f_o. The longest dimension of the aperture is parallel to the magnetic field in the cavities.

If the external coupling for a filter design is calculated from the prototype parameters, such as by (4.25), then it is the correct, or critical coupling for that particular filter design. For critical coupling, the VSWR (voltage standing-wave ratio) at resonance, $V_o(f_o)$, is equal to 1. The unloaded and external Q's are given by

$$Q_u = \frac{Nf_o}{\Delta f} \tag{4.30}$$

$$Q_e = \frac{Q_u}{V_o} \quad \text{for the over-coupled case} \tag{4.31}$$

$$Q_e = V_o Q_u \quad \text{for the under-coupled case} \tag{4.32}$$

Both cases of Q_e reduce to Q_u for critical coupling. Hence,

$$Q_e = \frac{Nf_o}{\Delta f} \tag{4.33}$$

where N=1 if Δf is measured at the 3 dB bandwidth (half-power) point [63, 67]. The 3 dB point can be computed from the phase of S_{11} as given by [67]. The phase method, which eliminates the need to measure the VSWR, involves the measurement of the voltage nodes with respect to a reference plane as a function of the S_{11} phase angle versus frequency plot. Two approaches are possible; one method tunes the cavity off resonance, the other tunes the signal source through resonance (sweeps the frequency). If the second method is used, the feed line must be de-embedded, i.e., the distance to the displacement of the detuned-open is subtracted from each phase point. The detuned-open positions are 1/2 wavelength apart and represent reference planes along the feeding transmission line where the self-reactance of the coupling structure goes to infinity. At resonance, the de-embedded curve passes through 0° phase. The curve passes through ±90° at points designated δ_1 and δ_2 where

$$\delta_1 = \frac{f_1 - f_o}{f_o} \tag{4.34}$$

$$\delta_2 = \frac{f_2 - f_o}{f_o} \tag{4.35}$$

These points correspond to the S_{11} phase angle = 90° when the feed line is de-embedded.

Using the information given by the phase plots for the over- and under-coupled cases, it is possible to solve for Q_e,

$$Q_e = \frac{1}{\delta_1 - \delta_2} = \frac{f_o}{f_1 - f_2} = \frac{f_o}{\Delta f} \tag{4.36}$$

So from a de-embedded single resonator, the Q_e due to the coupling structure can be determined by the phase of S_{11}. An illustration of this method is demonstrated in Fig. 4.6. The figure shows a resonant cavity coupled by a microstrip-fed slot aperture. The dotted arrow indicates the length of port de-embedding to the detuned-open on the microstrip line, where the H-field goes to zero (maximum E-field) [67]. Figure 4.7 shows the S_{11} phase plot for such a structure, with both the original port location data and the de-embedded data displayed.

The theoretical insertion loss of a filter, $(\Delta L_A)_o$, which is defined as the increase in midband attenuation due to finite conductivity, is given by

$$(\Delta L_A)_o = 8.686 \frac{C_n \omega_1'}{\Delta Q_u} \qquad \text{dB} \tag{4.37}$$

C_n is a function of the number of poles and the passband ripple. Q_u is degraded (from theoretical values) due to metal surface roughness, corrosion and oxidation, and losses due to the coupling elements which are difficult to predict. Hence, practical insertion loss never measures as low as theory will predict [63].

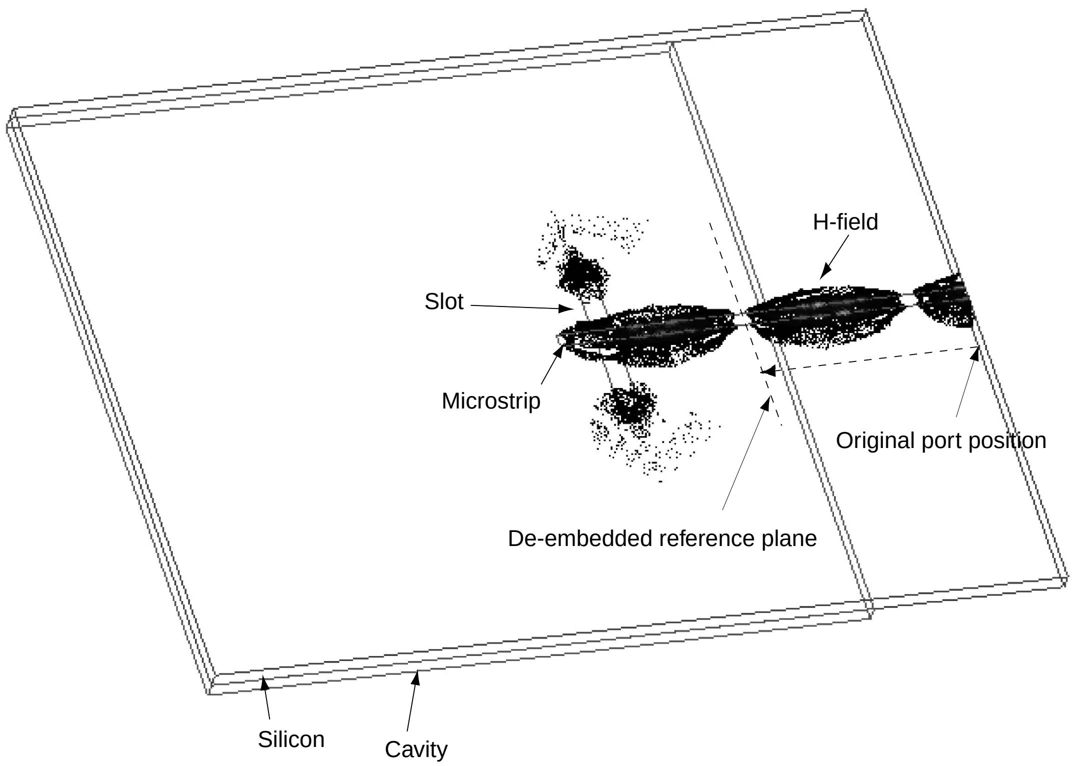

Figure 4.6: Microstrip-fed, slot-coupled, micromachined cavity showing magnetic field strength along microstrip line. Dotted line indicates the length of the port de-embedding.

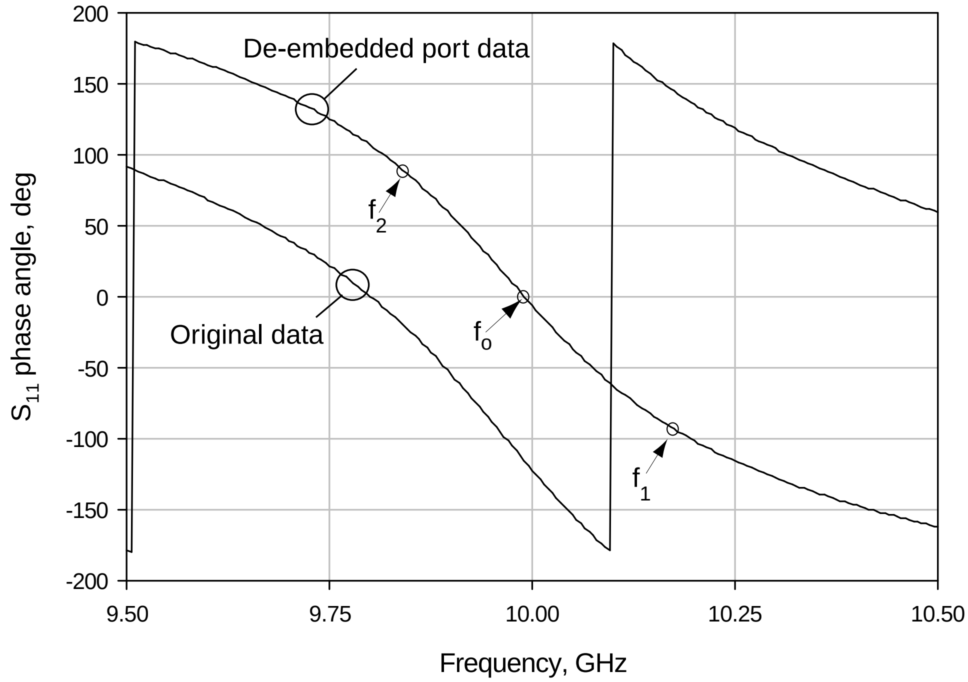

Figure 4.7: Reflection coefficient phase angle. Both original and de-embedded data are shown. $\Delta f = f_1 - f_2$ and f_o are indicated.

4.2 Vertically Integrated Micromachined Filter

4.2.1 Introduction

The novel character of the micromachined filter lies in its structure, which consists of a microstrip feed to cavities via slot apertures, and 3 vertically stacked slot-coupled cavities. The cavities are essentially reduced-height waveguide resonators, a unique three-dimensional concept in silicon. The measured results are presented and compared to an HFSS model. The simulated model has a bandwidth of 4% with an insertion loss of 0.9 dB at 10.02 GHz. The measured filter yields a 3.7% bandwidth with a de-embedded insertion loss of 2.0 dB at 10.01 GHz. Various loss mechanisms are examined to explain the difference between simulated and measured insertion loss.

A low-loss, high-Q resonator cavity fabricated in a planar environment using standard micromachining techniques was demonstrated in [1]. This chapter presents the first demonstration of a 3-pole filter using this high-Q micromachined resonator. Vertical integration was chosen to minimize the horizontal dimensions of the circuit, and to demonstrate top to bottom slot coupling between each cavity. A filter synthesis is developed, and the validity of the process is demonstrated as a filter that consists of three slot-coupled, vertically integrated resonators as shown in Fig. 4.8 and Fig. 4.9.

4.2.2 Design and Simulation

The design is accomplished with the aid of HFSS. A Chebyshev filter with a 0.1 dB ripple, three resonators and a 4% bandwidth is chosen as a demonstration vehicle for the proposed concept.

Recall that the Q_e is defined as the Q that would result if the resonant circuit were loss free and only loading by the external circuit were present [58]. This relationship can be used to determine external coupling. First, Q_e values are determined by using (4.24) and (4.25), where Q_{eA} is the external coupling from the input microstrip line to the circuit, and Q_{eB} is the external coupling from the n^{th}, or last, resonator to the output microstrip line. For an odd number of resonators, as in this work, the g values are symmetric, so $Q_{eA} = Q_{eB}$.

Through the simulations of a microstrip line coupled via a slot to the micromachined cavity (see HFSS model cross section in Fig. 4.10a), the relationship between the length of the external slots and the phase response of S_{11} is determined using (4.36). Simulations are run for slots of constant width but varying length, and Q_e is plotted versus slot length, Fig. 4.11. Nonlinear regression is used to determine a curve fitted to the data, and a slot of 5.6 mm $\times$ 0.635 mm is chosen. Hence, external coupling as determined by slot length is related to Q_e from (4.36), which is related to the desired prototype Q_e as determined by (4.24) and (4.25).

The desired internal coupling coefficients $k_{j,j+1}$ between the j^{th} and the $j^{th}+1$ resonators are calculated using (4.20). Through the simulation of two coupled cavities

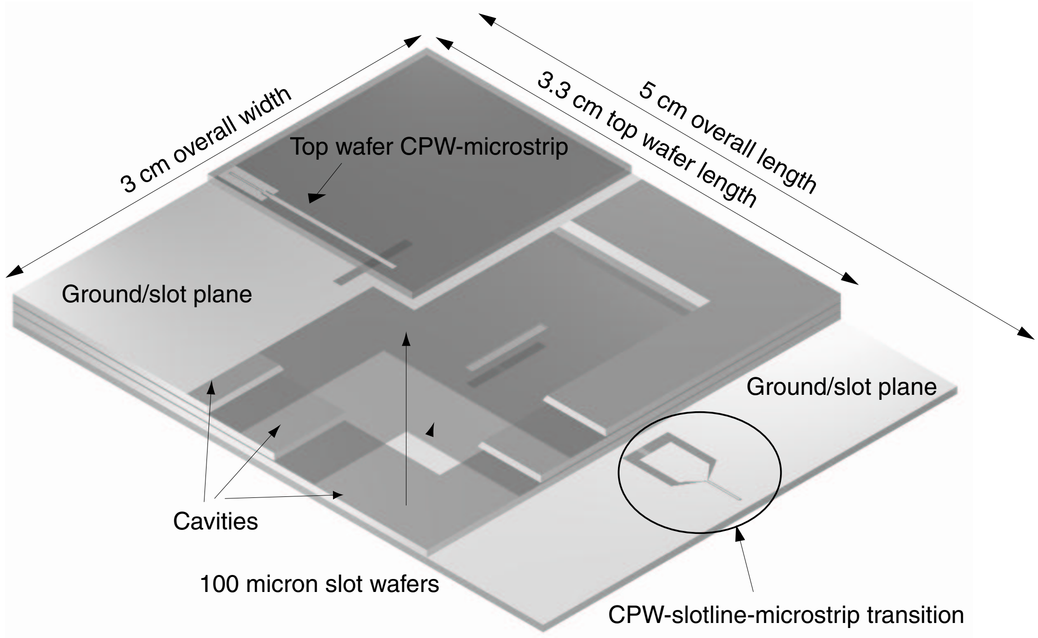

Figure 4.8: Cutaway view of CPW-microstrip fed, slot-coupled three cavity filter. View is to scale.

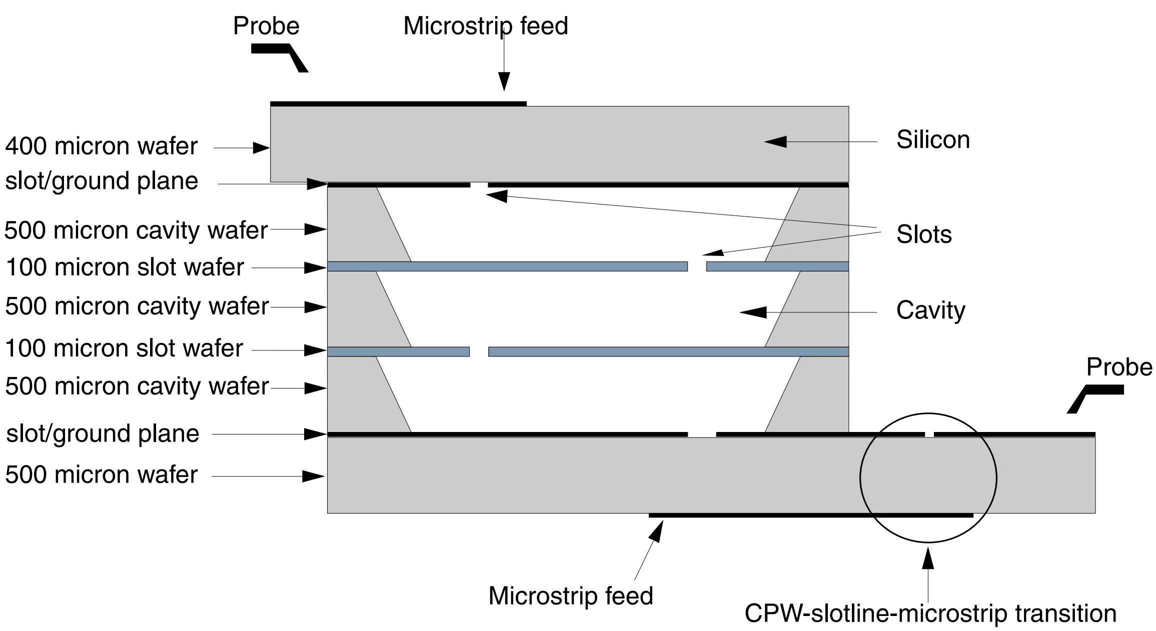

Figure 4.9: Side view of three cavity filter. View is not to scale.

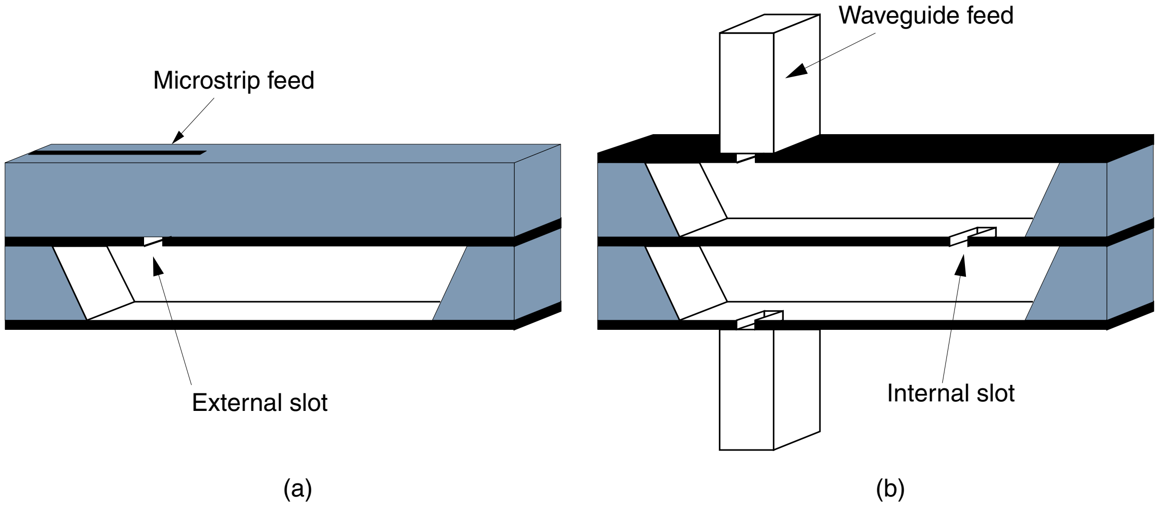

Figure 4.10: HFSS cross-sectional models for: (a) external Q and (b) internal coupling coefficient k.

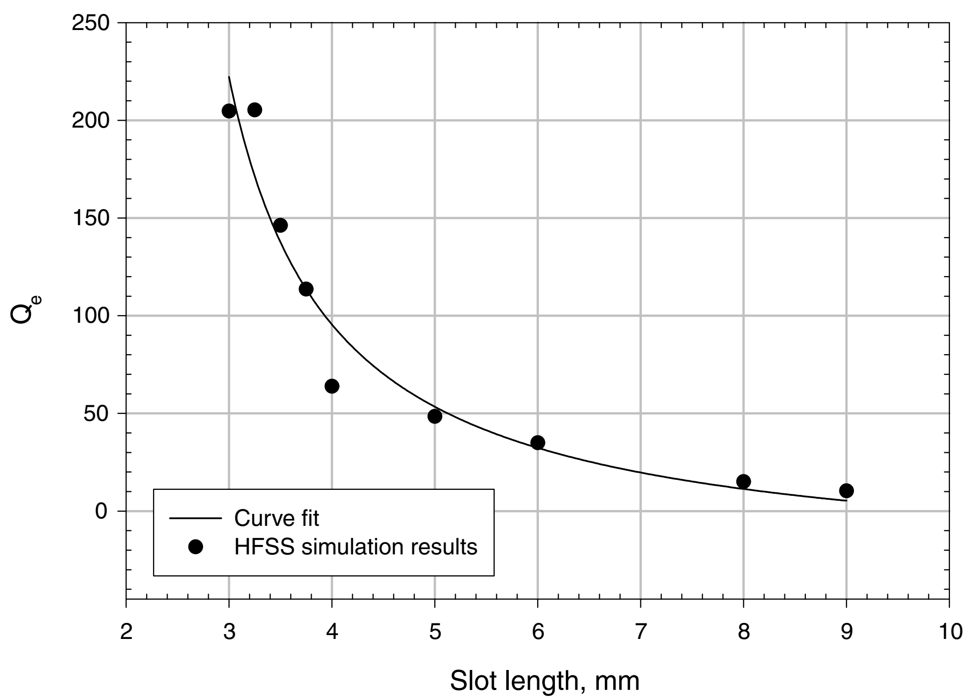

Figure 4.11: External Q versus slot length, curve fit to HFSS simulation results. Slot width held constant at 0.635 mm.

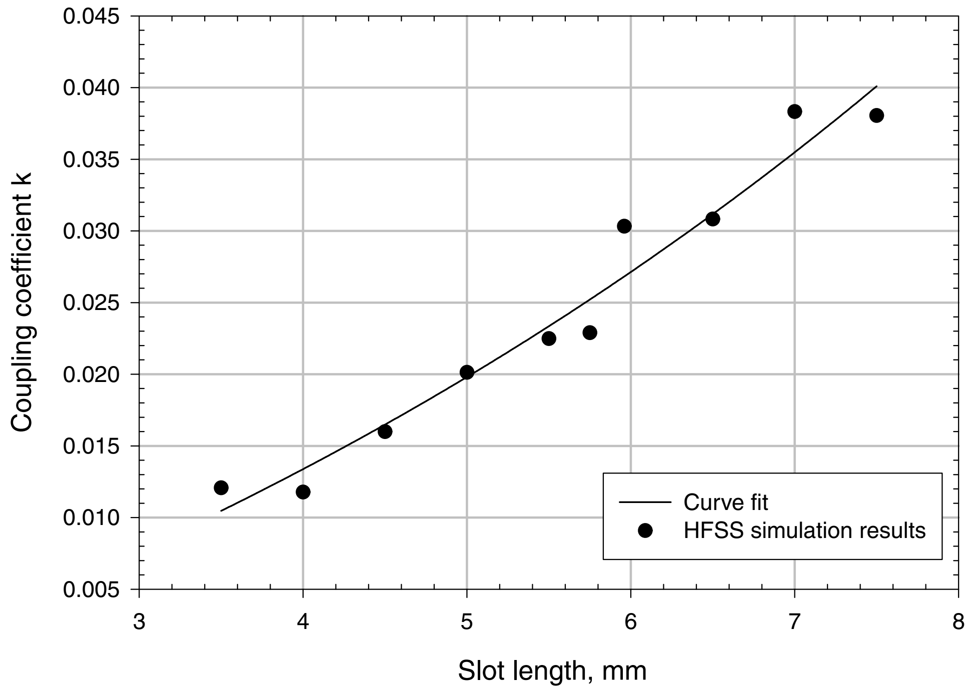

Figure 4.12: Coupling coefficient k versus slot length, curve fit to HFSS simulation results. Slot width held constant at 0.706 mm.

fed simply by waveguides via slots (see HFSS model cross-section in Fig. 4.10b), the relationship between the length of the internal slot and the pole-splitting of the resonance frequency is determined. Waveguide feeding is used for improvement in computation efficiency, without loss of design criticality. The slanted sidewalls are meant to model the sidewall produced by TMAH wet anisotropic etching. Simulations are run for slots of constant width but varying length, and the coupling coefficient k as determined by (4.29) is plotted versus slot length, Fig. 4.12. Nonlinear regression is used to determine a curve fitted to the data, and a slot of 5.921 mm $\times$ 0.706 mm is chosen. Hence, internal coupling as determined by slot length is related to k from (4.29), which is related to the desired prototype k as determined by (4.20).

The 10 GHz resonant frequency of the dominant mode, TE_{101}, dictates the di-

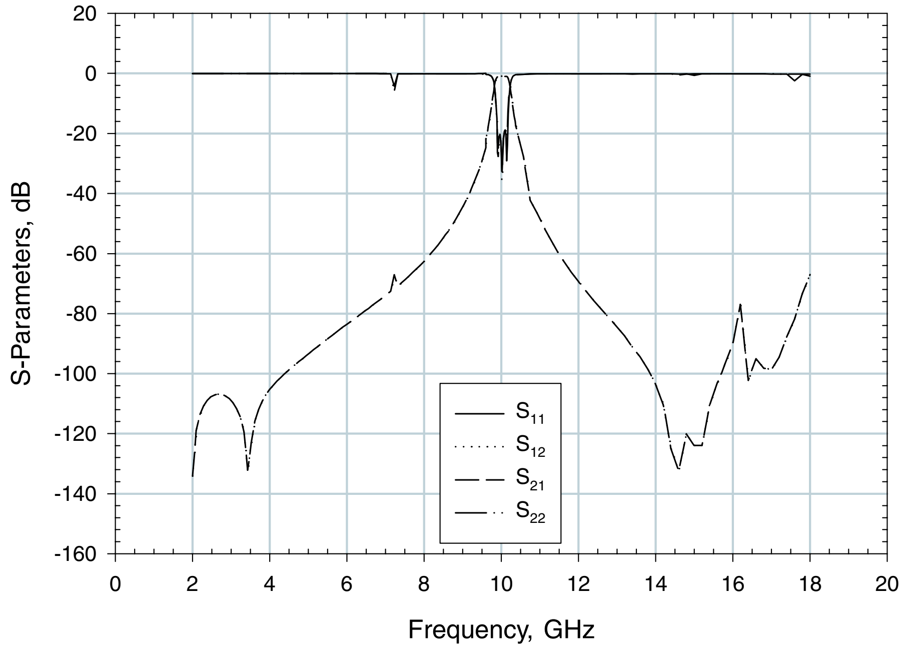

Figure 4.13: HFSS simulation results of three cavity filter.

mensions of the cavity by (3.4),

$$f_{101} = \frac{c}{2\pi\sqrt{\mu_r \epsilon_r}} \sqrt{\left(\frac{\pi}{a}\right)^2 + \left(\frac{\pi}{d}\right)^2} \tag{4.38}$$

For a square cavity, $a = d$, (4.38) reduces to (3.5) and the dimensions of the cavity become 2.12×2.12 cm^2. A square cavity is chosen for maximum possible Q_u as discussed in Chapter 3. In addition, the largest separation between the dominant mode (lowest order) and the next higher order propagation mode occurs for a square-based cavity [57].

With the slot lengths and cavity size determined, the complete filter is modeled in HFSS with the slots placed $\frac{1}{4}$ of the cavity length from the sides and with a microstrip stub length of approximately $\lambda_g/6$ at 10 GHz for maximum coupling to the slot. The simulated results are shown in Fig. 4.13 with a bandwidth of 4% and insertion loss of 0.9 dB at 10.02 GHz.

The HFSS modeled filter is identical to Fig. 4.8 but without a CPW to microstrip transition on either the top or bottom wafer. The model consists of seven silicon wafers. The top wafer is 400 μm thick and has a microstrip feed line on the top side coupled to a slot aperture in the ground plane on the bottom side. This slot feeds a cavity in a 500 μm wafer. A slot in a 100 μm wafer serves as the transition between the top and middle cavities and also between the middle and bottom cavities. The three cavities are identical. The bottom wafer is 500 μm thick with a microstrip on the bottom side and a slot aperture in the ground plane on the top side, coupling to the bottom cavity.

The model has microstrip feed lines on the top surface of the top wafer and on the bottom surface of the bottom wafer. However, the laboratory measuring facility requires that the feed lines for both ports be CPW and on the same side of the circuit. For this reason, it is necessary to design a transition for the bottom microstrip line to a CPW line on the top of the wafer as described in Chapter 2 and as shown in Fig. 4.14 again for convenience. One of these transitions is used on the bottom wafer to transition the feed line as seen incorporated into the final filter design in Fig. 4.8.

4.2.3 Fabrication

The filter was fabricated using high-resistivity silicon wafers with $\epsilon_r = 11.7$. Thermally deposited SiO_2 was used as an etch mask. The micromachined cavities were etched using TMAH wet chemical anisotropic etching. The internal coupling slots were etched using KOH wet chemical anisotropic etching due to its ability to define small, fine features. The microstrip lines, the CPW lines, and the top and bottom wafer ground/slot planes were defined with a titanium/gold/titanium (Ti/Au/Ti) seed layer and gold electroplated to approximately 3 μm (3 to 4 skin depths at 10 GHz). All surfaces of the etched slot and cavity wafers were metallized with a Ti/Au seed layer and gold electroplated to a similar depth. The wafers were all diced to the same size and the edges were aligned to each other manually. The aligned wafer stack

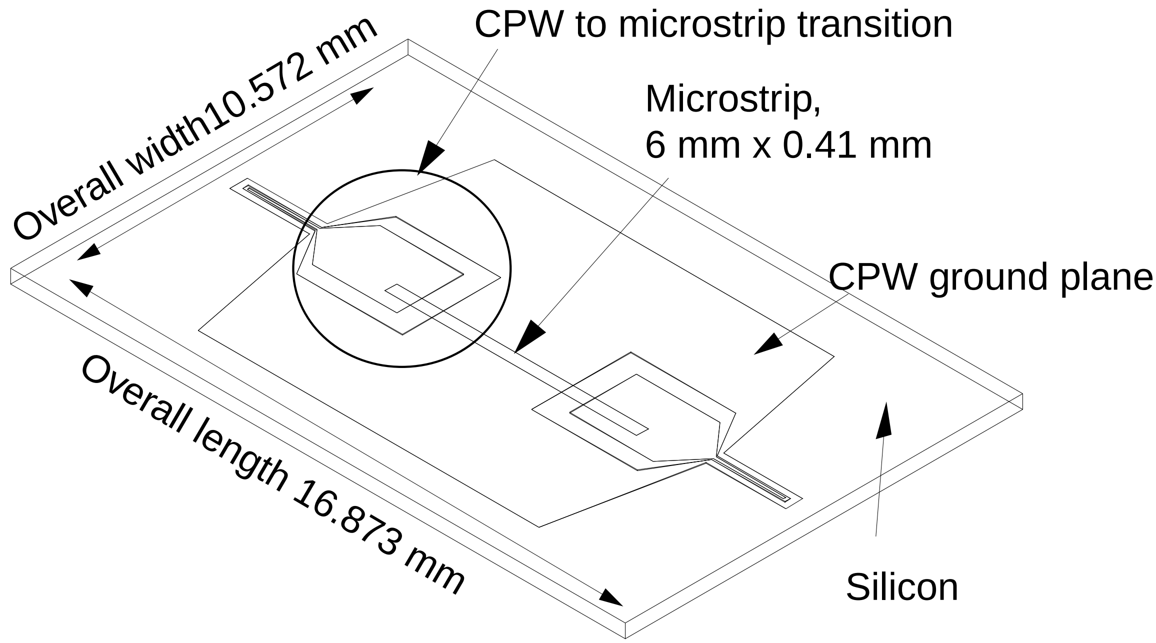

Figure 4.14: CPW to microstrip transition in a back-to-back, through-line configuration. The CPW is on the top of the wafer, the microstrip is on the bottom of the wafer.

was then thermal-compression bonded in the bond chamber of an EV 501 Manual Wafer Bonder at 350° C with 750 N of pressure in a vacuum [68, 69]. The overall dimensions of the finished circuit are approximately 5 cm long $\times$ 3 cm wide $\times$ 2600 μm high as illustrated in Fig. 4.8.

Concerning the choice of seed layer: in IC processing it has been found that many thin films exhibit stress and adhesion problems when deposited onto silicon substrates or silicon dioxide layers. Gold, which is desirable in this work for its nearly oxide-free property and high conductivity, is one of these films. Titanium and chrome have better adhesion, and when used as a barrier film between the gold and the substrate, reduce the gold thin film stresses. Gold exhibits good adhesion to both of these films. Titanium's adhesion characteristic is slightly better than chrome's; however, titanium is attacked by hydrofluoric and buffered hydrofluoric acids, whereas chrome is impervious to them. Therefore, when subsequent processing steps required the use of these acids, chrome was used as the adhesion layer. Otherwise, titanium was primarily the adhesion layer of choice for gold deposition [70, 71].

4.3 Results and Discussion

The finished filter was measured on an HP8510C Network Analyzer using a TRL calibration as described in Chapter 2. The CPW calibration moves the reference planes to the CPW taper transition on both the top and bottom wafers. The overall shape of the filter response compared favorably with the simulated model. The measured losses were found to be higher than expected. These losses are due in part to the CPW-microstrip transition and line lengths. As mentioned in Chapter 2, the transition and line losses are determined from through-lines of various lengths. Also, equipment malfunction during the bonding caused an unexpected rapid rise in temperature, which damaged the gold surfaces and resulted in additional loss. A detailed investigation into the performance of a transmission line with similar heat-induced damage indicated a reduction in the conductivity of the gold. This investigation involved heating a wafer of calibration standards to a temperature at which similar results occurred, then measuring these standards and comparing the loss per unit length to that of a pristine set of calibration standards.

All of these losses were calculated as a function of frequency and de-embedded from the measured insertion loss data. An expanded plot of a comparison of the simulated and de-embedded measured insertion loss results is shown in Fig. 4.15 with a bandwidth of 3.7% and a calibrated, de-embedded insertion loss of 2.0 dB at 10.01 GHz, with reference planes located approximately at the center of the external slots. The measurement repeatability error is on the order of ±0.1 dB. Despite the de-embedding of the feed line loss, the insertion loss of the filter is more than 1 dB higher than the simulated model insertion loss of 0.9 dB. Each of the three cavities has a gold

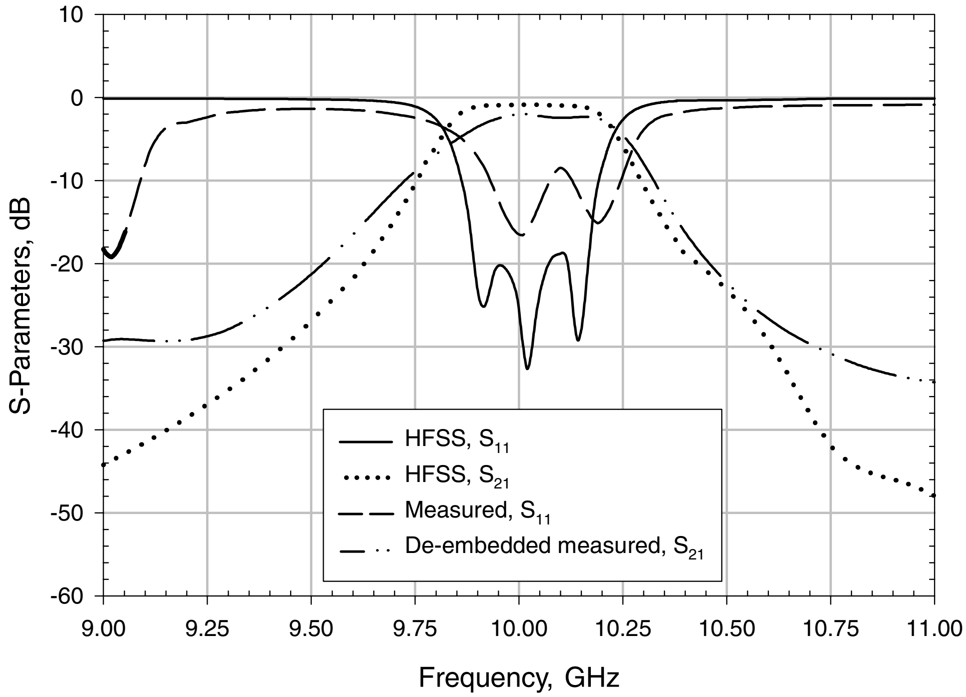

Figure 4.15: Expanded plot from 9-11 GHz comparing simulated and de-embedded measured return and insertion losses.

plated surface area of approximately 9 cm^2. The reduction in conductivity caused by the heat-induced damage of these surfaces likely accounts for this discrepancy. Although it was a simple matter to deduce the line loss by comparing damaged and undamaged calibration standards, it is not possible to extract the precise reduction in cavity wall conductivity from the filter data.

The losses due to the CPW-microstrip transition and the damaged gold were not de-embedded from the measured return loss data. The difference between simulated results and measured data are attributed to these losses.

Figure 4.16 shows the de-embedded measurement of the filter from 2 to 20 GHz. Out of band insertion loss is around 60 dB below and 40 dB above the passband, while the theoretical rejection above the passband was expected to be at least 20 dB lower. The difference between measured and expected values is attributed in part to excitation of spurious surface waves in the substrates as described below, and is in

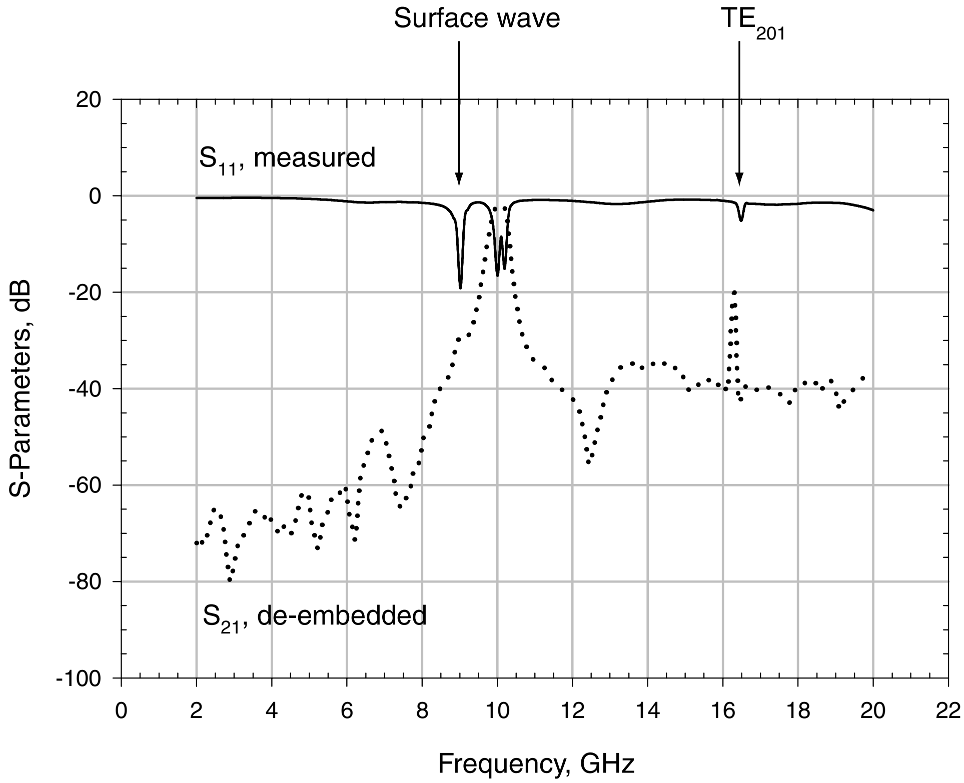

Figure 4.16: De-embedded measurement of three cavity filter. Note the resonances at 9 and 16.5 GHz.

part due to noise in the measurement equipment.

As shown in Fig. 4.16, several resonances are observed in the measured data. To understand these resonances, the transcendental equations for a grounded dielectric slab, representing the top microstrip wafer, were solved [23]. These equations are given by

$$k_c \tan(k_c d) = \epsilon_r h \tag{4.39}$$

$$k_c^2 + h^2 = (\epsilon_r - 1)k_o^2 \tag{4.40}$$

where k_c is the cutoff wavenumber, k_o is the free-space wavenumber, h is thickness of the dielectric and ϵ_r is the relative dielectric constant. The effective dielectric constant ϵ_{eff} was found to be 1.005, which is quite close to free-space. The dominant mode of a non-zero thickness dielectric waveguide is the TM_0 mode with a zero cutoff frequency. At 9 GHz, a TM_0 surface wave has a resonance in the top microstrip wafer, which behaves like a dielectric cavity. The surface wave can be launched from the radiating stub end of the microstrip, refer to Fig. 4.8. Simply changing the wafer dimensions and adding packaging can eliminate or move this resonance to a more convenient frequency. Also seen in Fig 4.16 is a resonance at 16.5 GHz, which is attributed to the TE_{201}, the next higher order cavity mode.

For ease of comparison, the simulated and measured return losses are shown in Fig. 4.17 and the simulated and de-embedded insertion losses are shown in Fig. 4.18.

The Q_u of this filter was not measured in part because the value would not be representative of the filter had the gold not been damaged during processing. Recall that the Q_u relies on the sheet resistance, and hence the conductivity of the metallization. However, the theoretical Q_u for the TE_{101} mode for a filter with air-filled cavities of this size is 565 from (1.3). A single, weakly coupled cavity model in HFSS yields a Q_u of 558 at 10.175 GHz. Earlier work with rectangular cavities has yielded a measured Q_u of 506, compared to a theoretical Q_u of 526 [9,22]. In addition to this work, it has been shown recently in [72] that a micromachined, metallized cavity etched in 1000 μm silicon and weakly coupled yielded a measured Q_u of 890 at 20 GHz, compared to a theoretical value of approximately 1000. All of these results are a demonstration of the ability to achieve experimentally a Q_u very close to the theoretically calculated Q_u in micromachined silicon cavities, using the appropriate conductivity value.

4.3.1 Issues

With this filter fabrication, accurate alignment and quality bonding were important issues. All wafers were diced to the same size and the edges were aligned manually. The misalignment with this method has not been measured, but it is probably on the order of several hundred microns. The filters presented in the following

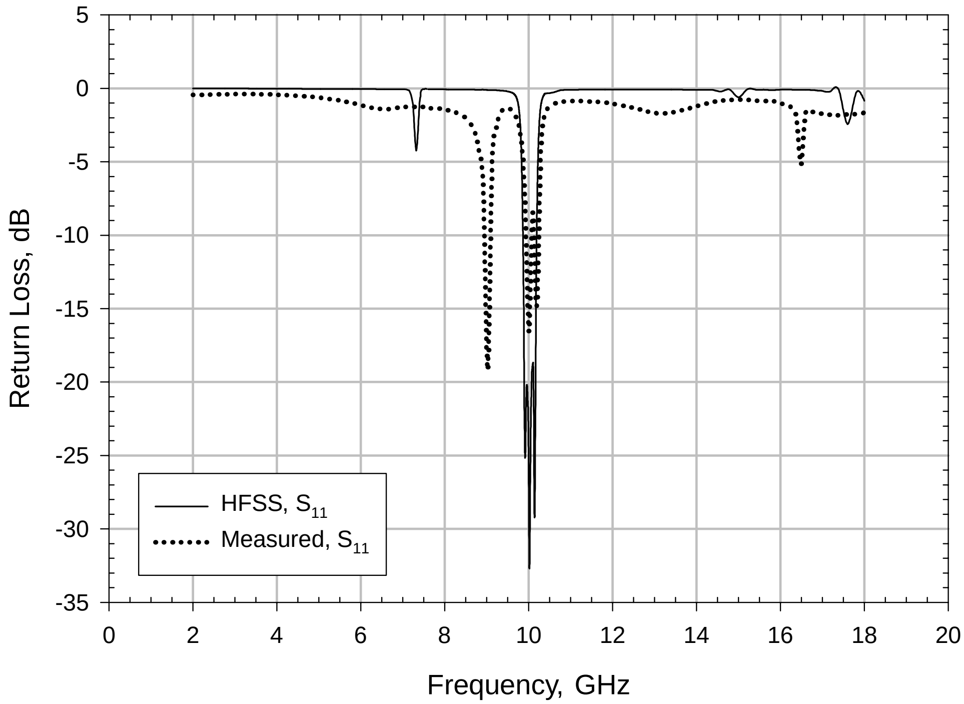

Figure 4.17: Simulated and measured return loss.

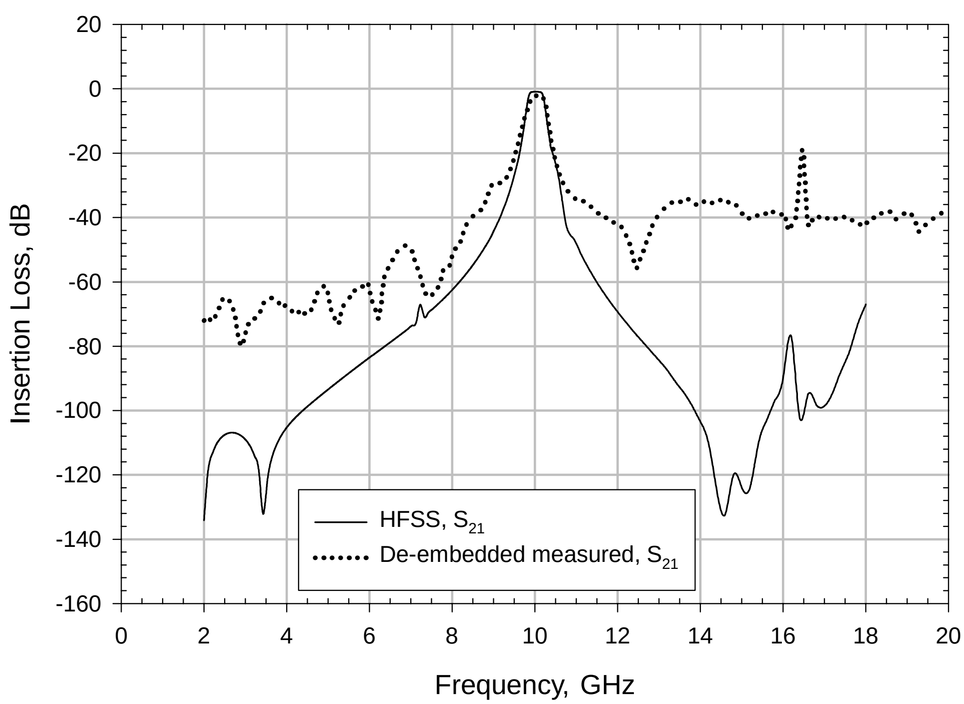

Figure 4.18: Simulated and measured insertion loss.

chapters are designed for 32 GHz and 28 GHz, where precise alignment of the wafers will be even more critical than at 10 GHz. A more exact method of aligning will be needed. Several bonds had been performed using the EV Thermal Compression Bonder in the SSEL laboratory. A three-wafer bond was manually forced apart, and the gold metallization pulled away from the silicon wafer in a few places. Care must be taken in monitoring the conditions used with the bonder in order to ensure a quality bond and good metal conductivity.

4.4 Summary

A simple and complete filter synthesis method for direct-coupled microwave cavity filters has been derived and implemented. It is based on well-established network methods and utilizes readily available parameter tables.

A multiple-pole, micromachined, vertically integrated bandpass filter has been successfully demonstrated for the first time. It is lightweight, of compact size, and may be easily integrated into a monolithic circuit. Loss is introduced because measurement of the circuit requires complex feed structures and the gold surfaces suffered a loss of conductivity during fabrication. In spite of these issues, the measured results show a filter response that is otherwise in very good agreement with the simulated model.

The flexibility of this method is now demonstrated in the design and fabrication of a horizontally coupled cavity Chebyshev filter, which is presented in the next chapter.

CHAPTER 5

A Horizontally Integrated Micromachined Cavity Filter

Imagination is more important than knowledge.
Albert Einstein

5.1 Introduction

A 32 GHz filter constructed of evanescent waveguide-coupled micromachined cavities in silicon is presented in this chapter. The structure of the filter consists of a microstrip feed via slot apertures to two side-by-side, horizontally integrated cavities, which are coupled in turn by evanescent waveguide sections. The measured results are presented and compared to an HFSS model. The simulated model has a bandwidth of 2.3% centered at 31.74 GHz with an insertion loss of 1.2 dB at that frequency. The measured filter yields a 2.2% bandwidth centered at 31.70 GHz with a de-embedded insertion loss of 1.6 dB at that frequency.

An alternative filter design that incorporates the horizontal integration of the micromachined cavity resonator is proposed, see Figs. 5.1 and 5.2. This design is after the fashion of full-height rectangular waveguide filters as presented in [73]. The cavities are placed horizontally in a single wafer, side by side, and are coupled together

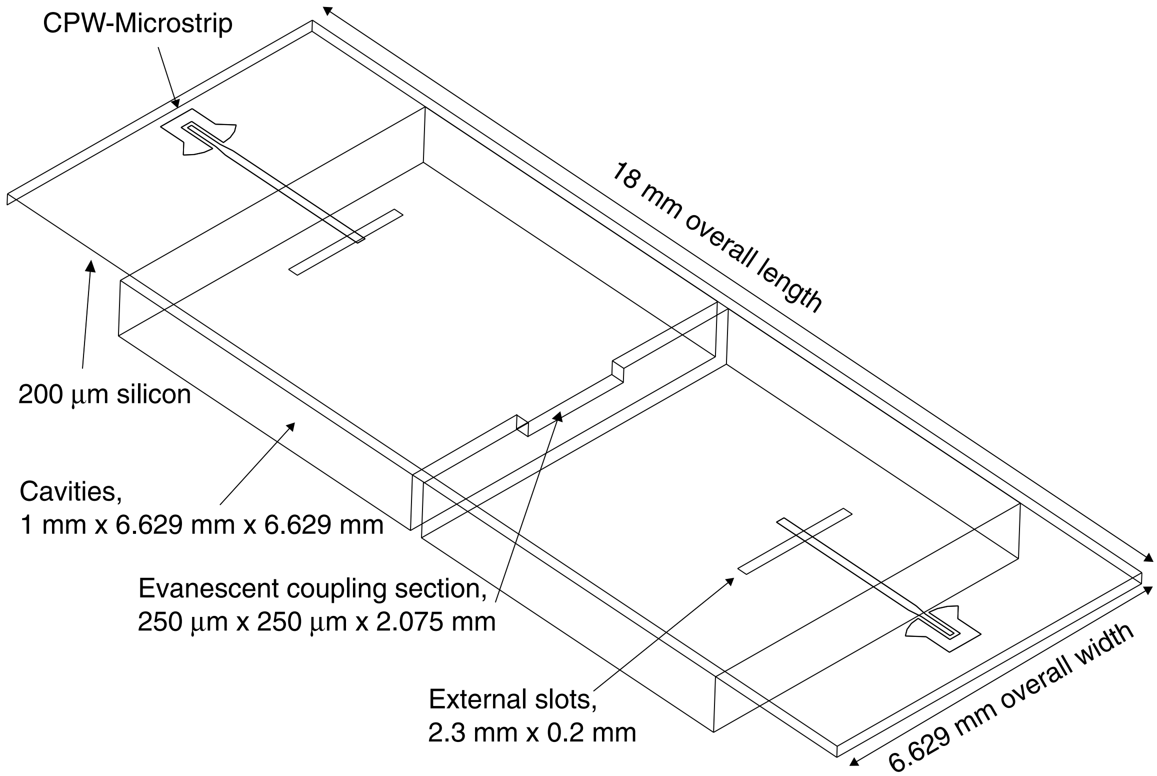

Figure 5.1: Horizontally integrated 2-pole Chebyshev filter. View is to scale.

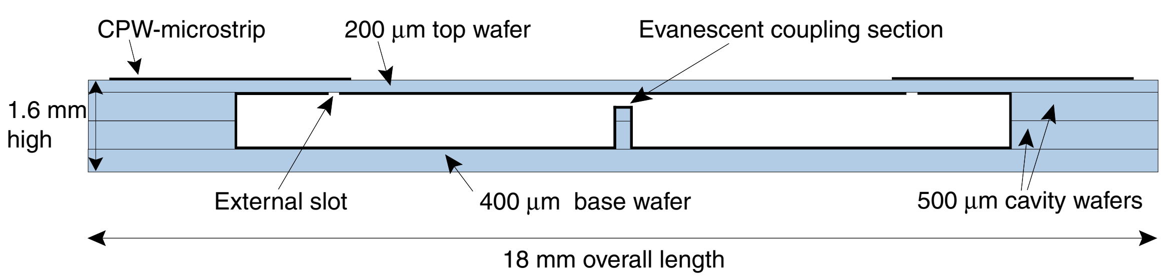

Figure 5.2: Sideview of horizontally-oriented filter. View is not to scale.

through evanescent sections in their common side wall. This will eliminate the need for the 100 μm internal coupling slot wafers between the cavities. The entire wafer "stack" will be shorter as a result of the horizontal integration. Using two 500 μm wafers will double the cavity volume, which will increase the Q_u as compared to the vertical design. Even with this increase in cavity volume, the overall height of the structure will be reduced. Because the cavities are situated side by side, the feeding microstrip lines will be on the same side of the same wafer, eliminating the need for a top-to-bottom transition as in the previous work and simplifying the measurement. This design will be performed at 32 GHz, which will require reducing the length and width of the cavities. It will be possible to fabricate multiple copies of the circuit on the same wafer, whereas at 10 GHz, the size of the cavity was the limiting factor, and only one cavity would fit in the space of a single wafer piece. The cavities can be laid out in a way that will allow for cross-coupling between electrically non-adjacent resonators, which can be made to produce either an elliptic or a linear phase response.

The possibilities of designing both dual-mode and cross-coupled filters were investigated. What is frequently referred to as a dual-mode cavity filter in the literature, [73, 74] for example, is one that employs coupling screws or corner cuts in the cavity that couple together the two degenerate modes, such as TE_{101} and TE_{011}, yielding two poles from just one resonator. These dual-modes are then coupled from cavity to cavity, producing additional cross-coupling effects. The modes require that the height of the cavity equal the width of the cavity, so that a half-wavelength of the same length in both the width and height directions may be formed. For the reduced-height waveguide design in silicon, this dual-mode design is not possible, because height and width cannot be the same. At 32 GHz, the cavities will be approximately 6.6 mm square. A height of 6.6 mm can be achieved only if many wafers are stacked together, defeating the intent of reduced height. However, it is still possible to produce an elliptic or linear phase response by cross-coupling between single-moded, non-adjacent resonators. This investigation is intended to prove this flexibility in the filter design, allowing for future designs other than the standard Chebyshev.

5.2 Design and Simulation

To improve Q_u, the cavities were to be fabricated out of two 500 μm silicon wafers which are stacked, so that the cavity height total is 1 mm. This effectively doubles the volume of the cavity compared to the previous work. Initially, the coupling sections were oriented so that their cross-section was varying in width but the height was held constant and equal to the full 1 mm height of the cavity, see Fig. 5.3a. The coupling section dimensions of length, height and width are given in the figure. Then the orientation was changed so that the cross-section was narrow in height, varying from 0.25 mm to 0.5 mm, and centered on the cavity sidewall, see Fig. 5.3b. With this configuration, half the coupling section is in the top wafer and half is in the bottom wafer. This creates a slot opening that is parallel to the magnetic field in the cavity, oriented just as the coupling slots were in the previous work. For ease of fabrication, the decision was then made to move the coupling section to the top of the cavity wall, so that the entire coupling section resides in the top wafer only, see Fig. 5.3c. This final design was incorporated into the model and eventually fabricated.

The design is again accomplished with the aid of HFSS. A 2-pole Chebyshev filter with a 0.1 dB ripple and a 1.25% bandwidth is chosen as a demonstration vehicle for the proposed concept. The design is performed in the same way as that described in the previous chapter. The Q_e is calculated using (4.24) and (4.25) and is modeled using a single cavity and a microstrip-fed slot. The modeled Q_e is determined from the phase of S_{11} and (4.36). The Q_e versus slot length is plotted in Fig. 5.4. Nonlinear regression is used to determine a curve fit to the data. The coupling coefficient is calculated using (4.20) and is modeled using two cavities coupled by an evanescent

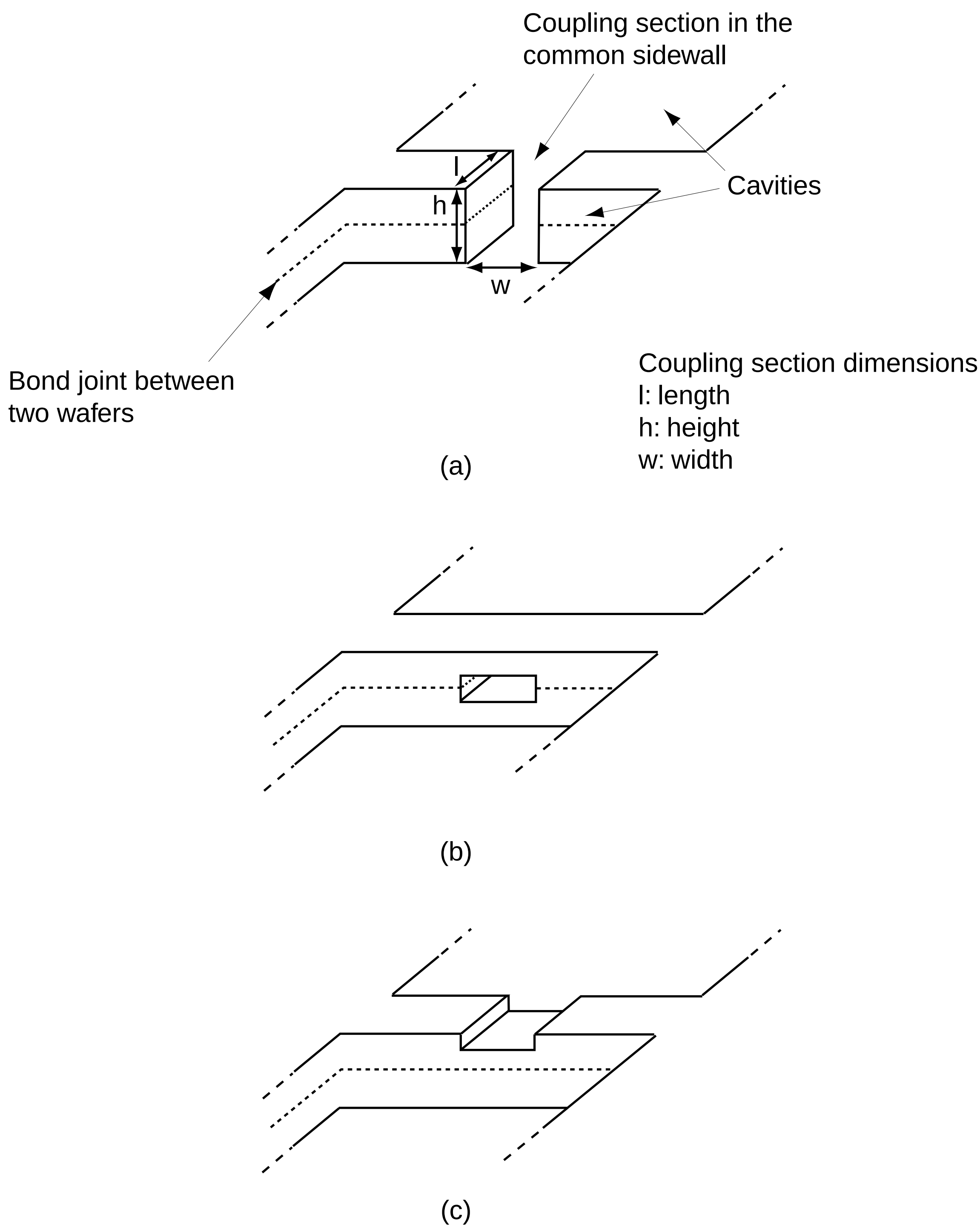

Figure 5.3: Various coupling section designs and their orientations.

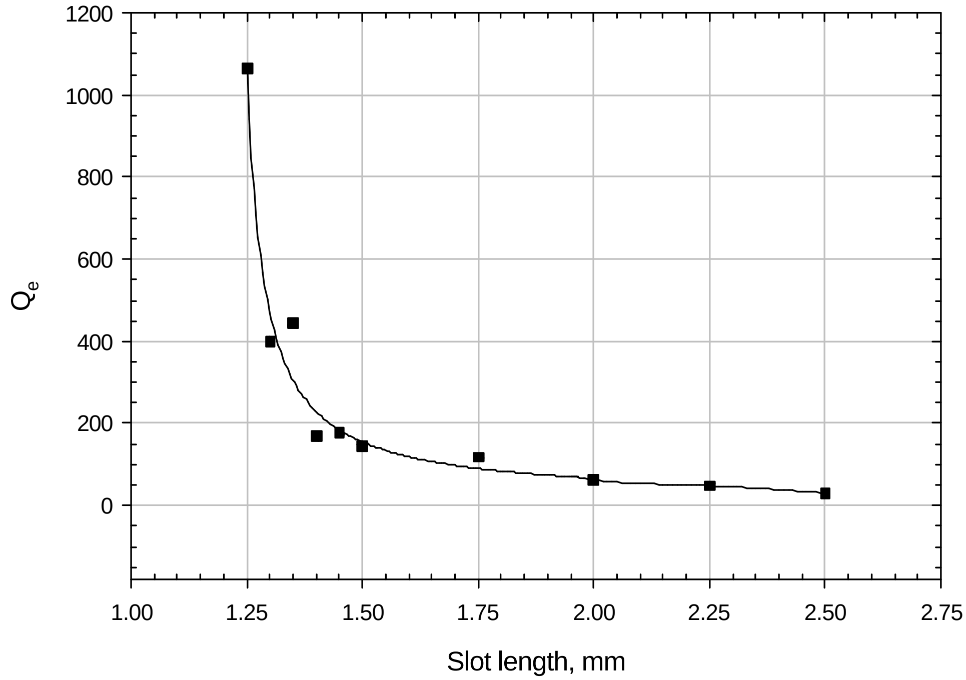

Figure 5.4: External Q vs. slot length, curve fit to HFSS simulation results. Slot width held constant.

section situated in their common sidewall, see HFSS model cross-section in Fig. 5.5. The modeled k is determined from (4.29). The vertical sidewalls are meant to model the vertical sidewalls produced by the Deep Reactive Ion Etching system. Both slanted and vertical sidewalls in the coupling section were tried initially in the HFSS design model. Vertical coupling section sidewalls gave better results in HFSS than the slanted sidewalls as would be produced by wet chemical etching, and therefore the decision was made to use the RIE system to produce more vertical sidewalls in both the cavities and the coupling sections.

As mentioned above, various orientations of the coupling section were modeled. Comparison of the coupling coefficient k for various coupling heights, lengths and widths is shown in Fig. 5.6. Two of the data sets are for a full cavity-height coupling section (Fig. 5.3a), two are for the coupling section located halfway up the cavity wall (Fig 5.3b), and one is for the coupling section located at the top of the cavity wall

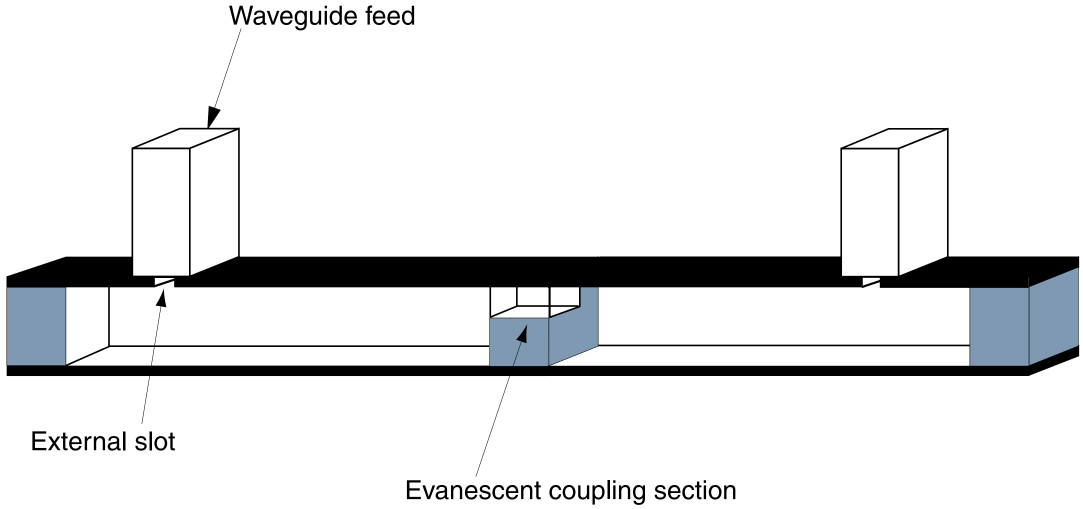

Figure 5.5: Cross-sectional sideview of HFSS model for modeling of coupling coefficient k.

(Fig. 5.3c). The graph shows that as one transverse dimension is decreased, the other dimension must increase for a given value of k. Also, if the length of the coupling section is increased, the coupling decreases. The solid square data points are for a coupling section situated at the top of the cavity wall and with 0.25 mm height and 0.25 mm length dimensions. The open circles are for the same height and length dimensions but for a coupling section situated half way up the cavity wall. The two data sets are close together, but for a given k, a coupling section at the top of the cavity wall requires a slightly wider opening, and hence stronger coupling, than for a coupling section half way up the wall. This is reasonable, as the magnetic field and surface currents are essentially the same at the top and middle of the cavity wall.

After fine-tuning the HFSS models, the external coupling slot dimensions are 2.3 mm $\times$ 0.2 mm. The coupling section dimensions are 2.23 mm wide $\times$ 0.250 mm high $\times$ 0.250 mm long (where length is also the separation between the cavities). The dimension of the cavities is 6.629 mm square, and they are identical. The microstrip feed lines are 165 μm wide for a 50 Ω line on 200 μm silicon at 32 GHz, and the microstrip stub length extends 343 μm beyond the external slot center. The HFSS

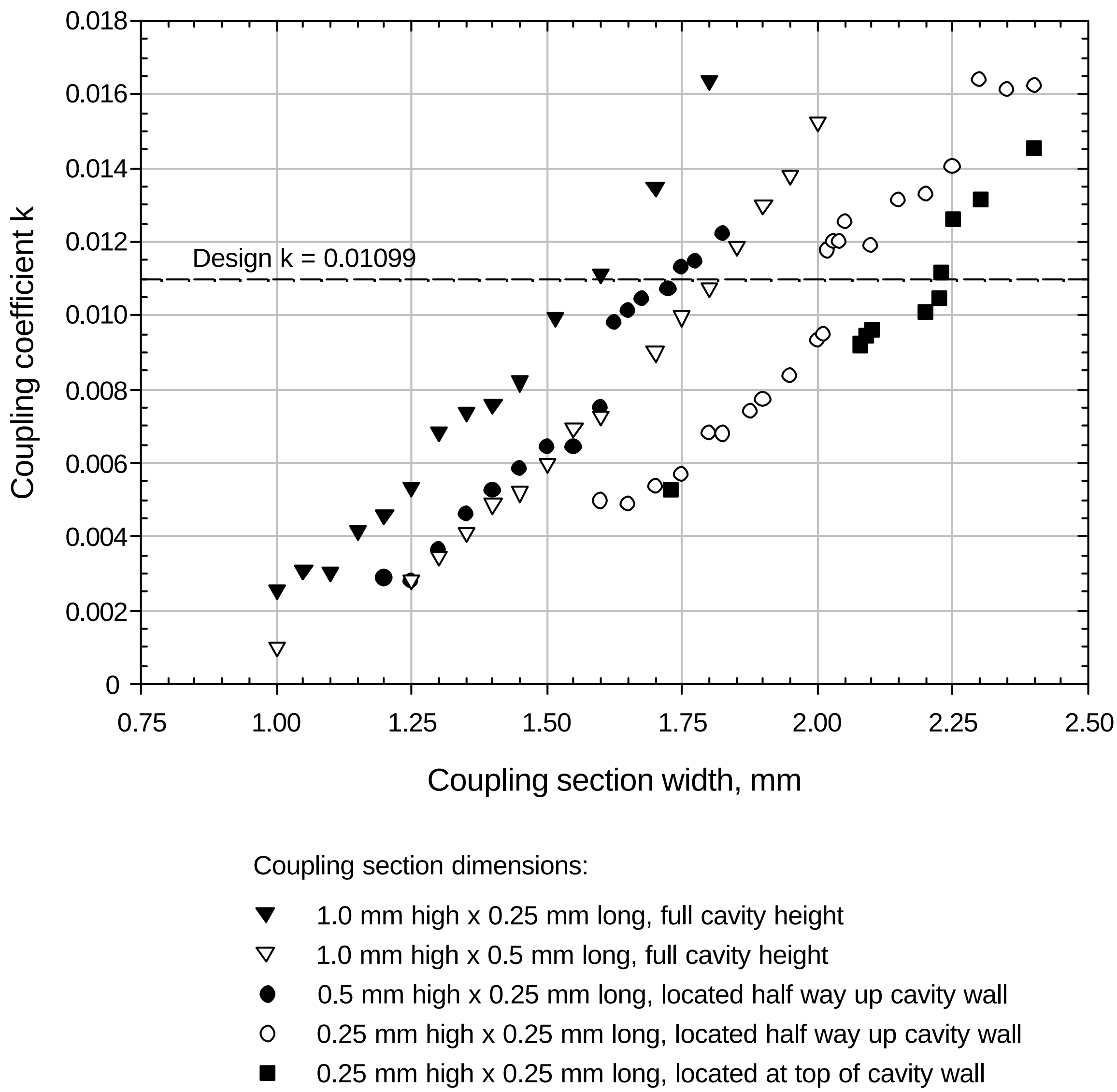

Figure 5.6: Various k vs. coupling section dimension data sets.

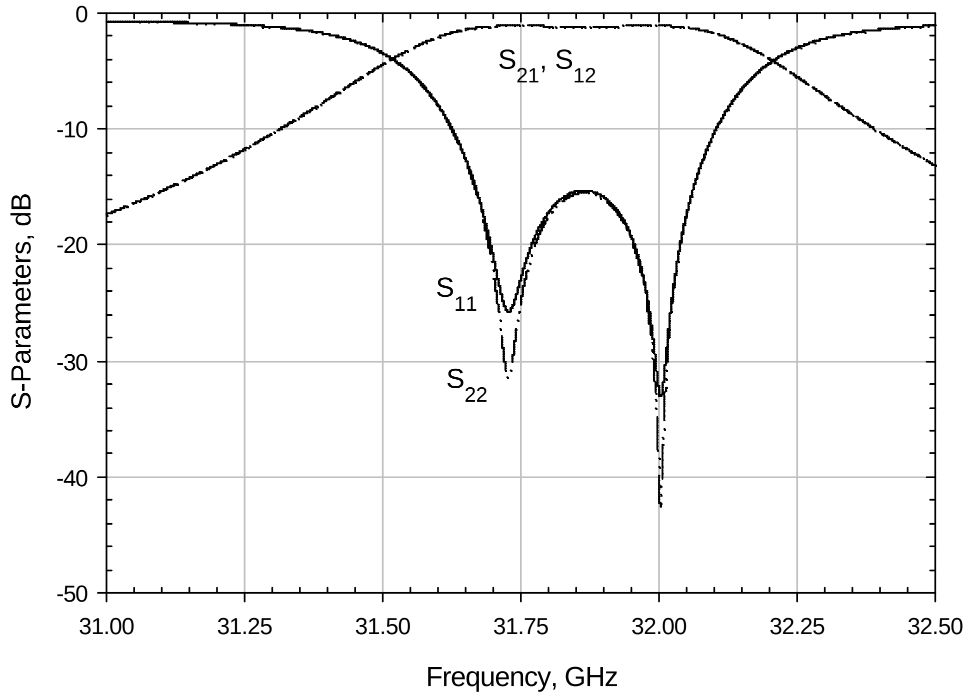

Figure 5.7: HFSS simulated results for complete horizontal 2-pole Chebyshev filter.

model response is shown in Fig 5.7.

A via-less CPW-microstrip transition was used in the design as described in Chapter 2 and as shown with dimensions in a back-to-back through-line configuration in Fig. 5.8. The IE3D response for this design with a microstrip length of 3 mm was given in Chapter 2 in Fig. 2.11. The S-parameters for this design with a short microstrip length of 926 μm is shown in Fig. 5.9. The modeled insertion loss for this back-to-back configuration is 0.2 dB at 32 GHz. This transition was not included in the completed HFSS model.

The finished design consists of 4 silicon wafers. The top wafer is a 200 μm wafer with the CPW-microstrip transition and microstrip feed lines coupled to slots in the microstrip ground plane. The middle wafers are each 500 μm wafers etched through to form the cavities and partially etched to form the coupling section. The bottom wafer provides the bottom wall to the cavities. The alignment of the multiple wafer stack in this work was achieved with the aid of 596 μm glass microspheres [75]. Shallow

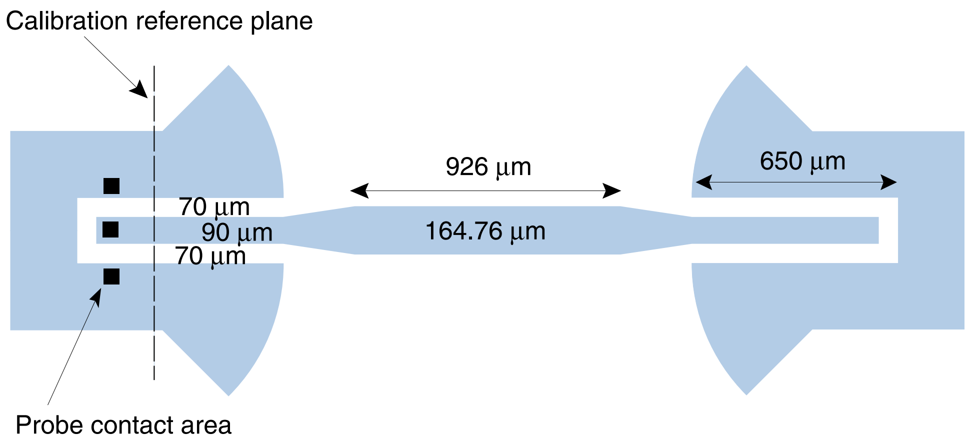

Figure 5.8: Via-less back-to-back CPW to microstrip transition with dimensions for fabrication on 200 μm substrate.

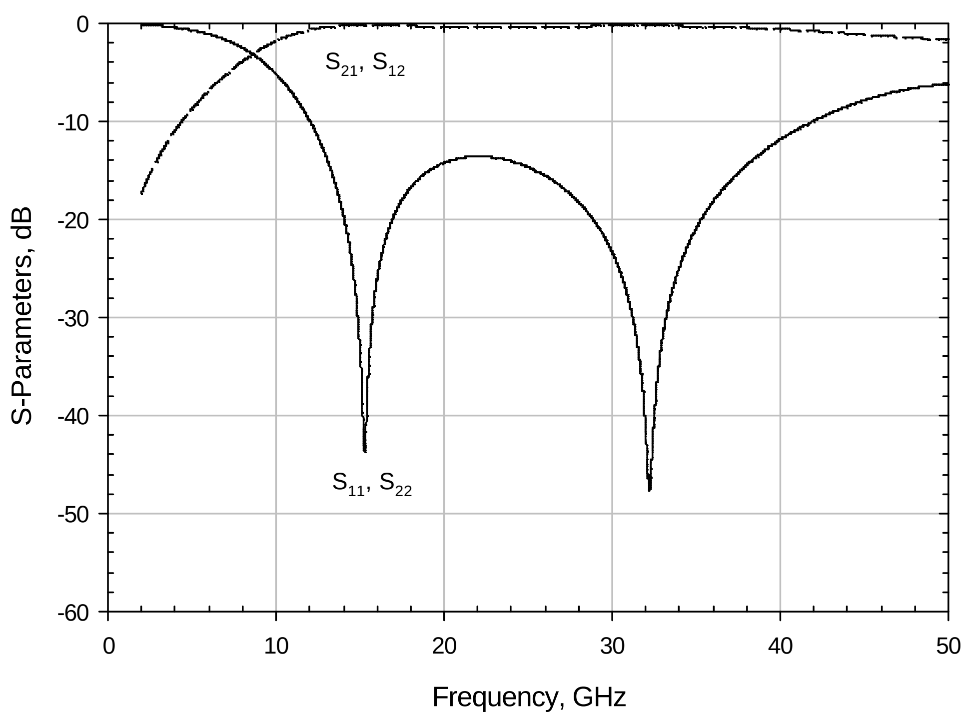

Figure 5.9: IE3D results for CPW to microstrip transition shown in Fig. 5.8.

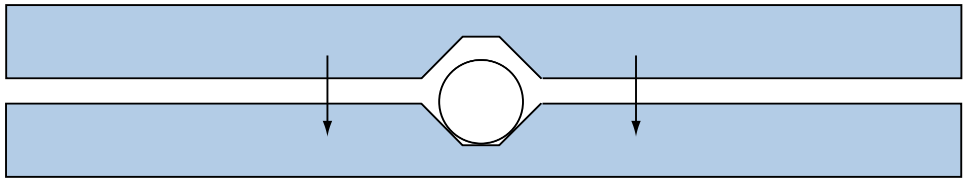

Figure 5.10: Alignment scheme using glass microspheres placed in TMAH-etched pyramidal cavities.

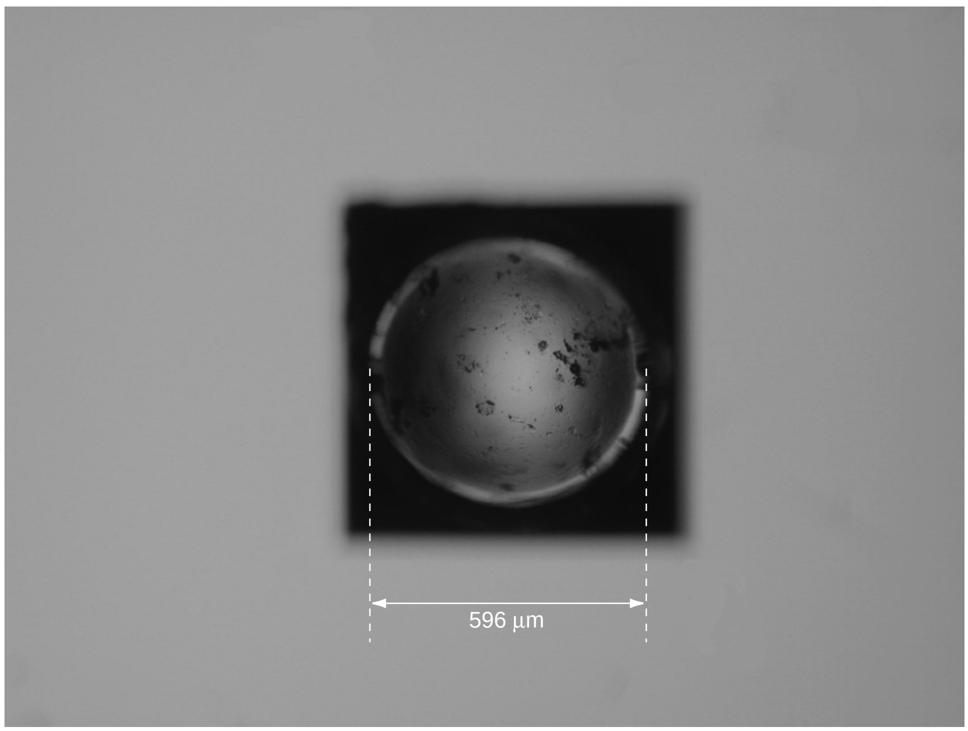

Figure 5.11: Glass microsphere shown resting in TMAH-etched cavity.

pyramidal cavities were etched in each wafer using TMAH to accommodate one-half of a glass sphere's volume. A cross-sectional schematic of two etched wafers brought together with a glass sphere for aligning is shown in Fig. 5.10. Several alignment cavities were patterned at various places on the wafer, to assure accurate alignment in each direction. Various cavity sizes were patterned to accommodate the $\pm 6\mu$m variation in the sphere diameter, any possible over- or under-etch, or inconsistent etch between cavities. In this manner, the top 3 wafers were aligned to each other. A micrograph of a glass sphere placed in an alignment cavity is shown in Fig 5.11.

5.3 Fabrication

5.3.1 Reactive Ion Etcher Characterization

Before fabrication on the filter could begin, it was necessary to characterize the STS Reactive Ion Etcher system (RIE) for this design. The first approach to etching the cavities and the coupling section was to pattern with photoresist and etch the cavities from the front side of the wafer first, then pattern the coupling section for etching, also from the front side. Recall that the photoresist functions as the etch mask during the RIE etch. Photoresist is typically applied to the wafer by the spinning technique, and the most uniform photoresist thickness and coverage are achieved if the wafer is smooth and uniplanar. Adequate resist thickness and coverage is necessary if the resist is to perform as an etch mask, and for accurate lithographic patterning of features. As the photoresist for patterning the coupling section was spun over the etched cavities, there was some thinning of the resist along the cavity edges. This thinned resist can eventually wear away in the RIE and will allow etching of the cavity edges. After etching, the cavity edges appeared rough and chipped as if they had suffered additional etching during the etch of the coupling section.

An SEM scan revealed other problems with the deep RIE etch. Recall that the time-multiplexed RIE etch is performed in two steps, several seconds of etch followed by several seconds of passivation. This passivation step leaves a layer of material on the etched sidewalls. The layer is seen peeling away from the etched sidewalls in Fig 5.12. Repeated ashings in an O_2 atmosphere in the plasma asher vacuum chamber [76] removed most of the peeling passivation layer, as seen upon inspection with the light microscope and in subsequent SEM scans. Removal of the passivation layer, especially if it is peeling away, is necessary for optimal metal adhesion to the cavity walls.

Additionally, the passivation layer remaining from the first etch prevented the

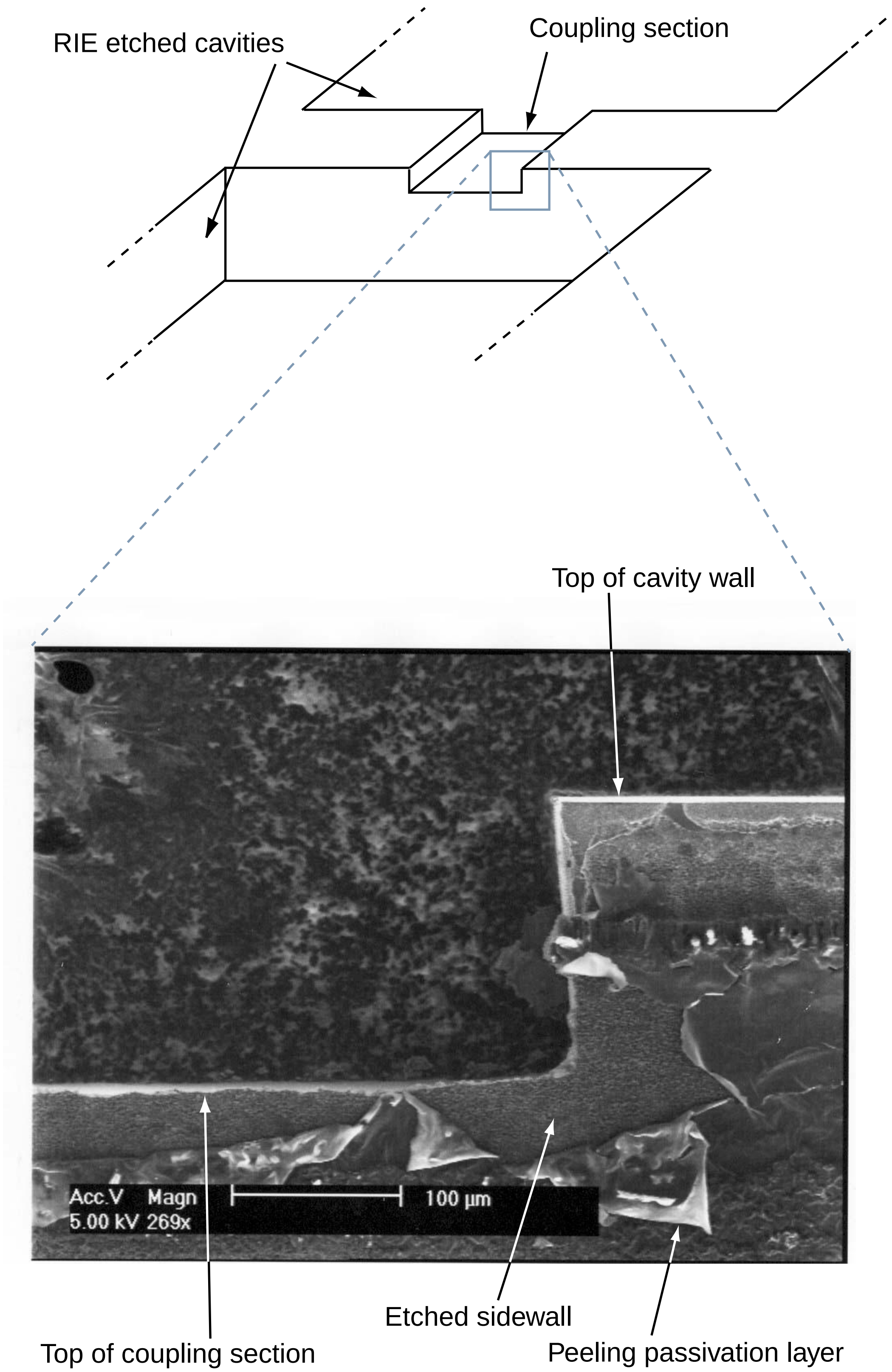

Figure 5.12: SEM image of etched sidewall showing peeling passivation layer.

etching of the edges of the coupling section, see the SEM image in Fig. 5.13. The images show the two cavities and the "beam" of silicon separating them, with the coupling section partially etched into the top of the beam. (The grid visible in the background is part of the SEM apparatus.) The hold over passivation layer protects the section of the cavity wall that meets the coupling section. Eventually, it is worn down and etched, leaving a thin layer of silicon "grass" perpendicular to the coupling section surface just at the edges of the coupling section. A similar effect is also visible in other photos along the very top edges of the cavities; there is a very rough and uneven quality to the very top of the cavity sidewalls after the second etch.

The solution to these problems was to redesign the masks for an etch of the coupling section from the topside of the wafer, followed by an ashing in the O_2 plasma to remove the passivation layer. Then the cavity etch photoresist mask would be patterned from the backside of the wafer. By etching the coupling section through the front side of the wafer first, then turning the wafer over for the application of resist to the un-etched back side for the full wafer cavity etch, the etch mask lithography steps are optimized. For each etch, the sample wafer is mounted onto a full 4 inch carrier wafer using photoresist as the adhesive, so that all patterns on the underside are protected from the etching action of the RIE. In this way the passivation layer is removed and the resist is spun over a flat surface, eliminating both the passivation layer interference and the step coverage problem.

With this solution in hand, the cavities and coupling sections were etched successfully and evaluated using the SEM. The quality of the etch was good with clean and relatively smooth sidewalls. The problems involving the passivation layer were resolved. Figure 5.14 shows the coupling section and the sidewall. By etching the coupling section from the top of the wafer and the cavities from the back, the "grass" effect as seen along the sidewall edges was eliminated. Neither the scalloping of the sidewalls nor the vertical striations at the wafer surface edges were problematic for

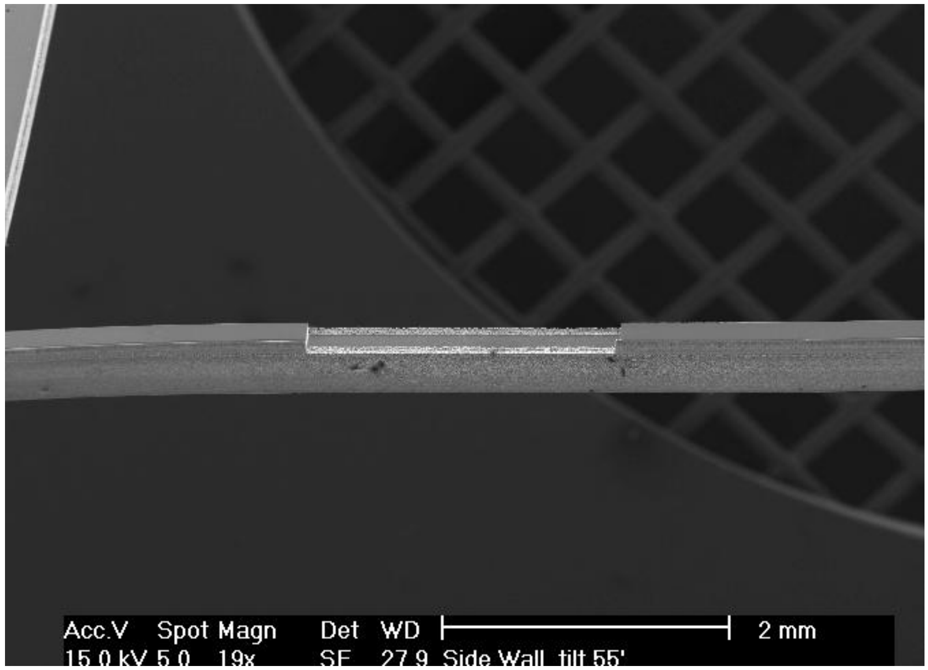

(a)

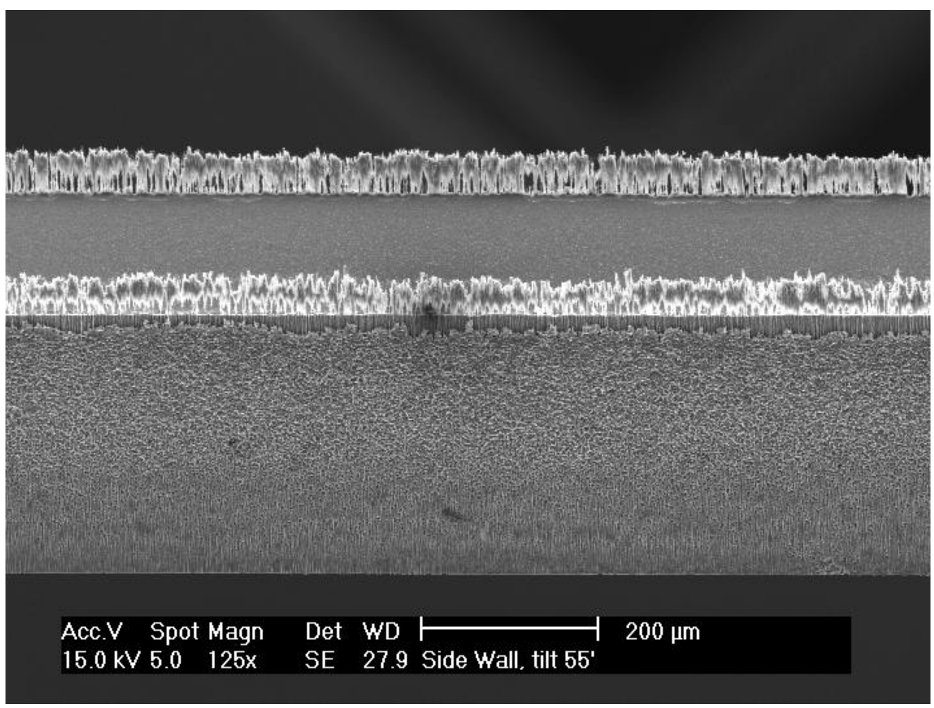

(b)

Figure 5.13: SEM images: (a) “Beam” of silicon separating two cavities, coupling section etched into the beam. (b) Close-up of coupling section showing “grass” effect.

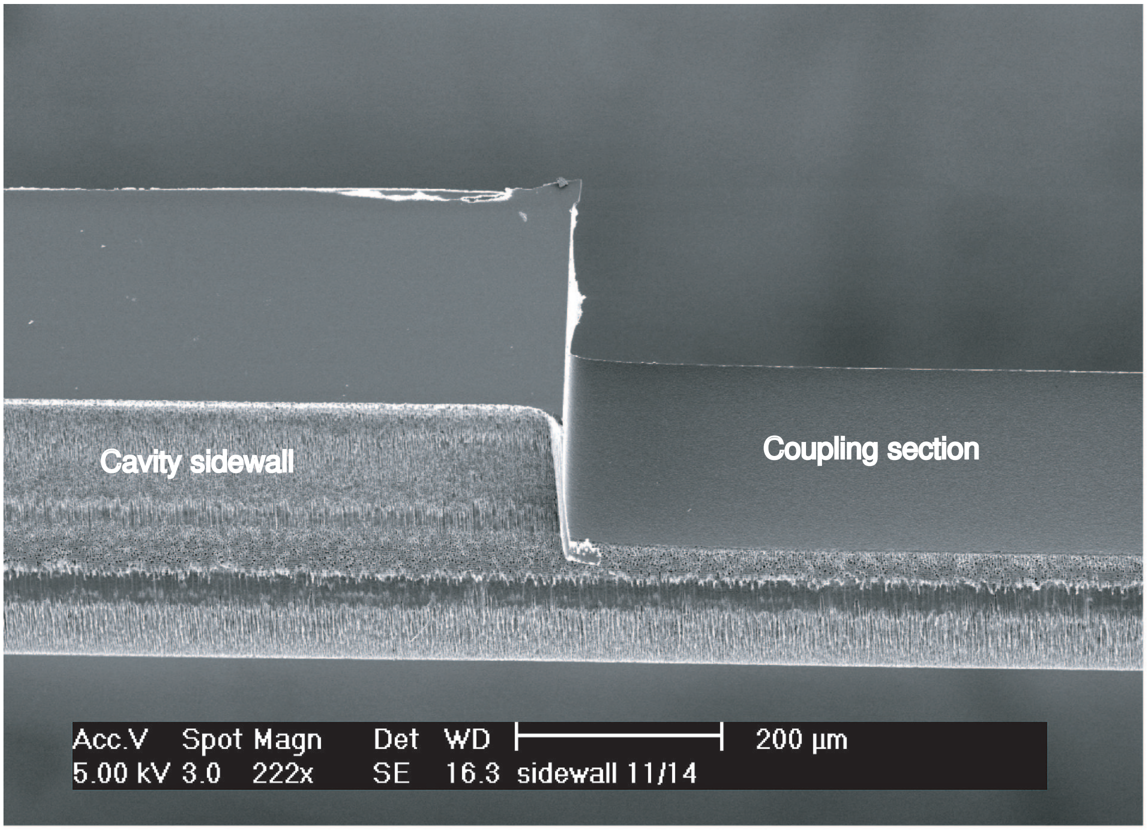

Figure 5.14: SEM image showing good quality sidewalls after etching coupling section from top side of wafer and cavities from back side of wafer.

metallization.

5.3.2 Complete Filter Fabrication

The filter is fabricated using high-resistivity silicon wafers with $\epsilon_r = 11.7$. Thermally deposited SiO_2 is used as an etch mask on all wafers for TMAH etching of the small alignment cavities. The SiO_2 is then removed. The top wafer CPW-microstrip lines are patterned with an evaporated chrome/gold (Cr/Au) seed layer and are then gold electroplated to approximately 2-4 μm (+4.5 skin depths at 32 GHz). The top wafer slot is defined in Cr/Au using a standard lift-off process, followed by gold electroplating to approximately 2-4 μm.

Two 500 μm wafers are used to create the 1 mm high micromachined cavities. The cavities and evanescent coupling section are etched using the STS Reactive Ion Etcher system in two steps as described above. The coupling section is etched from the front side of the top cavity wafer. Then, the cavities are etched completely through the top cavity wafer from the back side. Finally, the cavities are completely etched through the bottom cavity wafer from the front side. When brought together, the two wafers form 1 mm high resonant cavities coupled together by an evanescent coupling section at the top of the sidewall connecting the two cavities.

All surfaces of the etched cavity and coupling section wafers are sputter or evaporator coated with a Ti/Au seed layer, followed by gold electroplating to 2-4μm. A 400 μm wafer, gold electroplated to 2-4 μm, serves as the bottom of the cavities. The wafers are aligned using the glass microspheres and gold-to-gold, thermal-compression bonded in the vacuum bond chamber of the EV 501 Manual Wafer Bonder at 350° C with 750 N of pressure in a vacuum [68, 69]. The overall dimensions of the finished circuit are approximately 18 mm long $\times$ 6.629 mm wide $\times$ 1.6 mm high as illustrated in Figs. 5.1 and 5.2.

5.4 Results and Discussion

5.4.1 Alignment and Bonding Evaluation

For inspection and evaluation purposes, an SEM image was taken of the cavity corner after gold plating and the thermal compression bond of the cavity and bottom wafers only, shown in Fig. 5.15. All surfaces are gold plated in the image. The bond joint is indicated in the figure. Alignment and bond both appear to be very good. The “bubbles” seen in the image occur just on the etched sidewalls of the cavities, and may be due to outgassing during the bond procedure of either absorbed solvents from previous processing steps or any remaining passivation layer. Although this factor did not seem to affect the filter’s performance, as will be discussed shortly, future

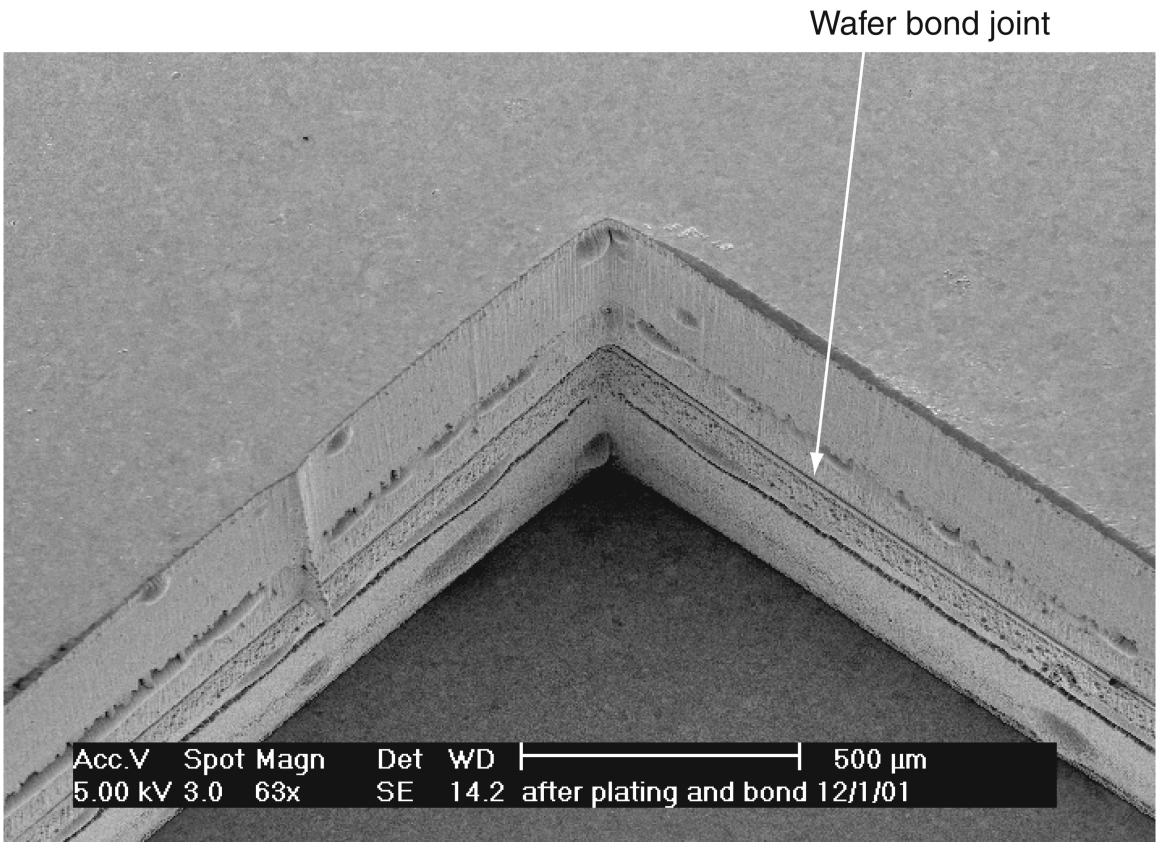

Figure 5.15: SEM image illustrating cavity wafer alignment and bond. Shown is the inside corner of one of the cavities.

fabrication procedures will include a high temperature outgassing of the wafers prior to metallization and plating.

5.4.2 RIE Tolerances

The RIE etching, although it typically creates very vertical sidewalls, can also result in slight angular sidewall undercut, also known as re-entrant or negative profile. Undercut can be controlled by reducing the platen power, which affects the energy at which the accelerated ions strike the wafer. A 10% reduction in platen power, from 25 W to 22.5 W, was found to alleviate the negative profile somewhat, but not entirely. The degree of the undercut was not so severe that a re-characterization of the etch recipe was necessary.

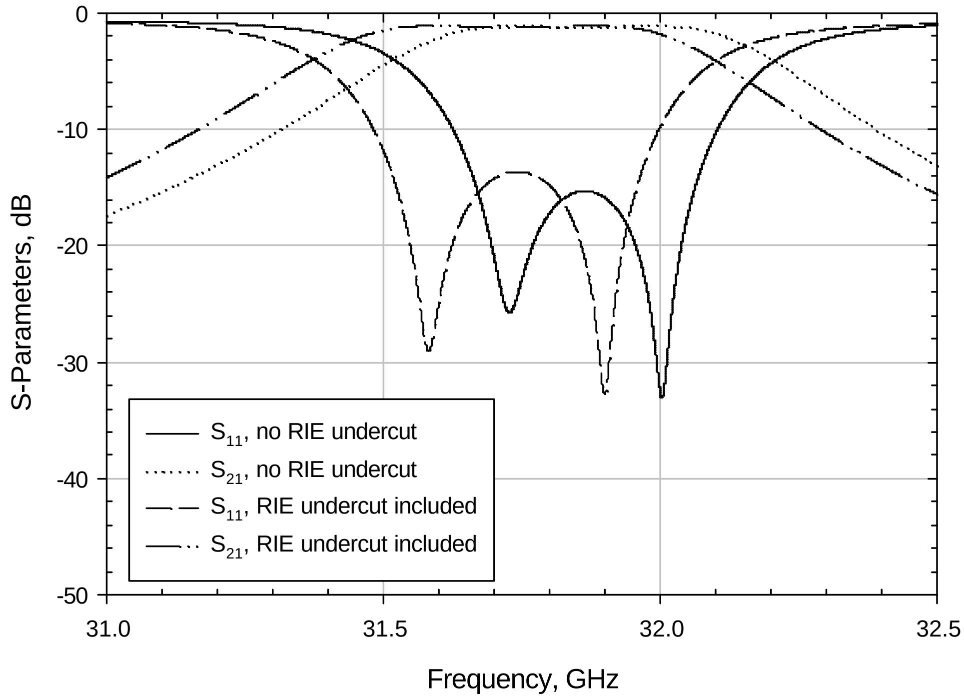

Figure 5.16: Comparison of HFSS results for filter. One model is the original design, without the sidewall undercut. The other model includes the sidewall undercut due to the RIE etch.

The undercut of the cavity and coupling section sidewalls was evaluated with the aid of the SEM. Undercuts of 12 μm in the coupling section for 250 μm of vertical etch and 24 μm in the cavity sidewalls for 500 μm of vertical etch were incorporated into the HFSS model. The undercut of the sidewalls resulted in a slight oversize of the cavities, producing a shift to a lower frequency. Comparison of the original HFSS filter model, both with and without the transition and sidewall undercuts, is shown in Fig. 5.16.

5.4.3 Transition, Filter and Q_u Measurements

The finished 2-pole Chebyshev filter and various CPW-microstrip transitions in back-to-back through-line configurations were measured on the HP8510C Network Analyzer following a TRL calibration [34]. The calibration moves the reference planes to the start of the CPW radial stub transition as indicated in Fig 5.8. The measurement repeatability error is on the order of ±0.1 dB. A comparison of measured and IE3D simulated results for a CPW-microstrip transition with microstrip length of 926 μm, as pictured in Fig. 5.8, are presented in Fig. 5.17 for 20 to 40 GHz. The loss per transition is found to be 0.2 dB at 31.7 GHz, and the bandwidth is more than adequate for measuring the filter. The measured filter results are shown compared with the HFSS model, with sidewall undercut included, in Fig. 5.18. The measured bandwidth is 2.2% centered at 31.70 GHz with an insertion loss of 1.6 dB. The modeled bandwidth is 2.3% centered at 31.74 GHz with an insertion loss of 1.2 dB. This model does not include the CPW-microstrip transition. As the total loss due to the transitions is only 0.4 dB, de-embedding of the measured data was not performed. When the loss per transition is considered, the measured filter is brought into very good agreement with the modeled filter. The bandwidth and the overall shape of the measured filter are also in excellent agreement with the model.

A transmission-type measurement of the unloaded Q requires the calculation of the loaded Q, which is proportional to the inverse of the 3 dB fractional bandwidth, FBW, at the resonance frequency fo,

$$Q_l = \frac{f_o}{f_2 - f_1} = \frac{1}{FBW} \tag{5.1}$$

The unloaded Q is then determined from

$$Q_u = \frac{Q_l}{1 - S_{21}(f_o)} \tag{5.2}$$

where $S_{21}(f_o)$ is the linear magnitude of the insertion loss at the resonance frequency. These equations hold for equal input and output couplings. If coupling is over-critical, $|S_{21}|$ approaches unity, so a small error in the evaluation of $|S_{21}|$ may yield a large error in Q_u. Weakly coupling the resonator reduces the risk of this error, producing a

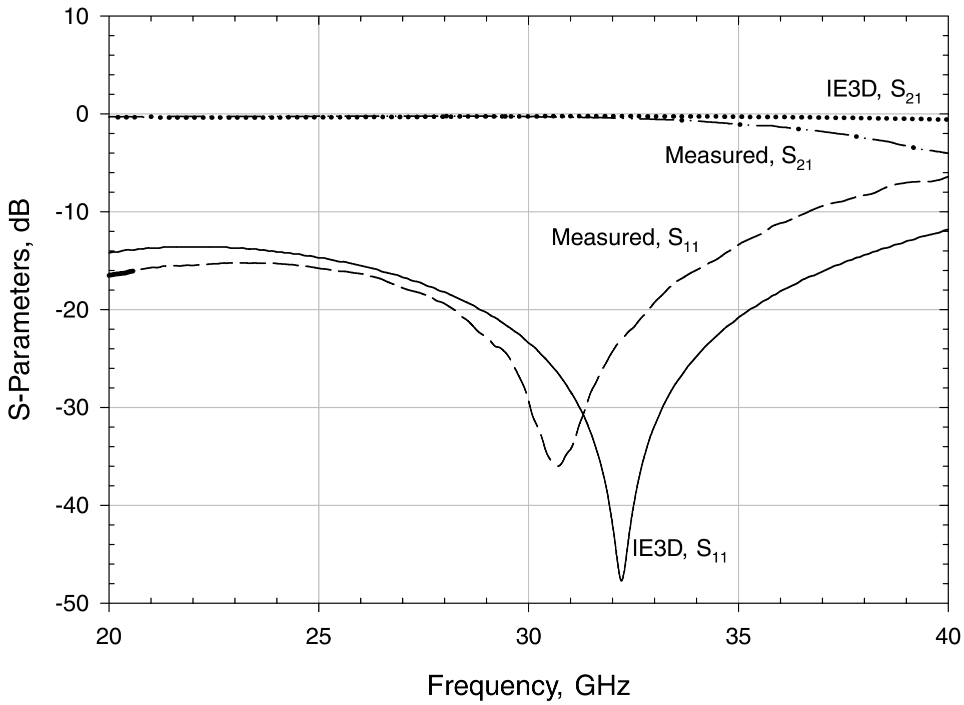

Figure 5.17: Comparison of IE3D and measured results for via-less CPW to microstrip transition in a back-to-back configuration. Microstrip is 926 μm long.

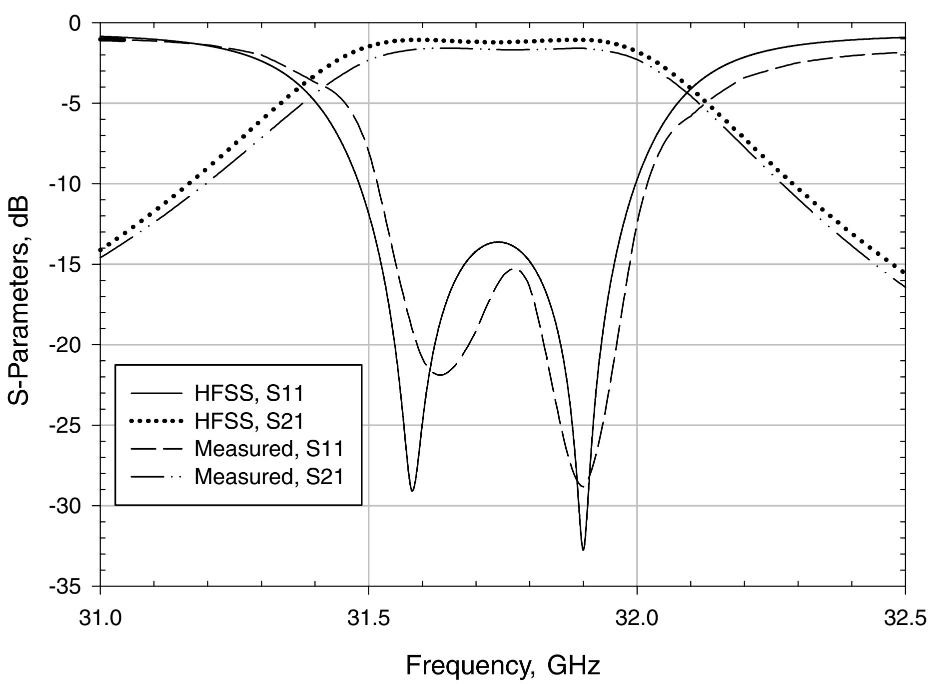

Figure 5.18: Measured and HFSS S-parameters for complete filter. Model includes undercut sidewalls.

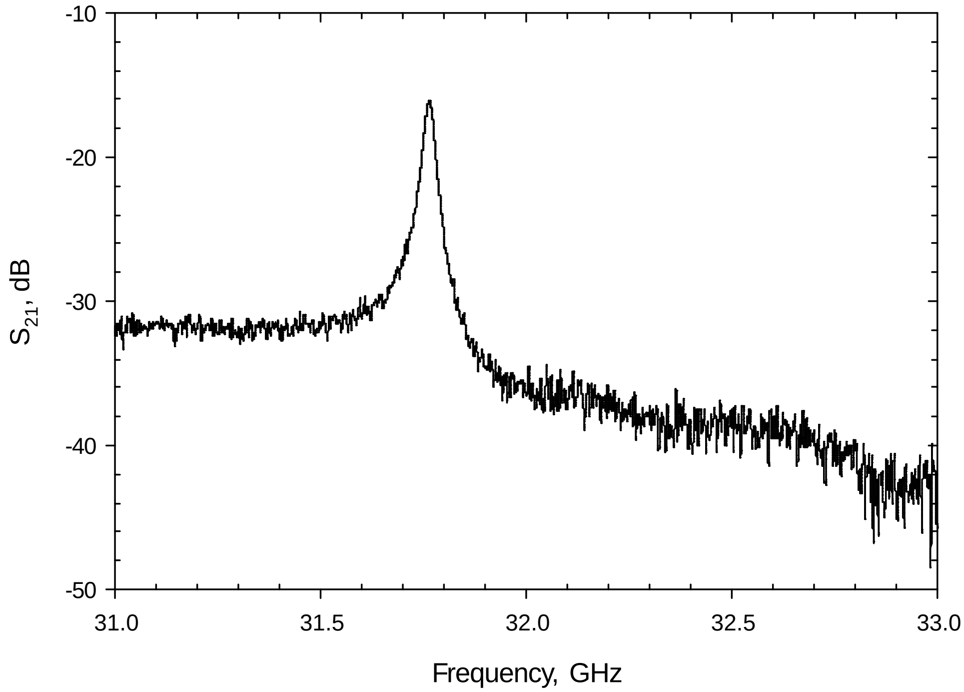

Figure 5.19: Q_u measurement from single, weakly-coupled cavity.

more accurate estimation of the Q_u, given enough data points to correctly deduce the 3 dB fractional bandwidth [77]. HFSS simulations of a microstrip-fed, slot-coupled single cavity whose slots are 0.7 mm $\times$ 0.1 mm in dimension produced a weak coupling that yielded a resonance at 31.773 GHz. An on-wafer, single, weakly coupled cavity was fabricated with slots of this size, measured and found to have a Q_u of 1422 resonant at 31.7635 GHz as shown in Fig 5.19. The theoretically calculated Q_u for the TE_{101} mode for a filter with air-filled cavities of this size is 1670 from (1.3) ($\sigma_{au} = 3.9 \times 10^7$ S/m) at this frequency. This measurement was taken at the same time as those that will be presented in Chapter 6 of this thesis. When measured, the CPW-microstrip transition used in that work was found to have a narrower usable bandwidth than anticipated, which will be discussed in Chapter 6. As a result, the Q_u measurement at 31.7635 GHz was just past the edge of the bandwidth upper limit, and was subsequently adversely affected by the decrease in return loss. This accounts, in part, for the disagreement with theory.

As discussed in Chapter 2, HFSS and other FEM and MoM simulation packages often model conductors as infinitely thin metal sheets with some finite conductivity and do not compute the volume current in the metal. The equation used to calculate the theoretical Q_u, (3.9), is derived from the average power dissipated in the cross-sectional volume of the conducting walls as given by Joule's law,

$$P^t = \frac{1}{2}\int_V \bar{E} \cdot \bar{J}^* \mathrm{d}v = \frac{1}{2\sigma}\int_V |\bar{J}|^2 \mathrm{d}v \tag{5.3}$$

The derivation is based on a surface impedance concept to determine the effect of conductor loss and does not compute the fields inside the conductor. An assumption is made that the exponentially decaying volume current in (5.3) can be replaced with a uniform volume current extending only one skin depth into the conductor, and is zero elsewhere. This assumption carries through to the derivation for (3.9) and contributes to the over-estimation of the theoretical Q_u [23, 47]. A nice illustration of these effects for various modeled and measured Q_u's for microstrip resonators is given in Table 2.1 of [6]. It is shown that the calculated and modeled values for Q_u may overestimate the measured by as much as 34%.

5.5 Summary

A 2-pole, micromachined, horizontally integrated bandpass filter has been successfully demonstrated. It is lightweight, of compact size, and may be easily integrated into a monolithic circuit. The measured results show a filter response that is in excellent agreement with the simulated model, and a good Q_u value.

The alignment and bonding issues seem to be resolved with the fabrication presented in this chapter. With the success of the horizontally oriented design, the next step is to investigate a multiple-pole filter with non-adjacent cavity coupling for the purpose of producing an elliptic or linear phase response.

CHAPTER 6

A Horizontally Integrated Micromachined Linear Phase Filter

The soft drops of rain pierce the hard marble, many strokes overthrow the tallest oaks.

John Lyly, Euphues, 1579

6.1 Introduction

SIGNAL distortion is the result of non-linear phase filter transfer functions. Group time delay is defined as the time required for a frequency signal packet to pass through the filter. If different components of that signal packet arrive at the filter output port at different times, the signal is distorted. As group delay is the first derivative of phase with respect to frequency, linear phase means flat group delay, or an absence of signal distortion [63]. It is desirable to have as little signal distortion as possible in some communication applications, and therefore, we investigate the feasibility of a linear phase filter based on the horizontally integrated micromachined cavity concept.

A 4-pole filter with one cross-coupling is about the simplest realization of this concept and therefore was chosen to prove the validity of the design and fabrication processes. A filter model with 2.2% fractional bandwidth at 27.48 GHz was designed. The measured response exhibited a 1.9% bandwidth at 27.604 GHz with a Q_u of 1465. Schematics of the completed filter model are given in Figs. 6.1 and 6.2.

6.2 Background

A linear phase response can be achieved by providing coupling between electrically non-adjacent resonators, or cross-couplings. The cross-couplings present multiple paths to the signal between the input and output ports. Given the correct amplitude and phase, the signals can cancel each other out. Hence, transmission zeros appear in the transfer function, located in the right-half of the complex frequency plane. This results in attenuation poles at either real, finite frequencies (elliptic response) or at imaginary frequencies (linear phase response).

Some of the original work on cross-coupling was done by J. R. Pierce in 1948 [78], which used a multipath filter to achieve a linear phase response. Later, work by R. M. Kurzrok [79, 80] and E. C. Johnson [81] described cross-coupled filters of three or four cavities, producing finite frequency attenuation poles through negative cross-coupling (elliptic response). Although they discussed the reduction in out-of-band roll-off produced by positive cross-coupling, they fail to mention the improvement in linear phase response as a trade-off. The importance of linear phase, or equalized delay, became apparent during the onset of the development of satellite communication technology in the late 1960's. The methodology was greatly advanced by J. D. Rhodes [16, 82, 83, 84] who developed synthesis techniques for generalized interdigital and direct-coupling cavity linear phase filters. Work in the 1970's was advanced by A. E. Atia and A. E. Williams at COMSAT [85, 86, 87], using dual-mode cavities with cross-coupling, producing both elliptic and linear phase options [88].

More recent work into dual-modes, cross-couplings, and evanescent waveguide

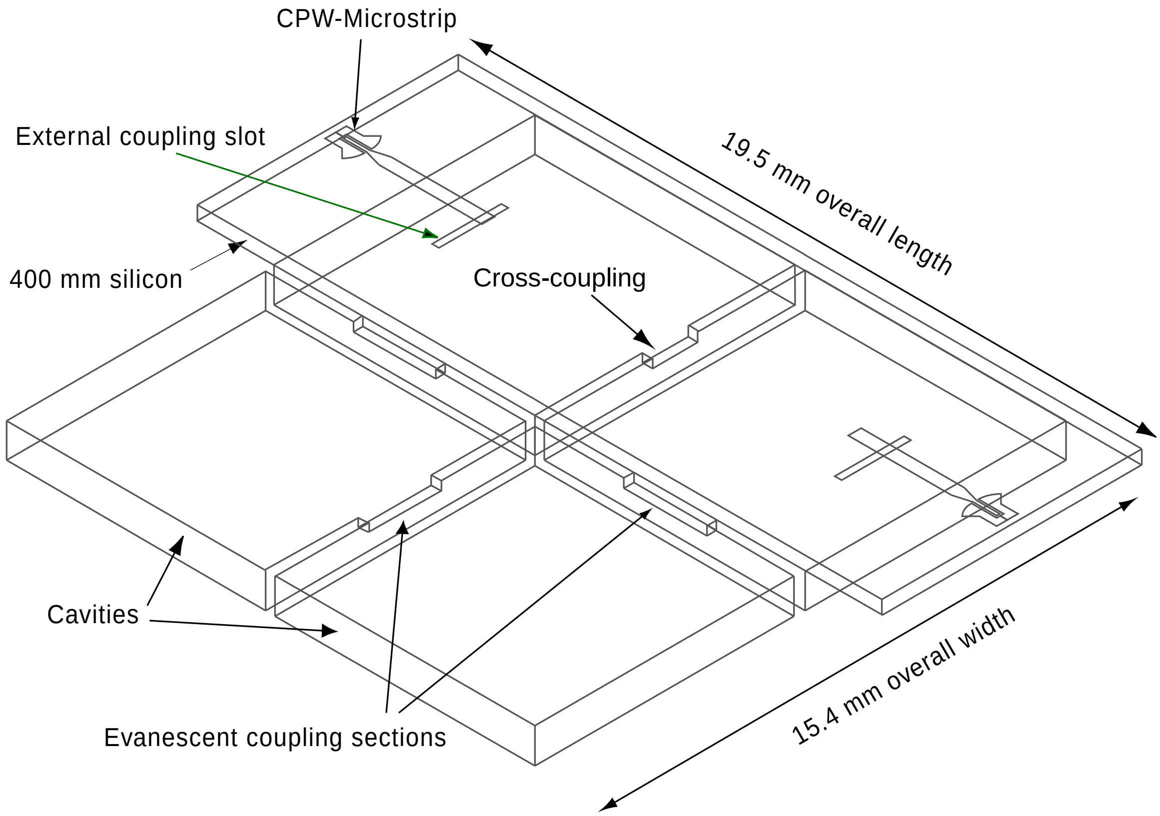

Figure 6.1: Cross-sectional schematic of 4-pole linear phase filter. View is to scale.

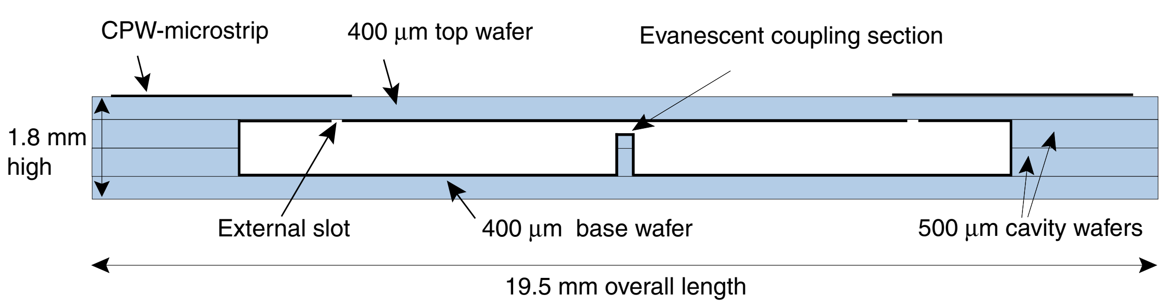

Figure 6.2: Side view schematic of 4-pole linear phase filter. View is not to scale.

couplings includes the design technique described in [73] for dual-mode microwave waveguide filters coupled by evanescent waveguides for an elliptic filter response. In [89], waveguide cavity elliptic filter design is applied to dual-plane microstrip resonators coupled by slots in a common ground plane. Both electric and magnetic coupling are developed to provide the necessary transmission zeros. Cross-coupling tuning screws are eliminated by altering the circular cross-section of a dielectrically-loaded cylindrical waveguide to include flats that couple orthogonal modes in [90]. Although the work presented in this chapter is based on positive cross-coupling for a linear phase response, and not an elliptic response, it is hoped that the success of this work will justify the continued investigation of more complex filter design based in semiconductor processing techniques.

One way to realize a linear phase filter is to design a filter with a pair of transmission zeros on the real axis of the complex frequency plane, with a positive cross-coupling of non-adjacent resonators. It can be shown that the phase error function, which tracks phase deviation from linearity, vanishes at equally spaced points along the real axis [83]. It's derivative, the group delay error function, approaches a constant as ω approaches infinity. In [82], it was shown that if the cross-couplings have the same phase (sign) as the direct couplings, then the transmission zeros are either complex or on the real axis in the complex frequency plane. Hence, to produce a linear phase filter, it simply remains to design a cross-coupling with the same kind of coupling behavior as the direct coupling, i.e., so that both couplings are either electrical or magnetic, both capacitive or both inductive.

6.3 Design and Simulation

6.3.1 Background

The design of the linear phase filter follows the approximate synthesis procedure of [91, 92] and will be summarized here. It is based on a Chebyshev design with one added cross-coupling and an adjustment for the mistuning created by the cross-coupling.

The low-pass prototype filter, as shown in Fig. 6.3 for an even number of resonator elements, consists of n shunt resonators coupled by admittance inverters. It is the dual circuit of that illustrated in Fig. 4.2. The prototype element values are given in [91] by

$$\begin{aligned} g_1 &= \frac{2\sin\frac{\pi}{2n}}{\gamma} \\ g_r g_{r-1} &= \frac{4\sin\frac{(2r-1)\pi}{2n}\sin\frac{(2r-3)\pi}{2n}}{\gamma^2+\sin^2\frac{(r-1)\pi}{n}} \quad (r=1,2,\ldots m), \quad m=n/2 \\ \gamma &= \sinh\left(\frac{1}{n}\sinh^{-1}\frac{1}{h}\right) \\ S &= (\sqrt{1+h^2}+h)^2 \\ J_m &= \sqrt{S}\ldots m \quad \text{odd or} \quad 1/\sqrt{S}\ldots m \quad \text{even} \end{aligned} \tag{6.1}$$

where S is the passband VSWR and h is the passband ripple. For a Chebyshev filter, there would be no cross-coupling, and J_{m-1} would be 0. For transmission zeros to occur at an imaginary frequency $\omega = j\sigma$, J_{m-1} must satisfy

$$J_{m-1} = \frac{J'_m}{(\sigma g_m)^2 + (J'_m)^2} \tag{6.2}$$

where J_m is slightly altered due to the mistuning of the filter caused by the introduc-

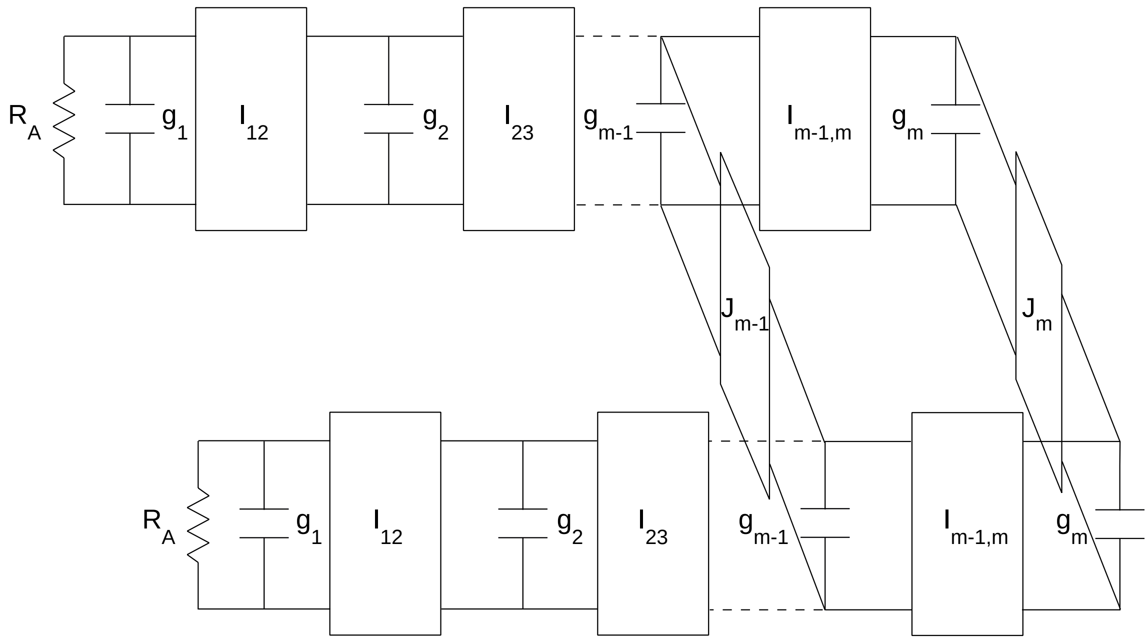

Figure 6.3: Low-pass prototype filter for an even number of resonators, $m - n/2$.

tion of the cross-coupling, and must be replaced by J'_m,

$$J'_m = \frac{J_m}{1 + J_m J_{m-1}} \tag{6.3}$$

The equations for J_{m-1} and J'_m are determined by manipulating the admittance matrix for that portion of the circuit shown in Fig. 6.3 between nodes 1 and 4 to achieve zero transmission between these nodes. The adjustment to J_m is determined by equating that portion of the circuit with a circuit without the cross-coupling at $\omega = 0$, see Appendix 1 of [91].

6.3.2 Design

In previous filter designs, HFSS alone was used to model the filter from scratch. In this design, an equivalent lumped element circuit was designed in ADS and whose response was used as the goal to which the HFSS model was designed. The ADS model elements were determined from the prototype parameters as outlined above.

The design was chosen for a resonance frequency ω_o of 27.57 GHz, a 0.1 dB ripple and a ripple bandwidth Δ of 1.65%. The ADS model was designed to be a symmetric ladder circuit with shunt RLC resonators and series C couplers as shown in Fig. 6.4. The first and fourth resonators were equal, as were the second and third resonators, and the first and last inter-cavity couplings were equal. The initial values for the resonator L's and C's are given by

$$\begin{aligned}
C'_1 = C'_4 &= \frac{g_1}{\Delta\omega_o} \\
C'_2 = C'_3 &= \frac{g_2}{\Delta\omega_o} \\
L'_1 = L'_4 &= \frac{\Delta}{g_1\omega_o} \\
L'_2 = L'_3 &= \frac{\Delta}{g_2\omega_o}
\end{aligned} \tag{6.4}$$

where the g_j values are given by (6.1), and the above equations are simply the frequency transform from the original prototype parameters, where $C_j = g_j$ and $L_j = 1/g_j$. The first to second cavity coupling C_{12} and the third to fourth cavity coupling C_{34} are given by

$$\begin{aligned}
C_{12} = C_{34} &= \frac{J_{12}}{\omega_o} = \frac{J_{34}}{\omega_o} \\
&= \frac{\Delta}{\omega'_1}\sqrt{\frac{C'_1 C'_2}{g_1 g_2}} = \frac{\Delta}{\omega'_1}\sqrt{\frac{C'_3 C'_4}{g_3 g_4}}
\end{aligned} \tag{6.5}$$

where the expressions for $J_{j,j+1}$ are found in [63].

The cross-coupling C_{m-1} and the second to third cavity coupling C_m are also given in [63] by

$$\begin{aligned}
C_{m-1} &= \frac{J_{m-1}}{\omega_o} \\
C_m &= \frac{J'_m}{\omega_o}
\end{aligned} \tag{6.6}$$

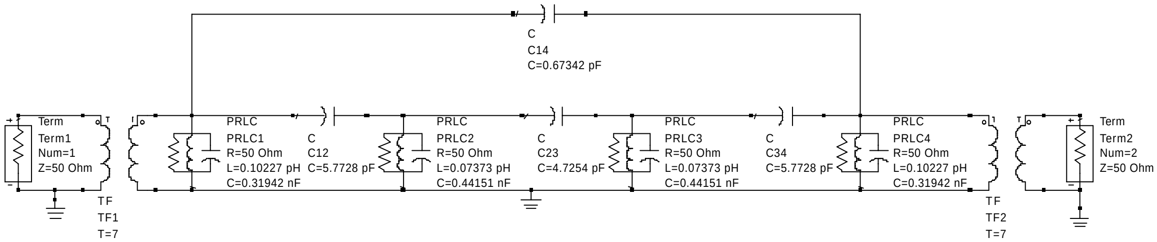

Figure 6.4: Complete ADS 4-pole linear phase lumped element filter model.

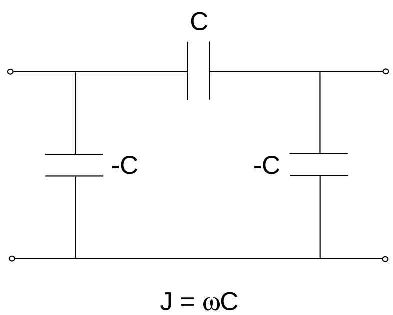

Figure 6.5: Admittance inverter used in ADS lumped element filter design.

where J_{m-1} and J'_m are given by (6.2) and (6.3).

The admittance inverter used in this design is shown in Fig. 6.5. Once determined, resonator values must be adjusted by subtracting from the resonator capacitor value the coupling capacitor values on either side. Hence, the C'_1 and C'_2 values are appropriately adjusted.

The external coupling in this model was supplied by a transformer whose turns ratio was adjusted manually to produce the best response. Other than that adjustment, no fine-tuning was necessary for the ADS model. The 1.65% ripple bandwidth design produced a 2.2% 3 dB fractional bandwidth at 27.57 GHz, and the response for the complete model is given in Fig. 6.6. The phase angle for S_{21}, which is quite linear, is shown with the ripple bandwidth indicated.

The initial HFSS design was performed in the same manner as in the previous chapters: a single cavity was used to determine a design external coupling, and two coupled cavities were used to determine design internal couplings. The layout of the

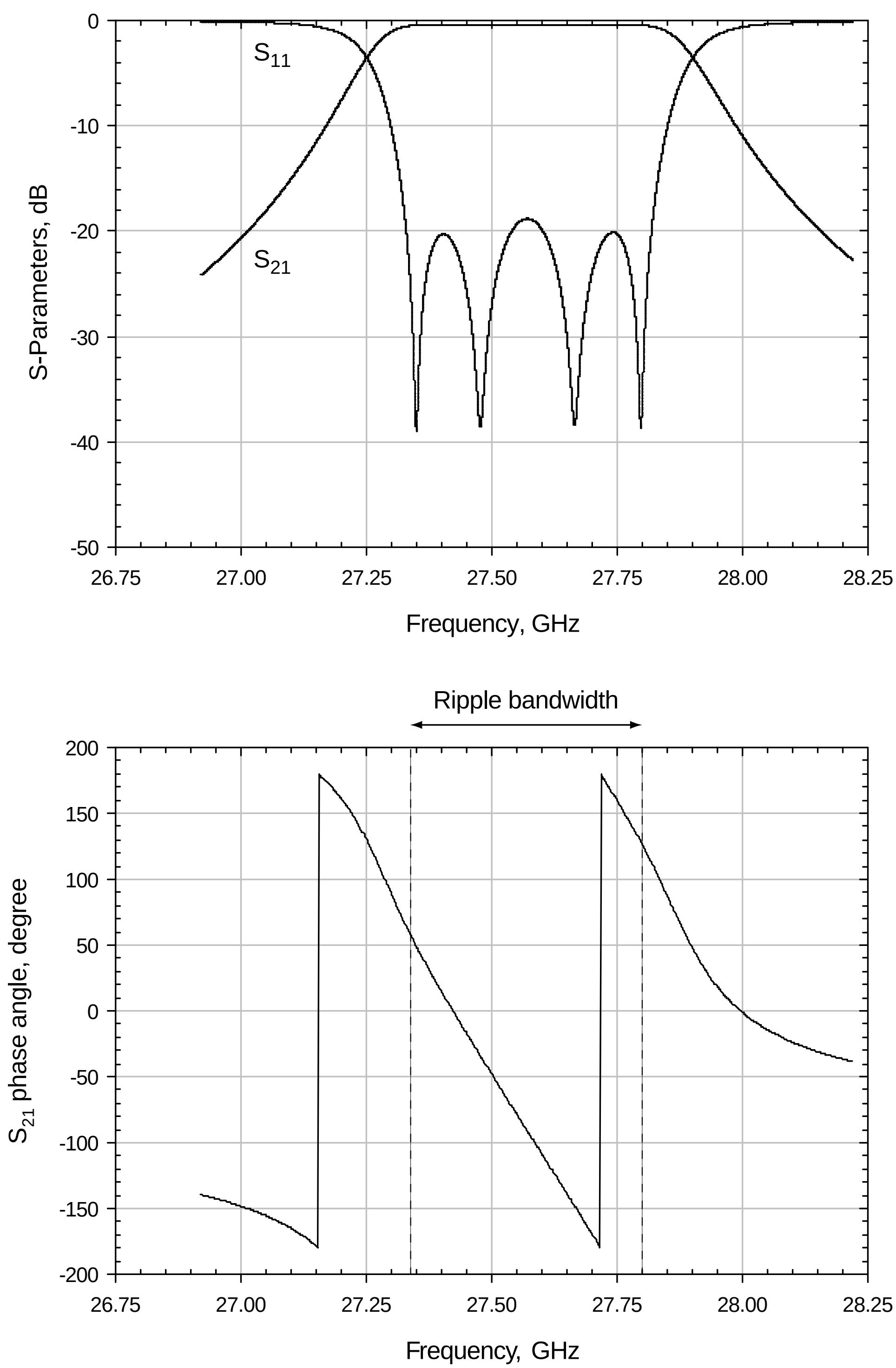

Figure 6.6: Frequency and phase response for ‘ideal’ ADS model.

HFSS model was the same as in Chapter 5, with microstrip-fed, slot-coupled cavities in a horizontal orientation and evanescent inter-cavity coupling sections. The resonator sizes were determined to match the resonance frequencies of the ADS resonators. The external couplings were based on equations (4.24) and (4.25), where $g_0 = 1$ and g_1, g_n, g_{n+1} are given by (6.1). The modeled Q_e's were based on (4.36).

The prototype first and last inter-cavity couplings were based on (4.20). The modeled coupling coefficient k was based on (4.29). The other coupling coefficients were based on equations for the admittance inverter susceptance obtained from [16],

$$B_r = \frac{K_r}{\alpha C_r} \rightarrow B_m = \frac{J'_m}{\alpha g_m}, \quad \text{where} \quad \alpha = \frac{\omega'_1(f_2 + f_1)}{\pi(f_2 - f_1)} \tag{6.7}$$

and where f_1 and f_2 are the band edge frequencies. The above equation is for the coupling susceptance between the second and third cavities. Replacing the subscript m with $m-1$ yields the equation for the cross-coupling susceptance.

An explicit relationship joining the coupling susceptance B and the coupling coefficient k was not found. However, given the similarity of the expressions it was deemed prudent to assume the two were nearly equal. Based on this assumption, and the explicit calculations stated above, an initial HFSS model was designed. A schematic of the model is shown in Fig. 6.1, although the HFSS model did not include the CPW-microstrip transition. The initial frequency response is shown in Fig. 6.7 compared with the ideal ADS frequency response.

A via-less CPW-microstrip transition designed for 50 Ω impedance on 400 μm substrate was used with this filter. Although the design on 200 μm substrate gave the best simulation results, this wafer cracked during the last bond, perhaps because it was too thin and fragile to survive direct contact with the bonding pressure plate. Also, the 200 μm wafers are only slightly less fragile than the 100 μm wafers. Both wafers must be mounted on carrier wafers or glass slides for stability during handling

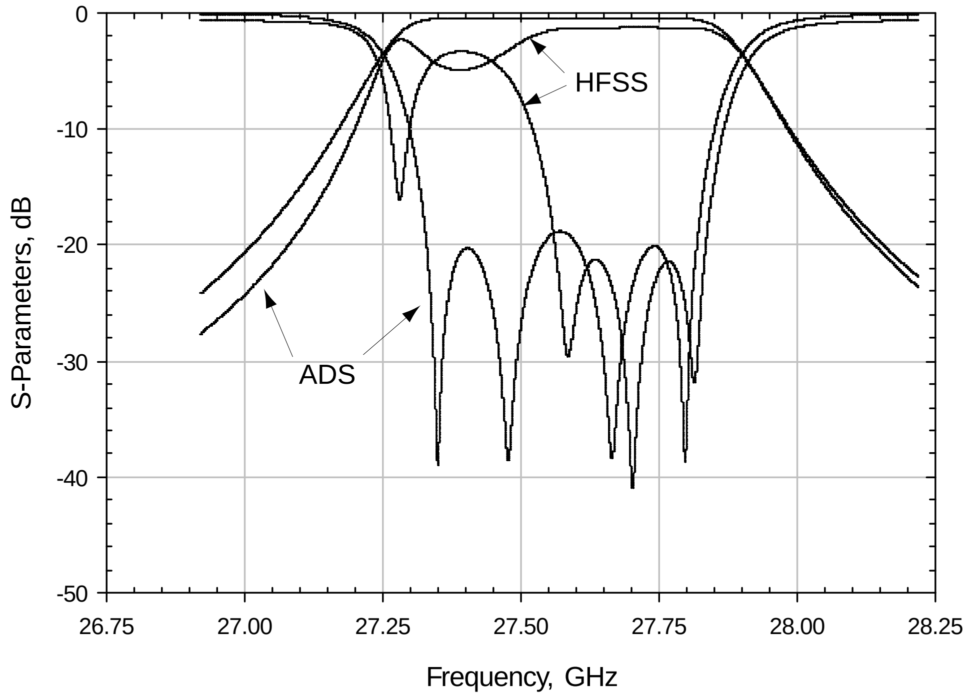

Figure 6.7: Frequency response comparison of initial HFSS model and ideal ADS lumped element model.

and processing. The 400 μm substrate design has a CPW pitch of 58.56-90-58.56 μm and a CPW-radial 45° stub taper length of 500 μm total. The IE3D response for a microstrip width and length of 374 μm $\times$ 2.4 mm in a back-to-back through-line configuration is given in Fig. 6.8. The modeled insertion loss for this design is 0.3 dB at 27.6 GHz. This transition was not included in the completed HFSS model.

6.3.3 Time Domain Tuning

In the previous filter designs, an initial HFSS model was determined by calculation, and the complete model was fine-tuned by slight alteration of each cavity and each coupling until the filter response was optimized, a tedious and computationally intensive process. It is quite difficult to tell from a given sub-optimal frequency response exactly which parameters are responsible for the mistuning. The interdependence of the elements complicates the tuning process. One coupling loads the

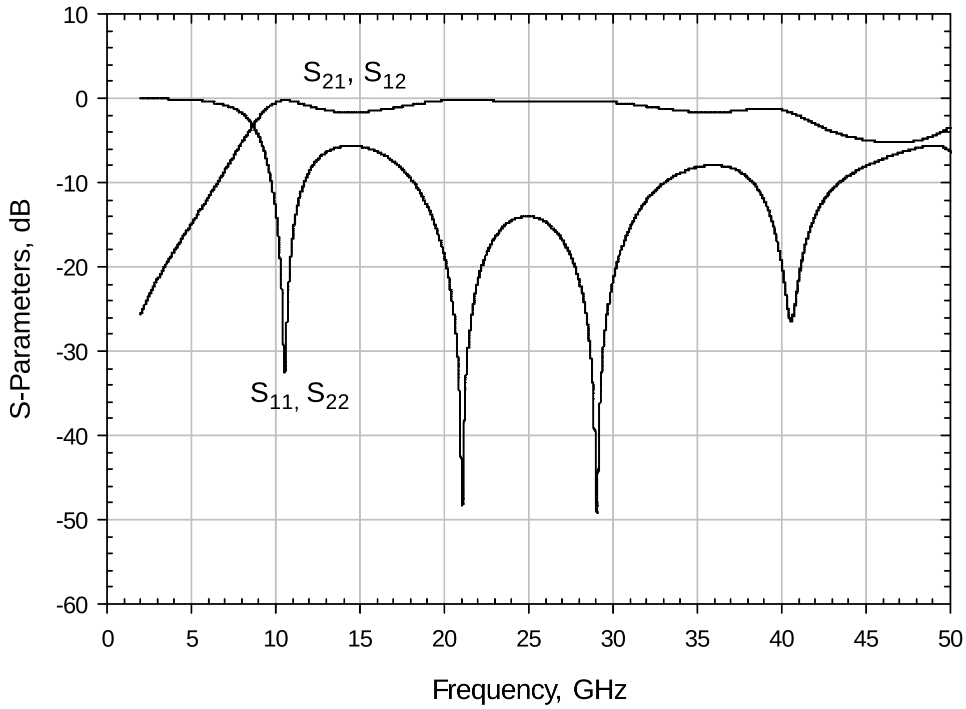

Figure 6.8: IE3D response for via-less CPW-microstrip radial stub transition on 400 μm silicon.

resonator, pulling it off resonance, multiple couplings even more so. Re-tuning the resonator requires re-tuning the coupling and the adjacent resonators. A better way to design and tune filter models is to examine the time domain response of the filter at each stage of the fine-tuning process. The approach to this method as used in this work is described in [93] and [94].

The return loss for each port as observed in the time domain exhibits reflections at each discontinuity. The nulls in the response represent the node resonance at each resonator, and the peaks represent reflections at each coupling. An illustration is given in Fig. 6.9 which shows the time domain response for the ideal ADS lumped element model. The null corresponding to each resonator is indicated in the figure. The peaks associated with each coupling, including the external coupling, are also indicated. If properly tuned, the resonators exhibit deep nulls. It is therefore obvious which of the resonators are mistuned, although a resonator mistuned by more than

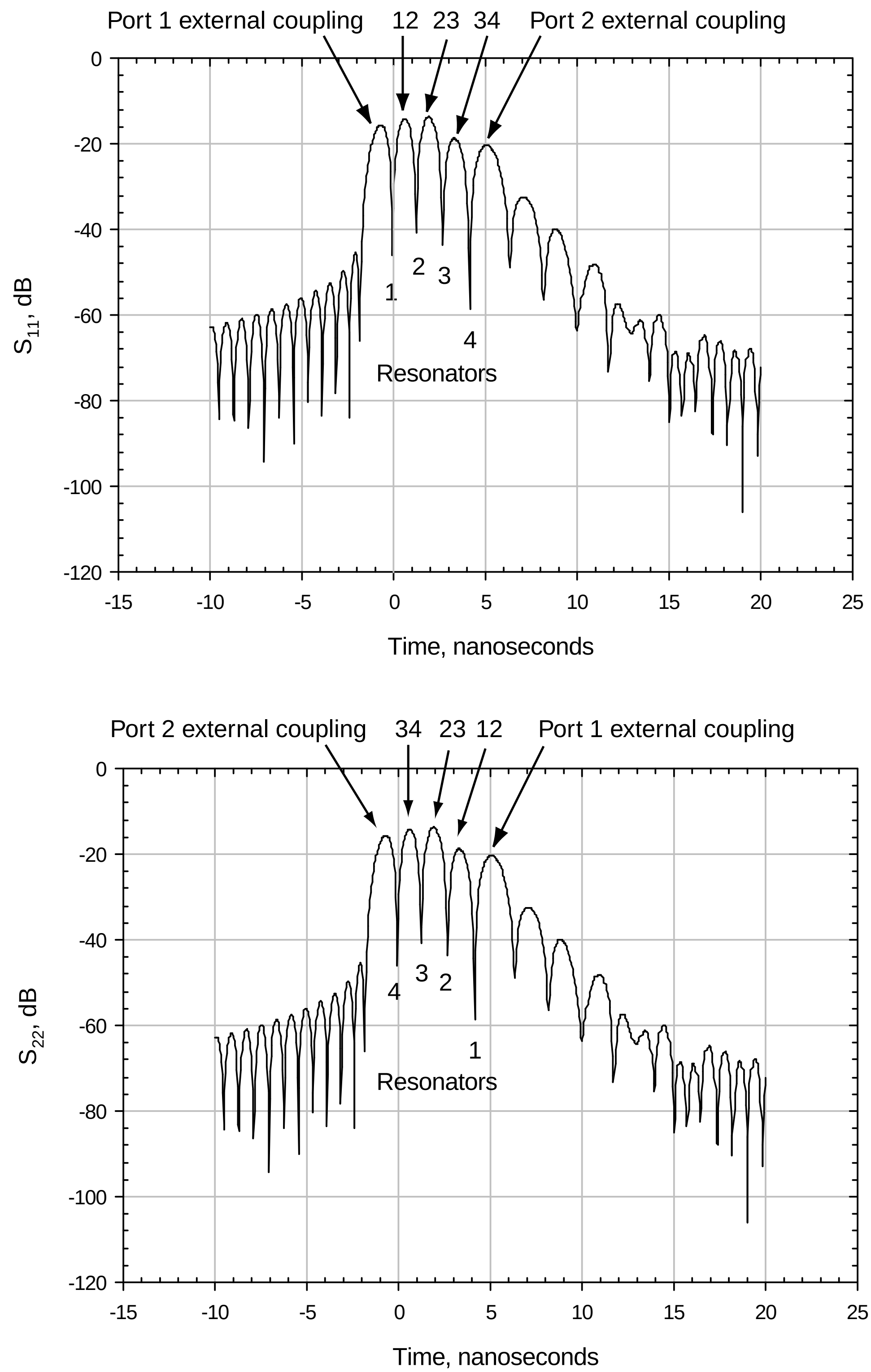

Figure 6.9: Time domain response for ideal ADS lumped element model. Nulls due to each resonator are indicated, as are the external couplings and couplings between each j,j+1 resonator.

1% will obscure the behavior of the subsequent resonators. Tuning each resonator will have some affect on the adjacent resonators; this affect is lessened as the resonators approach their proper values. The deepest nulls are only achieved when each resonator is properly tuned. Hence, the tuning is an iterative process. By using the ideal ADS lumped element model as a design goal, comparisons between the HFSS and ADS time domain responses can be made, and exactly which cavities and which couplings are mistuned can be determined.

An increase in coupling such that it is mistuned will produce a decrease in the peak associated with that coupling. An increase in coupling results in an increase in energy coupled to the following resonator, and less energy is reflected. However, this means more energy is available to reflect at the subsequent couplings, so those peaks increase. The opposite affect is seen if a coupling is decreased. In the frequency domain, an increase in coupling results in a wider bandwidth (again, more energy passes through) and a change in the return loss. A decrease in coupling results in a narrower bandwidth. However, it is difficult to tell in the frequency domain which coupling is mistuned and responsible for this bandwidth change.

An illustration is given in Fig. 6.10 which shows the frequency and time domain response for the HFSS model for a change in inter-cavity coupling. In the top two graphs, (a), the inter-cavity couplings 1 to 2 and 3 to 4 are both 2.366 mm wide, although only the S_{11} time domain results are presented. In the bottom two graphs, (b), the same couplings are decreased to 2.27 mm wide, a change of about 4%. Again, the width and height of the coupling section are the cross-sectional dimensions. All other dimensions are equal between the two sets of graphs. The time domain graphs include the ideal ADS response for comparison. The top arrows indicate the peaks associated with the couplings. There is a slight improvement in both the frequency and the time domain responses for the (a) graphs, which are for the larger coupling dimension. In the frequency graph, three poles are obvious. By improving the cou-

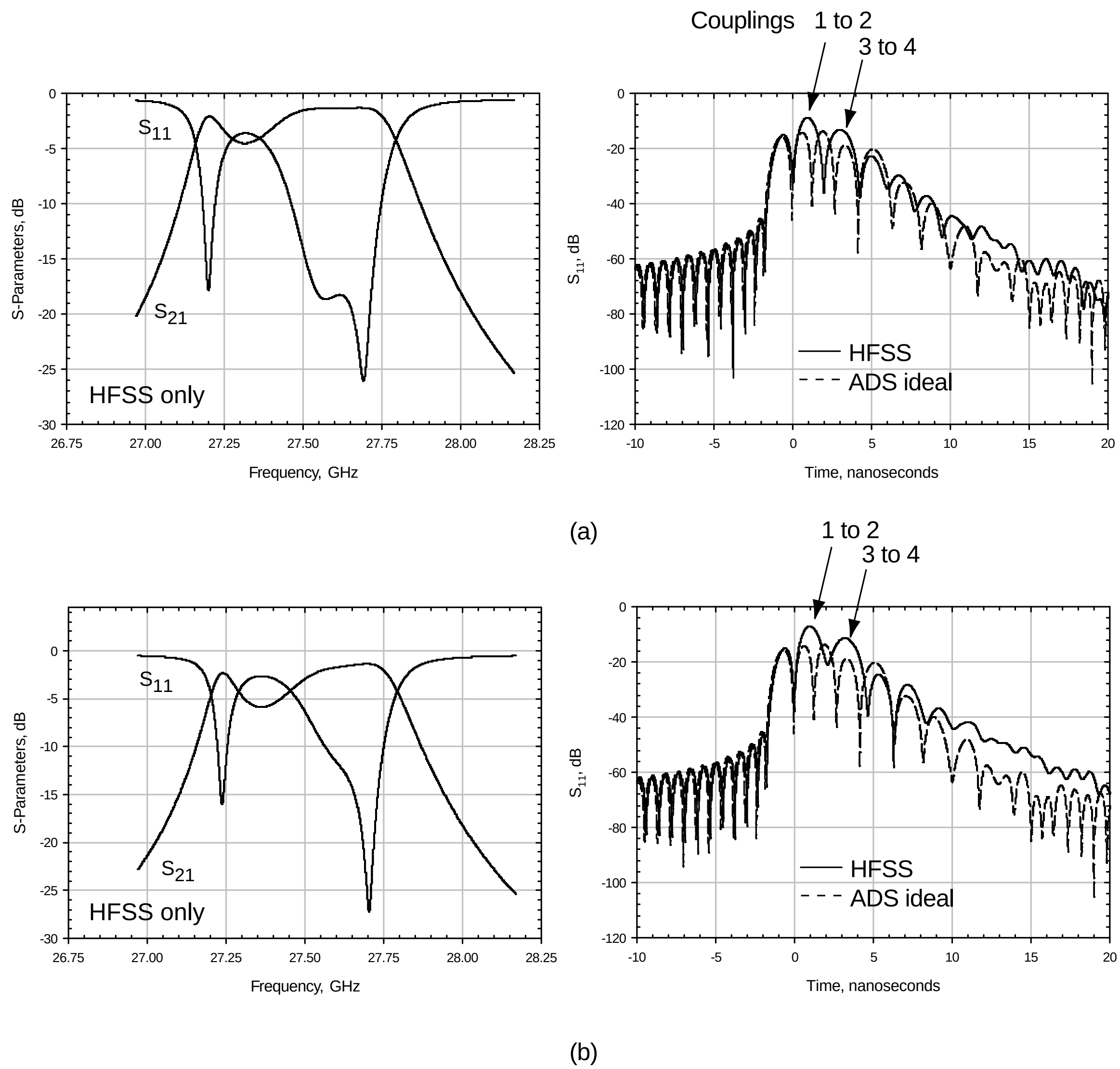

Figure 6.10: Illustration of change in frequency and time domain responses for a 4% reduction in HFSS model inter-cavity couplings between graphs (a) and (b). Time domain graphs include comparison with ADS ideal model. Arrows indicate inter-cavity couplings 1 to 2 and 3 to 4.

pling from the 1st to the 2nd resonator, the second null, which is associated with the second resonator, is improved. Tuning the coupling results in less energy reflection, and therefore more energy delivered to the next resonator. In frequency graph (b), only two poles are obvious, and the second null in the time domain graph is not as deep.

There should be four poles present in the frequency graphs. At best, barely three are visible due to mistuned, over-couplings. It is not clear from the frequency domain which couplings are mistuned, but from the time domain it is readily obvious. Both time domain plots presented in Fig. 6.10 exhibit one resonator null where there should be two, at the 3rd and 4th resonators. This indicates that the coupling between the 3rd and 4th cavities is mistuned. Once the tuning of that coupling was improved, all four resonator nulls were distinguishable in time domain, and all four poles were obvious in the frequency domain, as illustrated in Fig. 6.11. These responses are the result of a reduction in coupling between the second and third cavities from a design value of 2.35 mm to 2.115 mm wide. The ADS ideal time domain response is included for comparison. Although the frequency domain graphs look quite good, it is clear from the time domain comparison with the ideal model that there is room for improvement and additional tuning of both the resonators and the inter-cavity couplings. The reflection response begins to deteriorate beyond the midpoint of the filter relative to the port due to energy reflection, hence both S_{11} and S_{22} data were used to tune the HFSS filter model.

The time domain tuning technique also helps to clarify which of the model parameters are most sensitive to small changes in dimension. To illustrate this sensitivity, consider Fig. 6.12. The model presented in (b) is identical to that presented in (a), except that the first cavity width and length dimensions are reduced by just 1% for the results presented in (b). This yields a 2% reduction in cavity volume. The comparison between Fig. 6.10(a) and (b) is for the parameter change of a 4% coupling

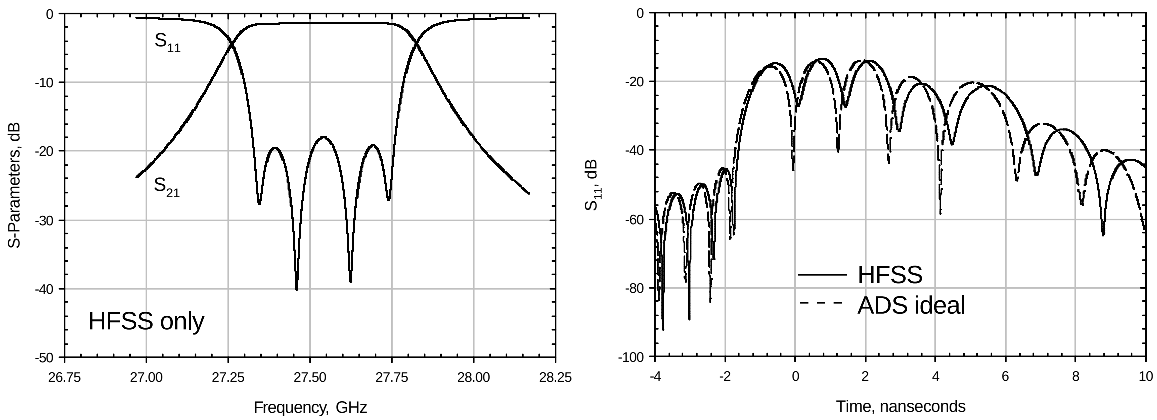

(a)

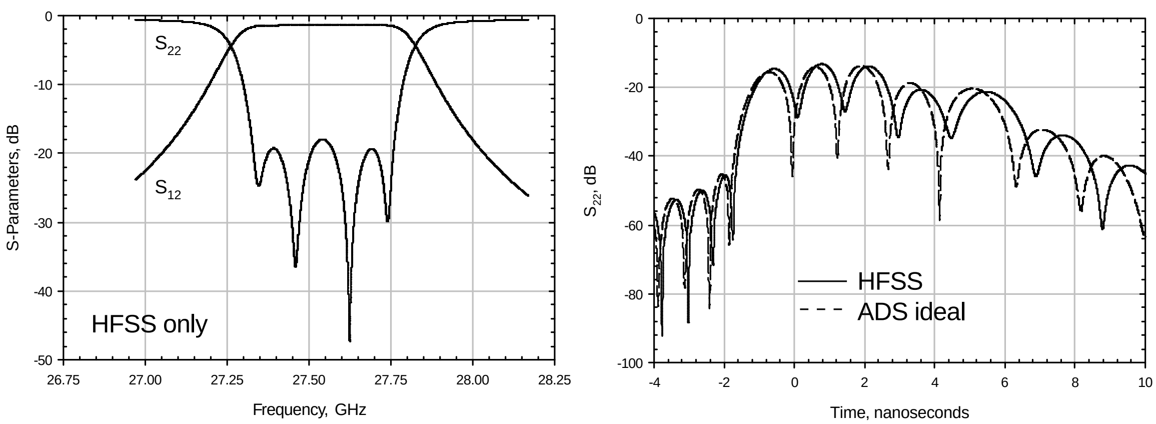

(b)

Figure 6.11: HFSS model, (a) S_{11}, S_{21} frequency domain and S_{11} time domain, (b) S_{22}, S_{12} frequency domain and S_{22} time domain. Time domain graphs include comparison with ADS ideal model.

section width reduction. These pairs of graphs exhibit similar behavior, whereas for the 1% cavity reduction, a drastic difference is seen in both frequency and time domain. In addition, in the time domain graph of Fig. 6.12(b), only two resonator nulls are visible where there should be three, and the peak that relates to the input external coupling has also been distorted due to the change in the cavity dimension. It was found that the response was consistently most sensitive to small percentage changes in cavity dimensions, and much less so to changes in the coupling sections. The response was also relatively insensitive to changes upwards of 8% in the external coupling slot length. The degree of resonator and coupling sensitivities also held true for the ADS model lumped elements. The response was most sensitive to changes in the resonator capacitors and less so to changes in the coupling capacitors. This can be explained by considering the influence of the individual parameters on the field and energy storage of the filter. The evanescent coupling sections and the coupling slots - that is, the external slots in this design and the inter-cavity slots in the design presented in Chapter 4 - all behave in an evanescent manner. There is very little field, and hence energy, concentration and storage in them. In contrast, the fields in the cavities are much stronger and the cavities store all or most of the energy. Therefore, it is reasonable to conclude from these illustrations that the evanescent coupling sections and the external slots are less susceptible to fabrication tolerances than are the cavities.

In addition, a lossless model will have higher coupling peaks than a model with loss incorporated. If it were possible to accurately model the loss of the cavity-based HFSS model with resistive lumped elements in the ADS model, this would not be an issue. However, even with resistive elements included in the ADS model, some discrepancies are likely to occur, and therefore the final tuned HFSS model will not exactly match the ideal ADS lumped element model.

The cross-coupling needed for the linear phase response has the affect of mistuning

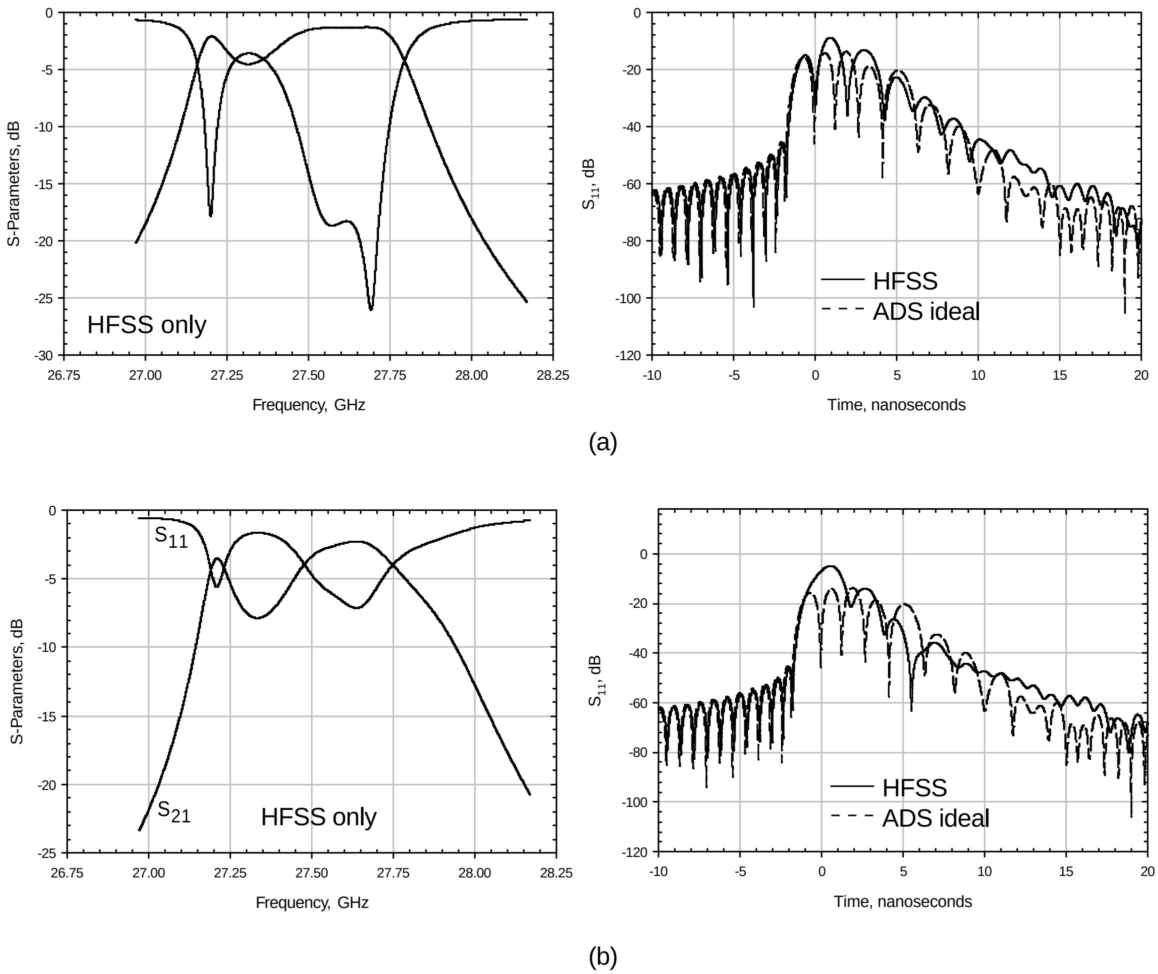

Figure 6.12: HFSS model response for 2% reduction in first cavity volume between graphs (a) and (b). Time domain graphs include comparison with the ADS ideal model.

the first and last resonators, however, the coupling itself is weak enough, compared to the other couplings, that the overall affect on the other coupling apertures is minimal. The cross-coupling was independently tuned for the best linear phase response.

The final results for the HFSS model are shown in Figs. 6.13 and 6.14. The model exhibits 1.3 dB insertion loss at 27.57 GHz and a 2.1% fractional bandwidth. Comparisons are shown with the ideal ADS model for the S-parameters, the return loss time domain responses, and the S_{21} phase angle. The HFSS model is slightly lossier than the ADS model, as anticipated. Reasonably good agreement is otherwise shown. Comparison for the S_{21} phase responses for HFSS model and a 4-pole Chebyshev ADS model, with the same center frequency, bandwidth and approximate Q_u values, is also shown in Fig. 6.14. The HFSS model exhibits an improvement in linearity over the ADS Chebyshev model.

Due to the fine-tuning of each individual parameter in the time domain, the final HFSS model for this filter exhibits asymmetry. The first (input), second, third and fourth (output) cavity dimensions are 7.6089, 7.5824, 7.5815, 7.6161 mm square, respectively. The coupling sections are all 250 μm high and 250 μm long. The widths for the first, second and third couplings, as seen from the input, are 2.409, 2.131 and 2.424 mm, respectively. The cross-coupling between the first and fourth cavities is 1.33 mm wide. The input external slot is 2.016 mm $\times$ 0.2 mm. The output external slot is 2.117 mm $\times$ 0.2 mm. Both microstrip stub lengths are 327 μm from the slot centers.

6.3.4 Time Domain Transform

An HP 8722D network analyzer was used to perform the time domain calculations. The ADS S_{11} and S_{22} frequency data were downloaded into the memory of the network analyzer, the inverse transform was performed on the memory trace, and the results were uploaded to ADS for display. The HFSS re-normalized frequency response was

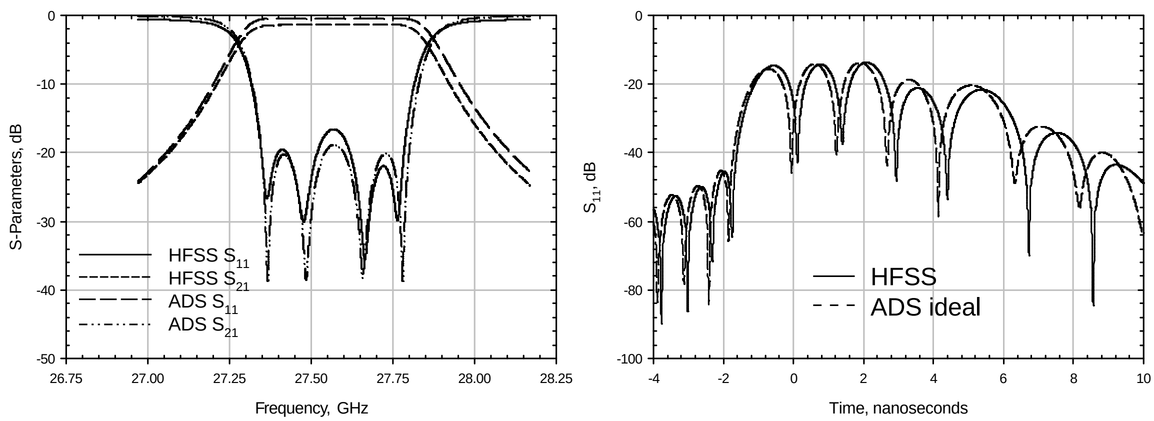

(a)

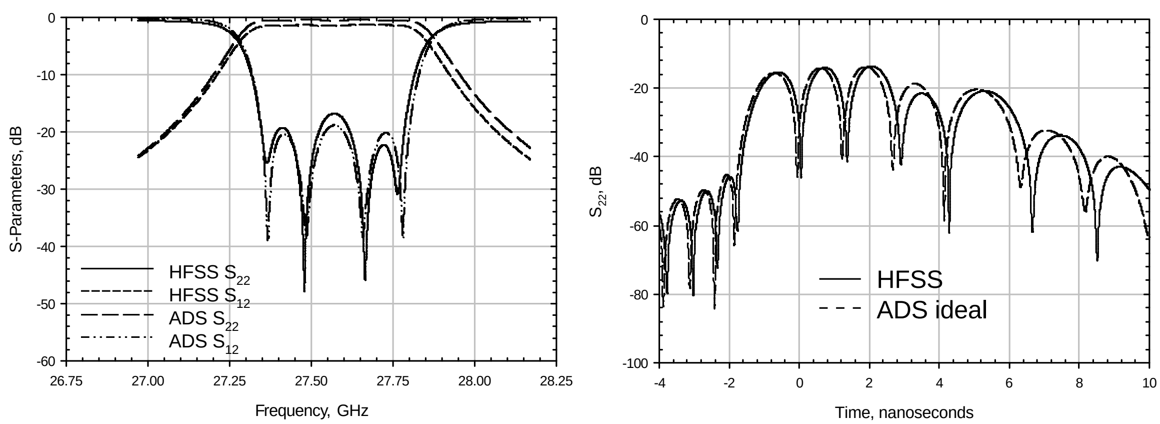

(b)

Figure 6.13: Comparison of final HFSS model and ideal ADS lumped element mode, (a) S_{11}, S_{21} frequency domain and S_{11} time domain and (b) S_{22}, S_{12} frequency domain and S_{22} time domain.

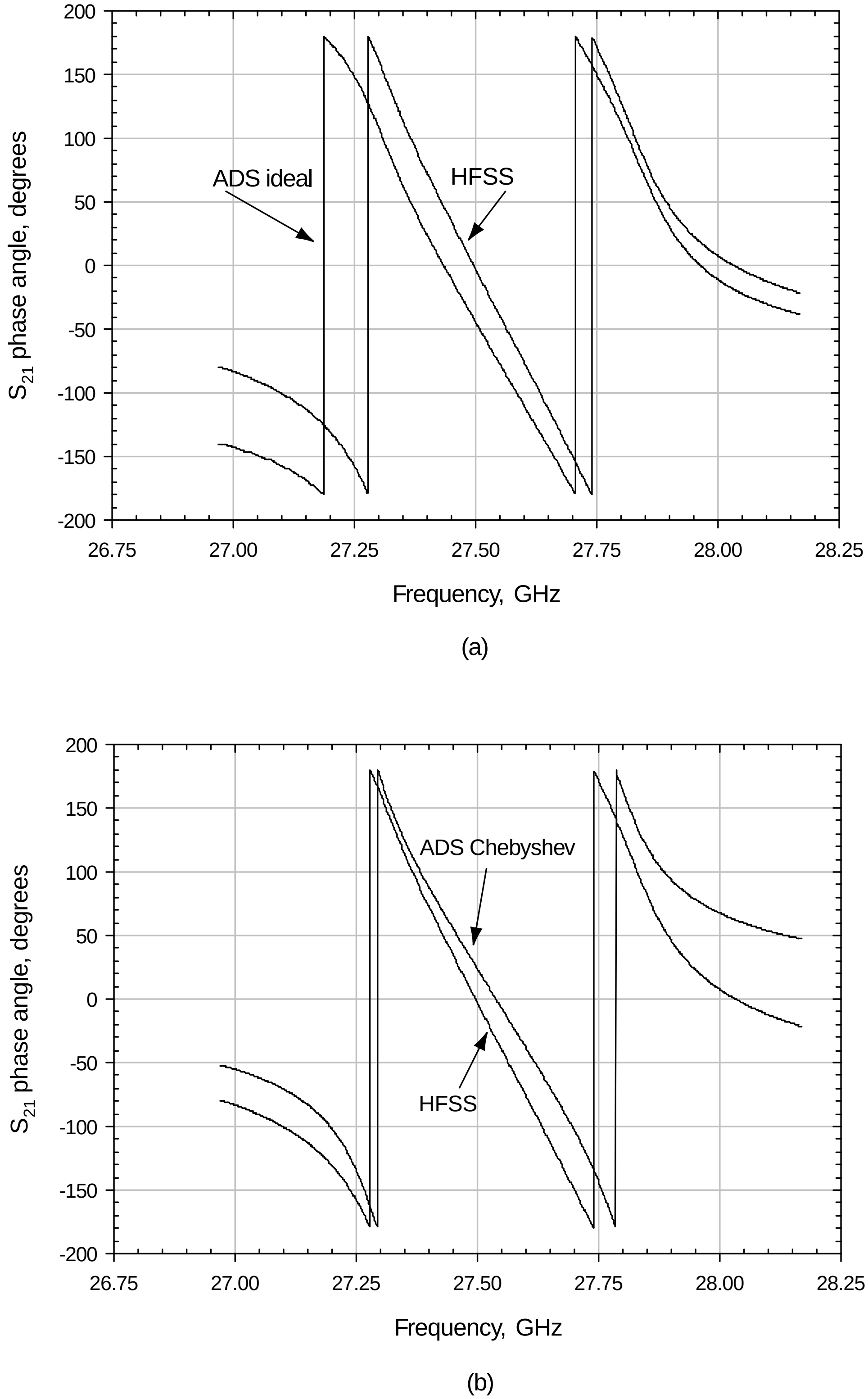

Figure 6.14: S_{21} phase comparisons, (a) final HFSS model and ideal ADS lumped element model and (b) final HFSS model and ADS 4-pole Chebyshev model.

transformed in the same manner, so that both time domain responses could be directly compared in an ADS data display window.

The HP 8722D network analyzer uses a chirp-z discrete frequency inverse transform to produce data that is similar to a time domain reflectometry measurement response to an impulse input. The chirp-z samples the z-transform along equally spaced points of a contour in the z-plane with an arbitrary starting point and an arbitrary frequency range. The sampled z-transform can be calculated specifically in the frequency range of interest, whereas the discrete Fourier transform (DFT) frequency range is dependent on the sampling frequency. The number of samples in the DFT must equal the number of points in the signal, which may require zero-padding. In contrast, no such requirement restricts the chirp-z transform. Because the chirp-z can be calculated for any arbitrary contour, including but not limited to the unit circle, poles and zeros which do not lie along the unit circle are more easily distinguished. The DFT is restricted to the unit circle in the z-plane [95, 96]. For a brief summary of the chirp-z transform derivation, see Appendix C.

The network analyzer uses a variety of modes to simulate the time domain response to impulse or step inputs. The bandpass mode is appropriate for measuring band-limited devices and simulates the time domain response to an impulse input. In order to mimic the broadband, low-pass time domain reflectometry measurement, the center frequency is transposed to DC, so that one-half the frequency span is below 0 Hz and one-half is above, and to which the inverse transform is applied [93, 97]. Adequate resolution of the circuit elements in time domain is achieved if a frequency span of two to five times the filter fractional bandwidth is used. Too wide a span and resolution will be reduced, as resolution in the time domain is inversely proportional to the span. The transmission delay of the filter is approximately bandwidth$\cdot$N/π, where N is the number of resonator elements and the bandwidth is measured in Hz (not fractional). Each filter section contributes 1/N to the delay, so the total reflection delay is approximately equal to bandwidth$\cdot 2N/\pi$, or twice the time necessary for a transmission to travel through the filter [93]. For a 4-pole, 2.2% filter at 27.57 GHz, the reflection delay is approximately 4 nanoseconds. The figure showing the ideal ADS model, Fig. 6.9, shows that this is true.

The frequency sweep of the network analyzer is centered on the center frequency of the filter passband. The ADS and HFSS models are both centered on this frequency and swept over the same frequency range. Setting the center frequency is critical as this is the frequency to which the filter will be tuned, and it must be the same in each situation.

6.4 Fabrication

The fabrication of this filter is quite similar to that presented in Chapter 5. It is fabricated using high-resistivity silicon wafers with $\epsilon_r = 11.7$. Thermally deposited SiO_2 is used as an etch mask on all wafers for TMAH etching of the small alignment cavities, after which the SiO_2 is removed. The CPW-microstrip lines are patterned on the top 400 μm wafer with an evaporated Cr/Au seed layer and are then gold electroplated to approximately 2-4 μm (+4 skin depths at 28 GHz). The top wafer slot is defined in Cr/Au using a standard lift-off process, followed by gold electroplating to approximately 2-4 μm.

Two 500 μm wafers are used to create the 1 mm high micromachined cavities. The cavities and evanescent coupling section are etched using the RIE system as described in detail in Chapter 5. The four coupling sections are etched from the front side of the top cavity wafer. Then, the four cavities are etched completely through the top cavity wafer from the back side. Finally, the cavities are completely etched through the bottom cavity wafer from the front side. When brought together, the two wafers form 1 mm high resonant cavities coupled and cross-coupled by evanescent coupling

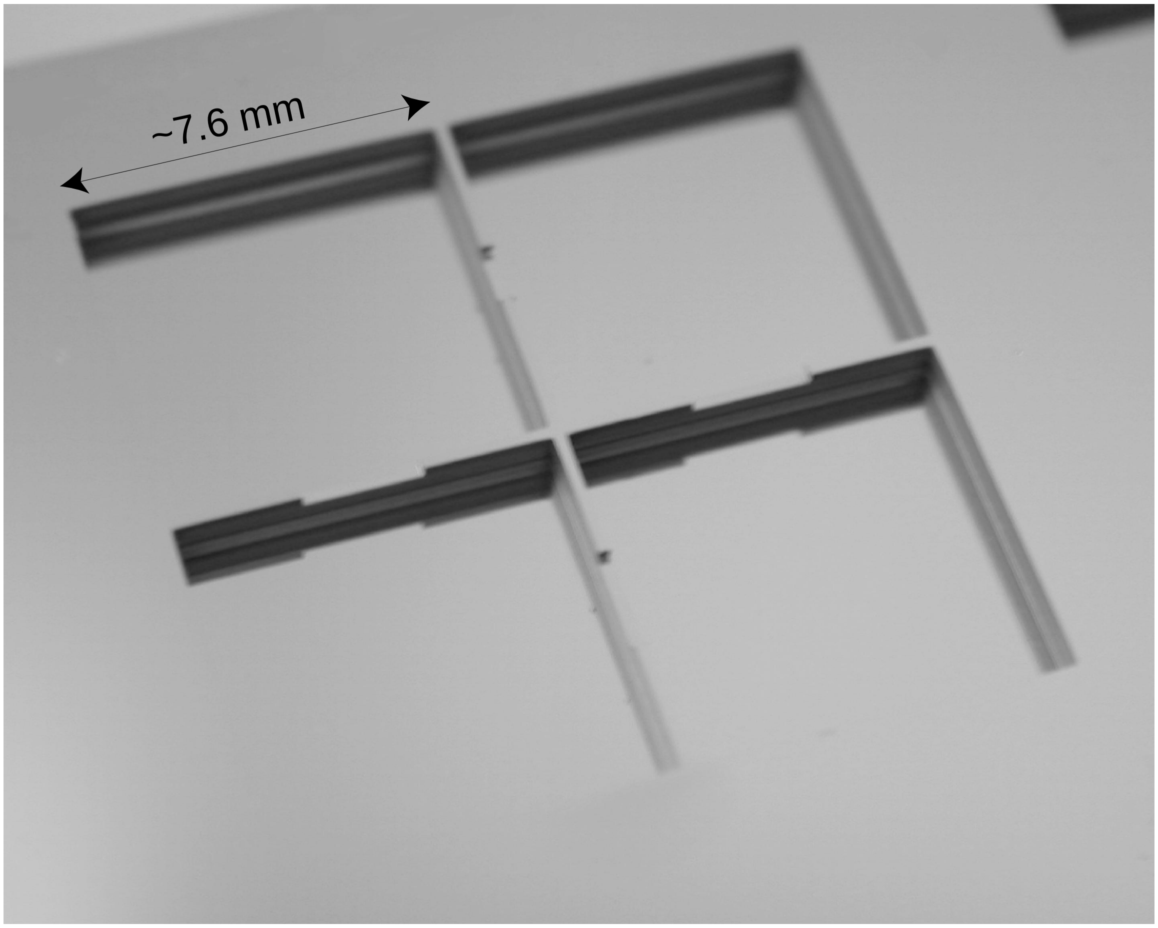

Figure 6.15: Photograph of four cavities and coupling sections after gold plating and alignment.

sections at the top of the sidewall connecting the two cavities. A photo of these aligned cavity wafers, gold plated and brought together with a gold plated bottom wafer, is shown in Fig. 6.15.

All surfaces of the etched cavity and coupling section wafers are sputter or evaporator coated with a Ti/Au seed layer, followed by gold electroplating to 2-4 μm. A 400 μm wafer, gold electroplated to 2-4 μm, serves as the bottom of the cavities. The wafers are aligned using the glass microspheres as described in Chapter 5. They are then gold-to-gold, thermal-compression bonded in the bond chamber of the EV 501 Manual Wafer Bonder at 340° C with 700 N of pressure in a vacuum [68, 69]. The overall dimensions of the finished circuit are approximately 19.5 mm long × 15.4 mm wide $\times$ 1.8 mm high as illustrated in Figs. 6.1 and 6.2.

6.5 Results and Discussion

6.5.1 RIE and Bonding Results

As seen in previous fabrications, the RIE etching process produced a degree of both mask undercut and sidewall undercut of the cavity and coupling section etched features. The photoresist mask undercut was 3 μm on average, and the reentrant profile was 15.5 μm undercut on average. Recall that the top cavity wafer was etched from the bottom up, and the bottom cavity wafer was etched from the top down. So the sidewalls of the cavities sloped out from the center, creating cavities that were approximately 37 μm wider in each direction at the top and bottom than at the center, as well as slightly larger than the mask feature. A degree of undercut was anticipated and built in to the masks; however, for a correct comparison with the measured results, the approximate alterations were incorporated into the HFSS model and a new simulation was performed.

In earlier work, the sample wafers to be processed in the RIE were mounted to a full 4 inch carrier wafer using photoresist. Unfortunately, this approach was unsuccessful during this fabrication. To protect the backside of the sample from being attacked during the etch, resist was spun and hard baked on the backside prior to the frontside lithography. A variety of deleterious conditions then developed during the RIE etch. It is most likely that these conditions were the result of trapped air bubbles between the sample and the carrier wafers, caused when the solvents in the resist used to mount the sample to the carrier dissolved into the hard baked resist on the backside of the sample. On several occasions, the sample wafer would release from the carrier and flip over during the initial pump down and helium leak check. As the chamber pumped down and the helium gas was flowed into the chamber, the carrier wafer would flex against the clamp, and the trapped air bubbles would succumb to the pressure gradient and propel the sample into the air. If the mounted sample survived the pressurization and helium leak check, the trapped air bubbles then degraded the thermal conductivity between the sample and the carrier. The sample would then overheat during the etch process, with resist etch selectivity seriously degraded as a result, yielding undesirable etching of the wafer surface. Backside etching of the sample wafer also occurred as a result of poor adhesion to the carrier. To resolve these issues, a combination of SiO_2 and a thin sputtered Ti layer was used to protect the backside during the etch, eliminating the process step of backside spinning of a protective resist layer. The existing etch mask SiO_2 was left on the wafer after the alignment cavities were etched, and Ti was then sputtered over the dielectric layer for additional protection. These layers were then removed following the RIE etch and after release from the carrier wafer. In this manner, the backsides of both of the cavity wafers were protected during the topside RIE etch processes. For the backside etch of the cavities in the top cavity wafer, a layer of sputtered Ti alone was used to protect the topside. This method proved to be quite successful, yielding smooth silicon surfaces, with very little unwanted etching, ready for metallization.

Multiple experimental bonds were performed in the EV bonder to characterize the temperature and pressure aspects after the bonder underwent repairs. Quarter-wafer pieces equal in size to those used in the filter fabrication were evaporated with Ti/Au seed layers and gold electroplated to 2.4 - 4 μm in order to simulate the filter bonding conditions. A solvent clean was performed, followed by a dehydrate bake and a UV organic clean on the test samples to improve the quality of the bonding surfaces. During several of the test bonds, the thermocouple located above the sample, but not in contact with it, indicated temperature spikes up to 34°C in excess of the setpoint temperature. In the most extreme circumstances, slight discoloring of the gold was observed. Although this was taken into consideration for the bond of the filter wafers, minor damage to the CPW-microstrip occurred in the form of darkening and some deformation. The gold of the other wafers, visible along the edges, appeared to be unaffected by the high temperatures. Therefore it is reasonable to assume that the conductivity of the cavities was not effected.

6.5.2 Transition, Q_u and Filter Measurements

A full on-wafer TRL calibration was performed on the HP8510C and multiple back-to-back through-line measurements of the CPW-microstrip transition were taken. A comparison of the measured and IE3D simulated results for a CPW-microstrip transition through-line with a 500 μm long microstrip is given in Fig. 6.16. The return loss per transition was found to be 1.25 dB at 27.6 GHz. The usable bandwidth was anticipated to be 14 to 38 GHz from the simulated model, but was found to be closer to 10 to 32 GHz, and much lossier than the model. From the various CPW-microstrip transitions modeled in IE3D for this thesis, it is reasonable to conclude that IE3D models planar structures on thinner substrates (200 μm) more accurately than those on thicker substrates (400 μm). This may be due to an underestimation of dielectric losses, which tend to dominate the total loss for microstrip lines on silicon [98, 44].

The HFSS model, with RIE undercut incorporated, exhibited 1.4 dB of insertion loss at 27.48 GHz, with a 2.2% 3 dB fractional bandwidth. The measured data with the transition loss de-embedded yields an insertion loss of 1.6 dB at 27.604 GHz and a 1.9% 3 dB fractional bandwidth. The de-embedded measured and HFSS insertion loss are compared in Fig. 6.17. The shift in resonance seen between the HFSS and measured insertion loss can be partly explained by the RIE undercut. The undercut was found to be inconsistent across the wafer, from one cavity to the next, one coupling section to the next. A precise measurement of each individual sidewall undercut could not be made given the technology available, so an average was used

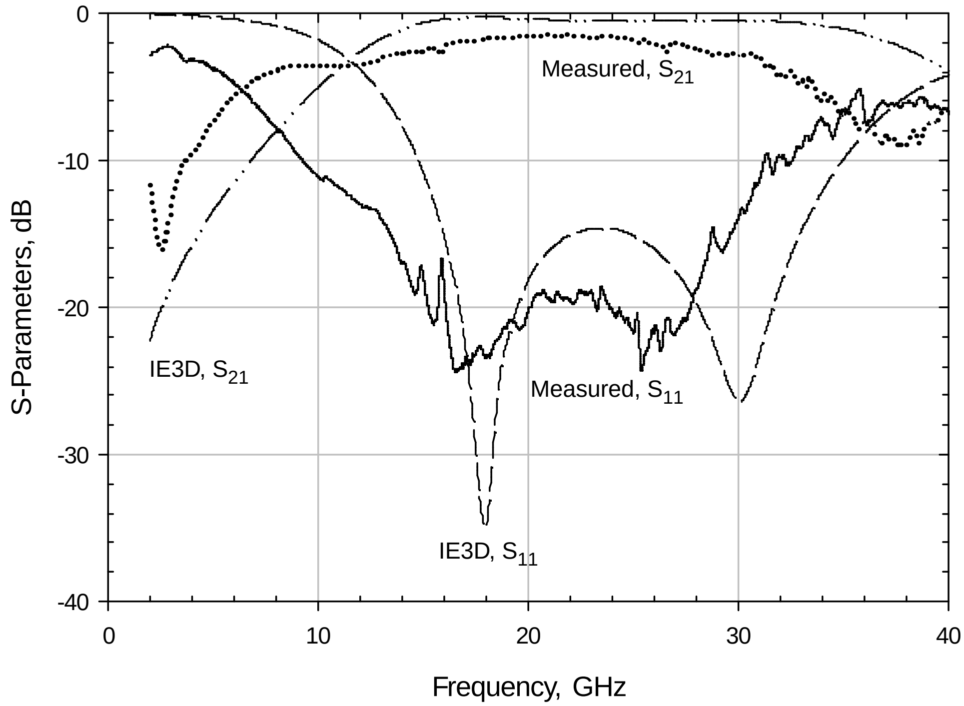

Figure 6.16: Comparison of measured and IE3D CPW-microstrip transition in back-to-back through-line configuration. Microstrip is 500 μm long.

for the entire model. A slight discrepancy in the estimated undercut would account for the resonance shift from 27.480 GHz (HFSS) to 27.604 GHz (measured), a shift of just 0.5%.

Although the HFSS model has the RIE undercut incorporated, it does not include the CPW-microstrip transition. This will account for an offset in the insertion loss phase response between the simulated and the measured data. The comparison of the measured and HFSS S_{21} phase angle is given in Fig. 6.18 with the ripple bandwidth indicated for the measured results. The measured data exhibit excellent phase linearity in the ripple passband, proving the success of the linear phase design.

HFSS simulations of a microstrip-fed, slot-coupled single cavity whose slots are 0.9 mm $\times$ 0.1 mm in dimension produced a weak coupling that yielded a resonance at 28.0375 GHz. An on-wafer, single, weakly coupled cavity was fabricated with slots of this size, measured and found to have a Q_u of 1465 resonant at 27.8838 GHz as

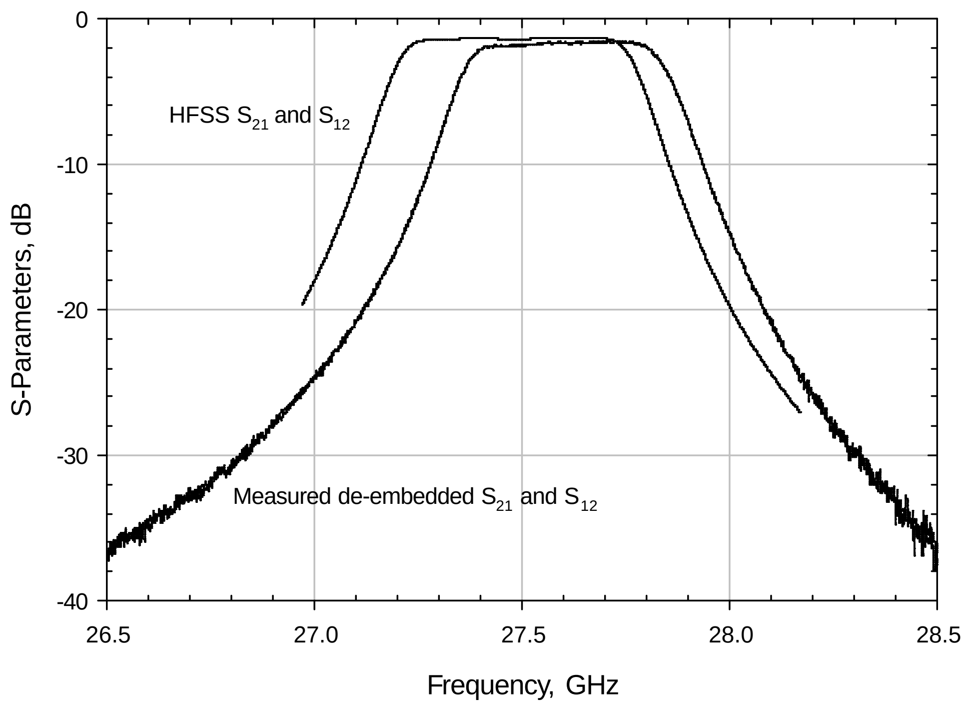

Figure 6.17: Comparison of de-embedded measured and HFSS insertion loss.

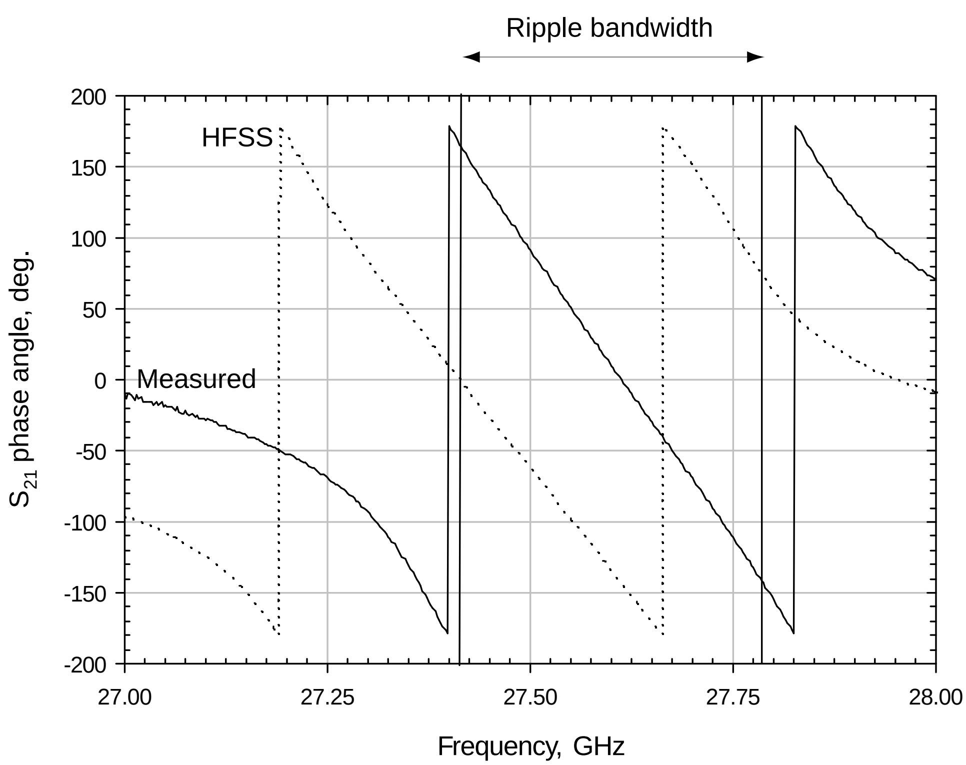

Figure 6.18: Comparison of measured and HFSS S_{21} phase response.

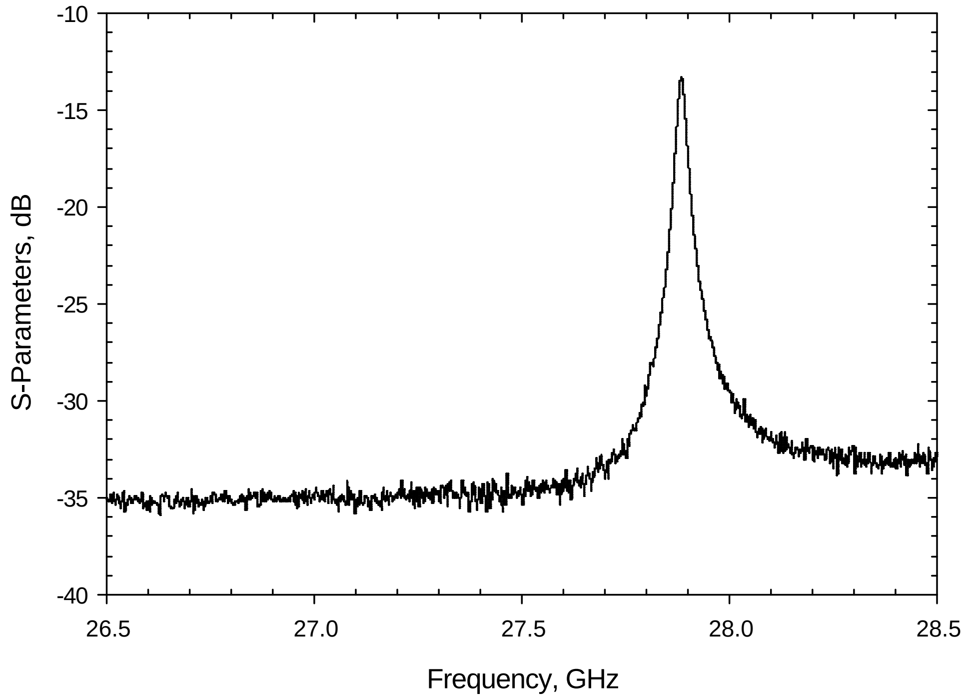

Figure 6.19: Q_u measurement from single, weakly-coupled cavity.

shown in Fig 6.19. The theoretically calculated Q_u for the TE_{101} mode for a filter with air-filled cavities of this size is 1614 from (1.3) ($\sigma_{au} = 3.9 \times 10^7$ S/m) at this frequency. The excellent value measured for the Q_u is compelling evidence that the bond is good for the filter as well, for a quality bond is one of the critical components for a high Q_u.

An earlier measurement of the filter following a failed bond attempt exhibited not only a poor filter response but also suspicious out-of-band minimums in the return loss indicative of parasitic modes or radiation. To explore this phenomenon, an IE3D model of the filter's top wafer CPW-microstrip-slot geometry was simulated. A schematic of the model and the S_{11} and S_{21} responses are shown in Fig. 6.20. Several minimums are seen in the return loss data. The minimum at 28.8 GHz of -1.7 dB has a corresponding minimum in the insertion loss data, indicating a radiation loss.

Following a full TRL calibration, the 4-pole linear phase filter was measured. The measured insertion and return loss results are shown in Fig. 6.21 for a 2 to 40 GHz

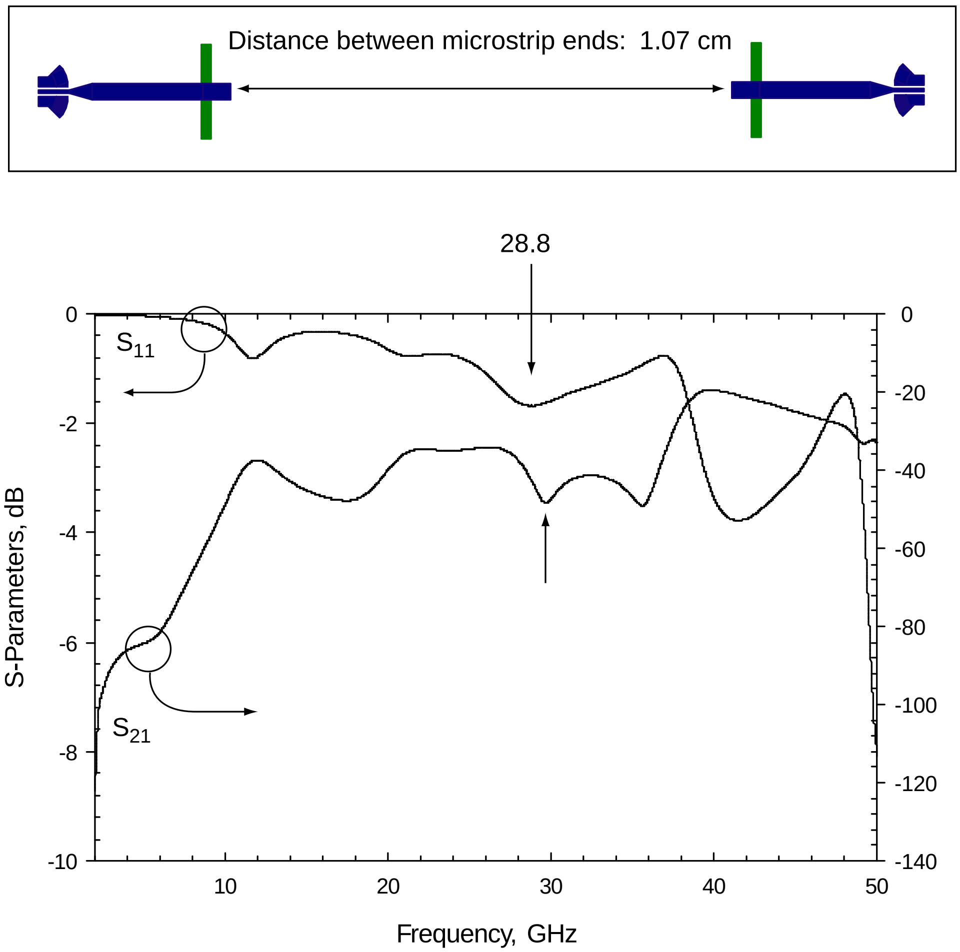

Figure 6.20: Top: IE3D model of filter top wafer. Bottom: S_{11} and S_{21} response for the model.

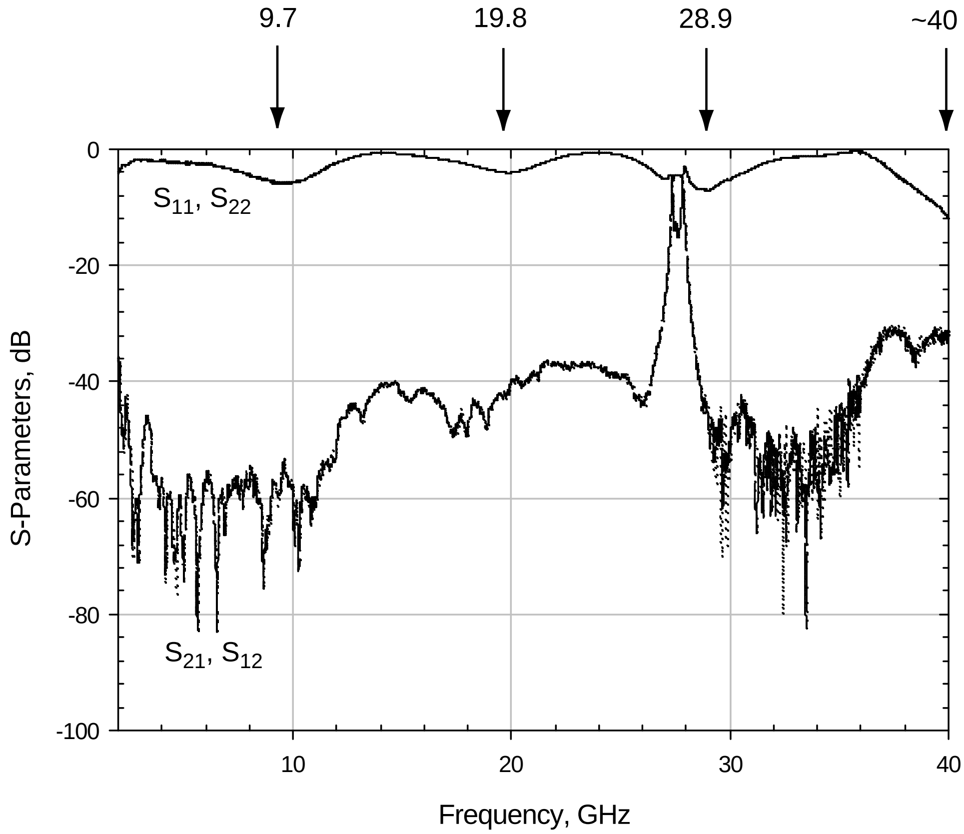

Figure 6.21: Measured results for 4-pole linear phase filter. Insertion loss minimums are indicated by the arrows.

frequency sweep. Comparison of the measured and HFSS model with RIE undercut incorporated are given in Fig. 6.22. Insertion loss minimums at 9.7, 19.8, 28.9 and 40 GHz are mimicked by the return loss and indicate radiation loss in the circuit.

To further investigate the lossy minimums in the data, several steps were taken. First, the full frequency sweep measurement from 20 to 40 GHz for the 2-pole Chebyshev filter from Chapter 5, as shown in Fig. 6.23, was re-examined. No minimums outside of the passband are seen in this data. The feeding structure geometries of the filters presented in these two chapters are very similar, refer to Figs. 6.1 and 5.1. The microstrip stub ends are 10.7 mm apart in the 4-pole linear phase design, and they are 9.5 mm apart in the 2-pole Chebyshev design. The major difference lies in the thickness of the top substrate. It is 400 μm for the linear phase filter of this chapter

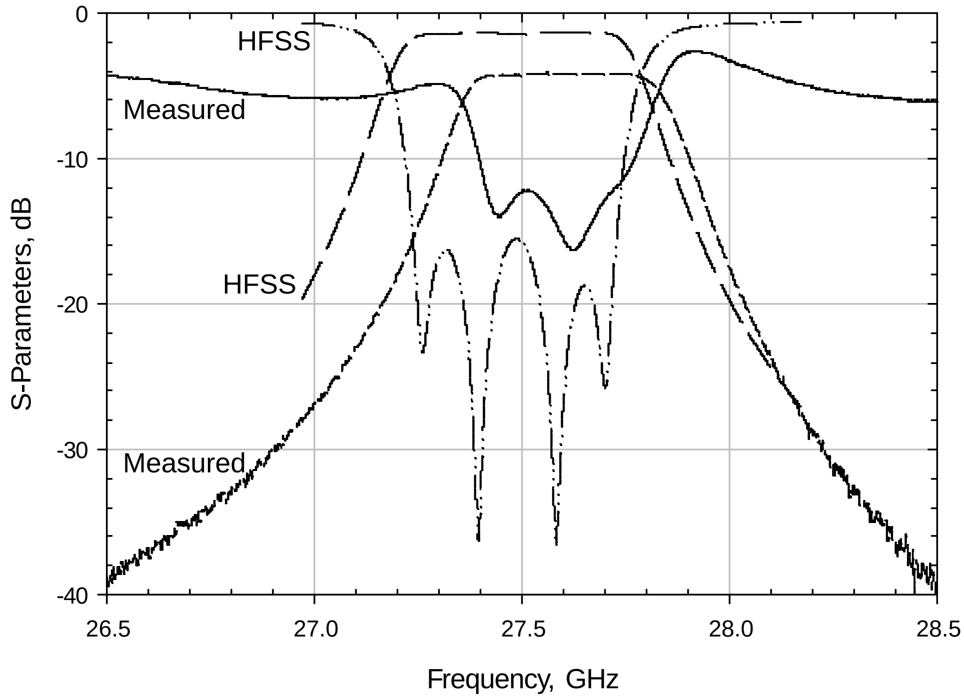

Figure 6.22: Comparison of measured and HFSS 4-pole linear phase filter.

and 200 μm for the Chebyshev filter. As has been discussed previously, substrate modes and radiation loss are more easily induced in thicker substrates by radiating structures such as the CPW ground plane radial stubs and the microstrip open end.

Secondly, a full 2 to 40 GHz measurement sweep was performed on the single cavities fabricated for the purpose of measuring the Q_u of the 4-pole linear phase filter and the 2-pole Chebyshev filter presented in the previous chapter. Comparison of the return loss for these measurements and the measurement of the linear phase filter is shown in Fig. 6.24. The single cavities are also CPW-microstrip-slot fed, although the microstrip open ends are closer together than they are for the filter. Minimums at slightly different frequencies are seen for the single cavity measurements. These correspond to radiation loss, not resonances, as indicated by the insertion loss responses which are not shown in this graph.

It is believed that substrate or radiating modes are present in the circuit and are induced from the naturally radiating structures present by the thickness of the top

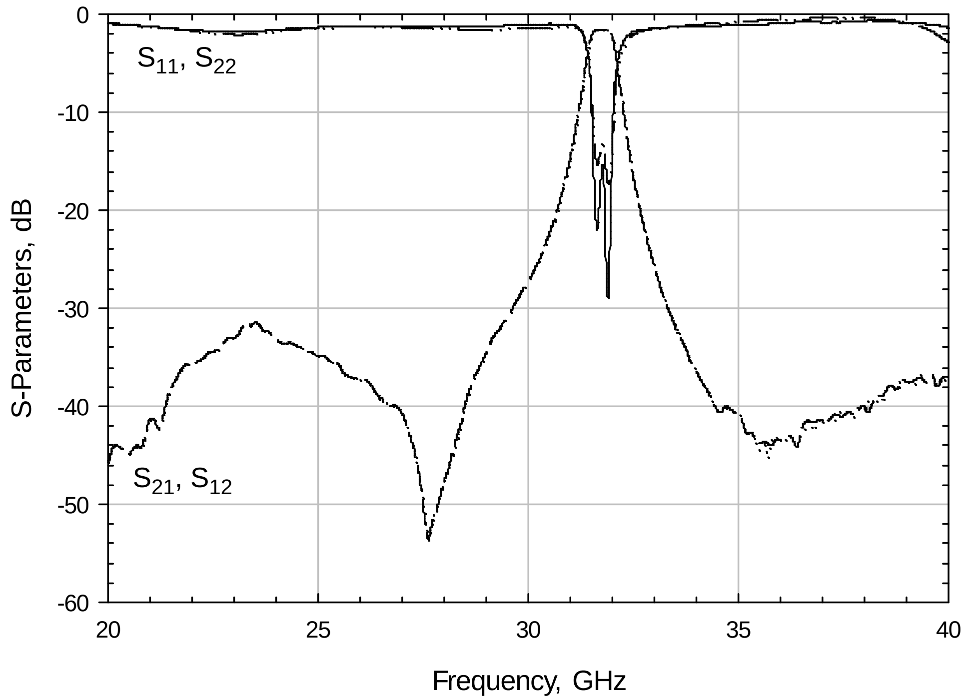

Figure 6.23: Full frequency sweep for 2-pole Chebyshev filter of Chapter 5 for comparison with Fig. 6.21. Note the absence of radiating modes.

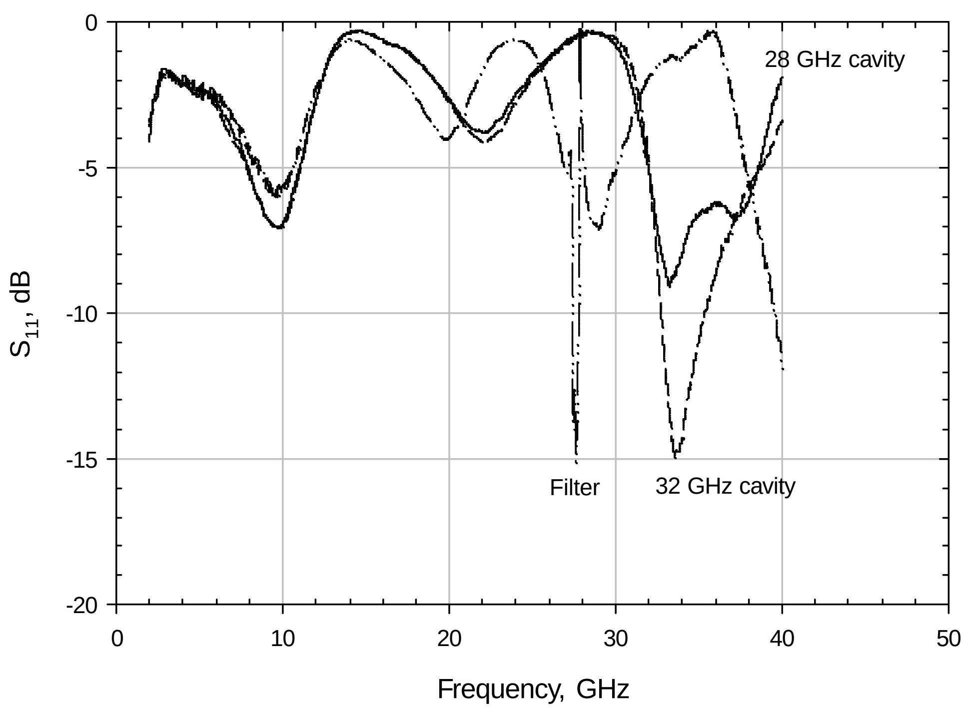

Figure 6.24: Return loss comparisons for linear phase filter and single cavities at 28 and 32 GHz.

substrate. They may be propagating and coupling between the CPW radial stubs, the microstrip open stub ends, or between the external coupling slots, although such behavior was not seen in the HFSS model. The radiating mode occurring at 28.8 GHz as seen in the IE3D model and the filter measurement is obscuring the return loss response of the measured filter. A parasitic radiation loss would reduce the energy entering the filter, and hence would reduce both the return loss and the bandwidth of the filter. If the filter had serious design or fabrication flaws however, the insertion loss curves would be degraded as well, but they are not. The time domain as illustrated in Fig. 6.25 shows a depressed external coupling compared to the ideal ADS model in both the S_{11} and S_{22} responses. In addition, the time domain plot clearly shows each resonator null and inter-cavity coupling peak. If a substantial radiation loss were occurring, the external coupling would be degraded, which it is. In spite of this deleterious effect, the time domain data confirms that the filter is working; the resonators and couplings are not obscured by the loss of energy delivered to the filter.

The external coupling in all the filters presented in this thesis was designed for the microstrip-slot feed and did not include any CPW-microstrip transition. But the inclusion of the CPW feed lines in the final circuit, whether they involve vias or radial stub transitions, does not effect the filter behavior, other than a small influence on the bandwidth. The resonance of the filter, the placement of the poles, the passband ripple level, and largely the bandwidth, are determined by the resonators and the couplings between the resonators. The external coupling serves only to impedance match the filter to the external feed line. A close match is desirable in order to deliver as much energy to the circuit load as possible, and therefore the CPW-microstrip transitions were designed to match the CPW to the microstrip with as little loss as possible. If the match between filter and external feed is poor, excess reflections occur, less energy enters the filter, and the bandwidth is slightly degraded. But the filter shape and overall performance will not be changed by an impedance mismatch

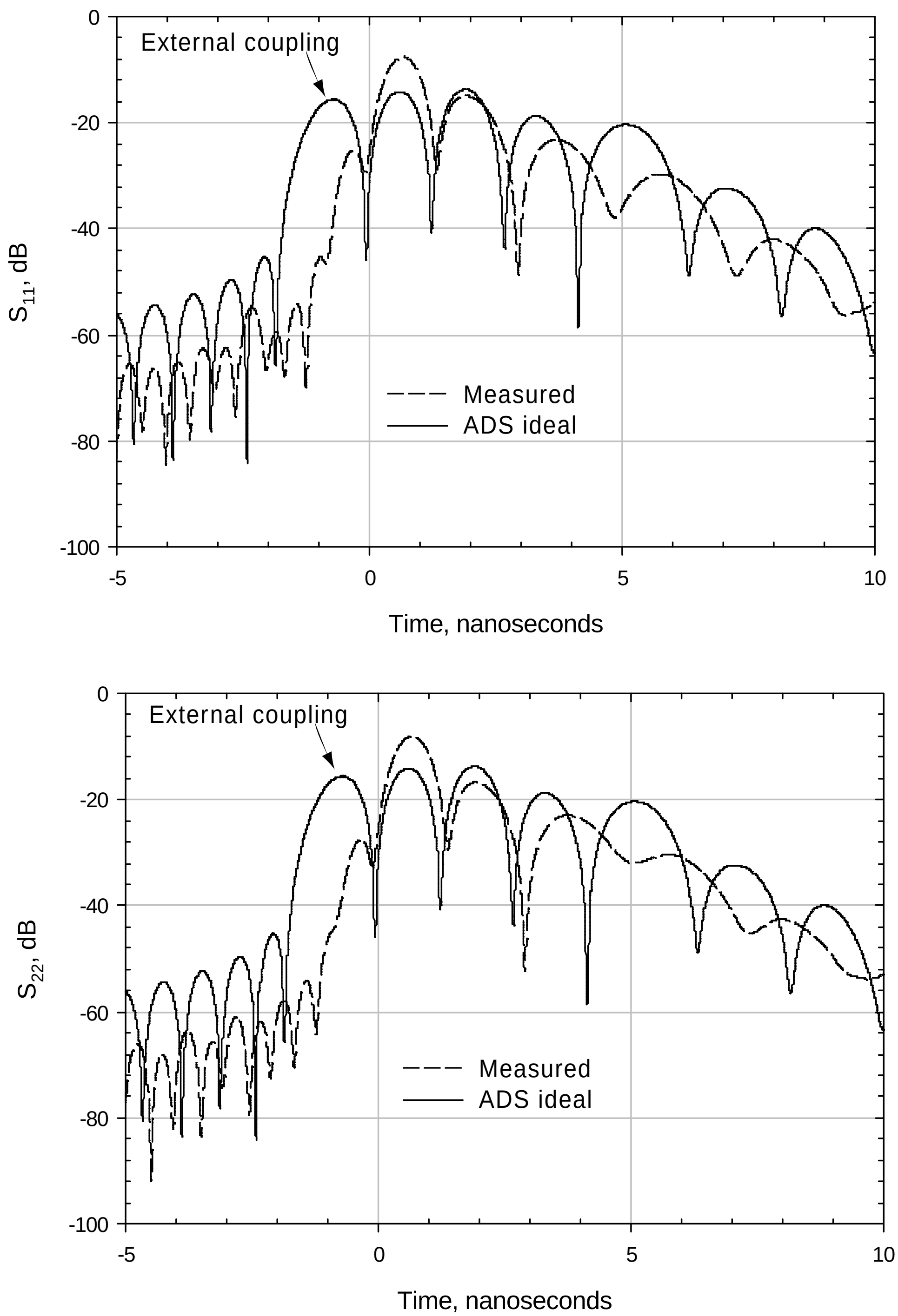

Figure 6.25: Time domain return loss responses for the measured linear phase filter compared to ADS ideal model. Top graph, S_{11}; bottom graph, S_{22}.

at the external feed.

From the performance of the transitions modeled on 400 μm substrates and the parasitic radiating behavior of the top substrate used in this filter design, it has been concluded that the use of thinner substrates is justified for the high frequency design of the planar transmission lines used to feed the cavity filters. Using thinner substrates for the top wafer would improve the CPW-microstrip transition performance, and it would reduce the instance of radiation modes [23]. However, risks include greater incidence of bond-induced breakage, difficulty in wafer handling due to increased fragility, and wafer alignment complications.

6.6 Summary

A linear phase, cross-coupled filter design and fabrication have been presented in this chapter. An improved design synthesis, utilizing time domain tuning, greatly enhances the efficiency of the design procedures discussed in earlier chapters. Although a parasitic radiation loss obscured the return loss performance, the de-embedded insertion loss was in good agreement with the HFSS model, the time domain results confirmed that the filter is working, excellent phase linearity was achieved and an excellent Q_u value of 1465 was measured.

Though the filter presented in this chapter is a linear phase design, it is hoped that the success of this work in cross-coupled cavities will justify the continued investigation of more complex filter designs, such as elliptic filters, based in semiconductor processing techniques.

CHAPTER 7

Conclusions

Nothing is as simple as it seems at first. Or as hopeless as it seems in the middle. Or as finished as it seems in the end.

Anonymous

7.1 Summary

THE motivation behind this work was to develop a high frequency filter of reduced size and weight for mobile and airborne platforms, with proven affordability and high-density integration capability for a single, monolithic communication system. Relatively inexpensive MEMS processing techniques, whose effectiveness in the fabrication of a variety of system components has been established, were to be used to develop these devices and prove their system integration and compatibility. An accurate assessment of the Q_u of these filters, and how fabrication tolerances effected it, was also required.

In response to this motivation, this thesis has demonstrated the developments of several cavity filter synthesis techniques and the micromachining fabrication processes for realizing those filters. These filters are unique, three-dimensional concepts in silicon, lightweight, compact and integrable into planar circuits. They are presented in both vertical and horizontal orientations. The vertical integration demonstrated

Table 7.1: Comparison of calculated and measured Q_u values for previous work and filters presented in this thesis.

Device	Calculated Q_u	Measured Q_u
10 GHz rectangular cavity, previous work	526	506
10 GHz 3-pole Chebyshev filter	565	-
32 GHz 2-pole Chebyshev filter	1670	1422
28 GHz 4-pole Linear Phase filter	1614	1465

the original filter application of the single, microstrip-fed, slot-coupled micromachined resonant cavity. The horizontally integrated design demonstrated design flexibility, incorporated evanescent waveguide coupling sections, and laid the foundation for cross-coupled filters. It was an improvement over the vertically integrated design in that it eliminated the need for 100 μm wafers and simplified the measurement technique. The linear phase filter design was the first application of the cross-coupled filter, and was the product of an improved time domain design and tuning approach to filter synthesis. Its success is proof of the viability of more complex, cross-coupled designs such as elliptic filters. The measured Q_u values for these filters were found to be quite promising and are summarized in Table 7.1.

7.2 Contributions

A number of unique contributions to the field have been made during the course of this work, including the following.

- A filter synthesis and design method for cavity resonators in silicon was established. Both vertical and horizontal integration designs were demonstrated. While the design of single cavity resonators is relatively simple, filter design using full-wave three-dimensional modeling and analysis is quite difficult.
- The filter synthesis method was further improved with the addition of a time domain tuning technique.

- Fabrication technologies were applied in a novel way to create multiple, direct- and cross-coupled, micromachined cavity filters in silicon that are unique in the microwave field, to the best of the author's knowledge.

Fabrication was a large part of the research presented here, and required the resolution of multiple issues. Both wet and dry anisotropic etching techniques were developed. The issues associated with the RIE etching process were resolved, including the lithographic patterning of three-dimensional features, the mounting of wafer pieces and protecting the wafer sample backside during RIE etching. Bonding difficulties were also addressed, including the demonstrated repeatability of sub-eutectic gold-to-gold bonding of multiple wafer stacks. The goal was to bond below the eutectic temperature to protect the transmission line geometries and retain gold conductivity. However, there must be just enough heat and pressure to achieve a good bond along the cavity bond joints. It would seem impossible to achieve a good bond with an operating temperature well below the melting point for gold ($> 1000°$C). But the excellent Q_u's of the 32 and 28 GHz filters attest to the high quality of the bonds. The most obvious indication of a poor bond is a severely degraded Q_u.

Some of the alignment issues were found to be less critical, even at the higher frequencies. For example, the glass spheres worked very well for the cavity wafers, which is the most important aspect of alignment. But for the 32 GHz filter, the 200 μm top wafer could not be aligned using the spheres and had to be aligned by hand under the optical microscope. As shown by the measured data, precise alignment of the external slots to the cavities was not critical to the success of the filter.

7.3 Future Work

7.3.1 On Improving the Current Methods

The filter synthesis method developed here employed a commercially available FEM code for three-dimensional modeling. This software package, HFSS, does an excellent job of modeling the cavity structures. However, its computational efficiency is significantly impaired by the addition of microstrip transmission lines, and it proved to be quite incapable of modeling CPW-to-microstrip transitions accurately. A numerical code tailored for the accurate and efficient analysis of hybrid planar and three-dimensional structures would be a welcome asset, and could be a future dissertation topic.

Although many of the fabrication issues were resolved to some degree, there is room for improvement. Further investigation of the RIE etching techniques is warranted, including simplified sample mounting techniques, the use of oxide or nitride "hard" etch masks for reduced mask undercut, and altering the RIE recipe parameters such as power, process times and etch chemistry in order to improve the vertical profile. Evaluation of bond quality as a function of pre-bond cleaning, bond pressure, temperature and ambient atmosphere could be accomplished by an SEM examination of the bond joints of diced, bonded samples. The investigation of simplified, via-less CPW-to-microstrip transitions on thicker substrates with improved insertion loss performance and reduced parasitic modes would have practical results for a variety of circuit applications, in addition to those presented here. Also, system fabrication integration should be examined. Each component of the system requires certain fabrication processes, which will impact the neighboring components. Fabrication compatibility will certainly influence the viability of such a system.

Finally, an evaluation of the integrated system performance would be instructive. To reiterate, full size waveguide filters have very high Q_u's, but require waveguide feeds or cable feeds, which by themselves are lossy and not easily integrated with on-wafer amplifiers and MEMS switches. As components, the filters demonstrated here are unique and high-Q_u for their size. However, it remains to be verified how these filters would actually perform in a "system-on-a-chip" transmit/receive system. The reduction in overall system weight and volume, and the reduced loss due to the elimination of waveguide or cable connections may very well justify the use of micromachined filters.

7.3.2 Elliptic Filters

Elliptic filters are based on the Cauer-Darlington (elliptic) functions which have equal ripple in both the pass and stopbands. Waveguide demonstrations of elliptic filters have been demonstrated as far back as 1970 in [87]. Elliptic filters allow specification of minimal transmission attenuation in the passband as well as maximum attenuation in the stopband, at the expense of linear phase. However, filters with both real frequency transmission zeros and a linear phase response are possible. The freedom to specify stopband attenuation yields improved cut-off rates and isolation between filter channels [99]. The success of the cross-coupled linear phase filter presented here means that an elliptic filter design is possible. The fabrication approach to the elliptic filter would be very similar to that taken for the linear phase filter; such a filter is probably realizable as well.

7.3.3 Dielectric Resonators

Resonant cavities loaded with dielectrics have been in use since the early 1960's [88, 100]. Dielectric bodies with air boundaries will resonate, with the fields concentrated in the dielectric if the relative permittivity is high. By placing the dielectric material inside a metal waveguide below cutoff, radiation losses are minimized. The total Q_u of a dielectrically loaded cavity with lossy conducting walls is dependent upon unloaded Q's due to dielectric and conductor losses as given by (3.13). If the waveguide dimensions are about twice the largest dimension of the dielectric, the metal waveguide will not degrade the Q_u, which will be entirely dependent on Q_d, or $Q_u = Q_d = 1/\tan\delta$. Otherwise, the Q_c due to the conducting cavity walls will also influence the total Q_u. For example, if the 32 GHz filter presented in Chapter 4 were loaded with a ceramic dielectric material of $\epsilon_r = 100$ and a loss tangent of 0.0001, the cavity dimensions could be reduced by an order of magnitude, from 6.6 mm square to 0.66 mm square, and the total Q_u would increase, theoretically, to about 3500. Even with a contribution due to Q_c, this is a significant improvement in Q_u and size reduction. Size and weight reduction is of course important for space-borne applications, as well as other communication applications where miniaturization is a factor. Dielectric loading could improve the performance of a cross-coupled linear phase or elliptic function filter as well.

Low-Temperature Cofired Ceramics (LTCC) is a promising technology currently used to manufacture RF circuits. LTCC is a multilayer glass ceramic composite material that combines the ceramics with high conductivity metals in three-dimensional circuits. Digital, analog, RF, and microwave components are all interconnected and integrated into the package. LTCC's come in a wide range of dielectric constants, from as low as 3.8 up to 20,000. The reduced weight, low loss and high circuit density characteristics make it an attractive alternative for many integrated applications. Its thermal stability make it a possible candidate for use in dielectrically loaded cavity filter design [101, 102]. A recent three-dimensional LTCC filter embedded in GaAs MESFET-based MMIC front-end module demonstrates the feasibility of using LTCC for wireless application filter design [103].

It ain't over 'til it's over.
Yogi Bera

APPENDICES

Appendix A

STS Deep Reactive Ion Etching Process Parameters

A.1 Introduction

A typical "Thru Wafer" etch recipe was used for all of the RIE etching as described in this thesis. The user has the freedom to define total process time, which is dependent on the depth of material to be etched, the etch step time, the passivation step time, and the coil and platten generator powers. The original recipe used here called for 13/7 seconds of etch/passivation and 250 W platten power. This recipe was altered to 12/8 seconds of etch/passivation and 225 W platten power in an effort to reduce the reentrant profile, as discussed in the thesis. The etch time varied from 2.3 to 5 μm/minute, depending on the amount of exposed silicon and the temperature of the chamber.

A.2 RIE Process Parameters

1. Stand-by steps:
   (a) Pump down time: 20 seconds

   (b) Purge time: 10 seconds
   (c) Pump out time: 30 seconds
   (d) Helium leak-up rate test: Test time: 1 minute
   (e) Maximum leak rate: 10 mT/min

2. Etch process steps:
   (a) Pump down time: 20 seconds
   (b) Gas stabilization time: 30 seconds
   (c) Process time: defined by user
   (d) Pumpout time: 30 seconds
   (e) Order of etching: passivation first
   (f) Etch time: 13 or 12 seconds
   (g) Passivation time: 7 or 8 seconds
   (h) APC Mode: Manual
   (i) APC setting: 67%
   (j) Base pressure: 0.2 mT
   (k) Pressure trip: 94 mT
   (l) C_4F_8: flow = 85 sscm, tolerance = 50%
   (m) SF_6: flow = 160 sscm, tolerance = 50%
   (n) O_2: flow = 0 sscm, tolerance = 5%
   (o) Ar: flow = 0 sscm, tolerance = 5%
   (p) RF etch power: 250 W
   (q) Matching: auto, match load = 50%, match tune = 50%
   (r) Coil generator: etch = 800 W, passivation = 600 W, tolerance = 50%
   (s) Platten generator: etch = 250 or 225 W, passivation = 0 W, tolerance = 50%

Appendix B

Fabrication Processes

The processing fabrication steps for the filters described in this thesis are provided in this appendix. In section B.1, wafer cleaning is presented. Thermal oxidation processing is presented in section B.2. Photoresist processing is presented in section B.3, mounting of thinned wafers in section B.4 and wet chemical etching in section B.5. Transmission line printing and wafer metallization is discussed in section B.6.

B.1 Wafer Cleaning

1. Organic "piranha" clean: Used to remove stubborn organic residues and some metals.
   (a) Pour a 1:1 mixture of hydrogen peroxide and sulfuric acid, being sure to add the acid to the peroxide.
   (b) Place sample in the solution for 10 minutes.
   (c) Rinse in deionized water (DI) for several minutes.
2. Solvent clean: Used at the start of every new wafer process and in between processing steps.
   (a) Place sample in acetone for 2-3 minutes.
   (b) Remove and place sample in isopropyl alcohol (IPA) for 2-3 minutes.

(c) Dry sample using the N_2 gun.

(d) Dehydrate bake sample on 130° hotplate for at least 3 minutes.

B.2 Silicon Dioxide Furnace Processing Steps

1. Pre-furnace Clean

   (a) Wear full personal protective equipment: goggles, apron, faceshield, sleeves and trionic gloves.

   (b) Do not allow the bottles or bottle caps to touch the inside of the bench, and do not touch the bench without wearing the trionic gloves.

   (c) Run DI hose into quench tank for 30 seconds to clean the hose.

   (d) Fill organic and ionic clean tanks with DI to just cover the end of the N_2 hose.

   (e) Turn on the heaters set to 95°C.

   (f) Load wafers into teflon carrier (maximum 25 wafers) using tweezers.

   (g) Load 200 μm and 100 μm wafers in every other slot.

   (h) Using top load handle, place carrier wafer into the quench tank and turn it on to rinse wafers while other preparations are completed.

   (i) Organic Clean

      i. When temperature of the organic clean tank reaches 92°C, add organic clean chemicals.

      ii. Add 1 liter of hydrogen peroxide to the tank, followed by 1 liter of ammonium hydroxide.

      iii. Immerse wafers in the tank for 10 minutes, removing carrier handle and placing it in the quench tank during this time.

      iv. Remove wafer carrier from the organic clean tank, and rinse wafers for 2 minutes in the quench tank, removing the handle and placing it beside the wafer carrier.

v. Turn off the organic tank heater.

(j) HF Dip: Removes native oxide

i. Place wafers in hydrofluoric solution (10:1 with DI) for 30 seconds. Do not remove the handle.

ii. Rinse for 2 minutes in the quench tank, removing the handle and placing it in the quench tank beside the carrier.

(k) Ionic Clean

i. Add 1 liter of hydrogen peroxide, followed by 1 liter of hydrochloric acid.

ii. Immerse wafers in the tank for 10 minutes, removing the carrier handle and placing it in the quench tank during this time.

iii. Both the ionic and organic solutions will begin to etch silicon after 20 minutes, so be sure to remove the wafers well before this time.

iv. Remove wafer carrier from the ionic clean tank.

v. Turn off the ionic tank heater.

(l) Final Rinsing

i. Rinse wafers for 5 minutes in the downstream cascade tank, removing the carrier handle and placing it beside the wafer carrier.

ii. Rinse wafers in upstream cascade tank, removing the handle and placing it in the downstream tank.

iii. Make sure that the carrier is placed so that the water flows parallel to the wafers in both tanks.

iv. Make sure that the handle is perpendicular to the water flow, or it may slip underwater.

v. After resistivity has approached as close as possible to 15 MΩ-cm on the resistivity meter, place carrier wafer into the spin drier using both the top and side load handles.

vi. Cycle the spin drier.

vii. Once the cycle has completed successfully, (resitivity $> 14.2M\Omega - cm$) the wafers are ready to be loaded into the furnace.

(m) Furnace Loading

i. Load the wafers into the furnace with the vacuum wand only.

ii. Never touch the cleaned wafers with tweezers.

(n) Clean Up

i. Aspirate and rinse the beakers three times.

ii. Aspirate and clean the tanks twice each.

iii. Do not aspirate the chemicals in sequence. Aspirate and rinse, then aspirate the rinse water before moving between tanks/beakers. Otherwise, chemicals can be transferred from one tank/beaker to the next by the aspirator hose.

1. Wet/Dry/Wet Thermal Silicon Dioxide Recipe

(a) Parameter table: DWDSKIN

(b) Recipe name: DWD/TCA

(c) Upgas/A: N2-3

(d) Temp/A: 800

(e) Temrmp: MAX

(f) Dry/A: 1 hour

(g) Upgas/B: N2-3

(h) Temp/B: 1100

(i) Settime: 10 minutes

(j) Dry1: 5 minutes

(k) Wet: 0

(l) Wet/TCA: dependent on desired oxide thickness

(m) Dry2: 5 minutes

(n) N2 anneal: 10 minutes

(o) Downgas: N2-3

(p) PULL-600: 200

(q) Settle: SPKSET

(r) Lowset: -2

(s) Highset: +2

(t) LoN2flo: MAX

(u) Rampdown: MAX

(v) Boatspd: 20

B.3 Photoresist Process Steps

1. Shipley SC1827: General purpose positive resist.

   (a) Solvent clean wafers.

   (b) Spin adhesion promoter HMDS for 30 seconds, same speed as resist spin.

   (c) Spin 1827 resist for 30 seconds:

      i. @ 4k rpm for 2.7 μm thickness.

      ii. @ 3.5k rpm for 3 μm thickness.

      iii. @ 3k rpm for 3.3 μm thickness.

   (d) Soft bake on hotplate at 105°C for 2 minutes.

   (e) Align and UV expose for 12 seconds.

   (f) Develop in Shipley 351:DI, 1:5 for 40 seconds.

   (g) Hard bake on hotplate at 130°C for 1 minute.

2. AZ 5214-E: Used for image reversal necessary for metal lift-off process.

   (a) Solvent clean wafers.

   (b) Spin adhesion promoter HMDS for 30 seconds, same speed as resist spin.

(c) Spin 5214 resist for 30 seconds @ 2.5k rpm for 1.7 μm thickness.

(d) Soft bake on hotplate at 105°C for 2 minutes.

(e) Align and UV expose for 4.5 seconds.

(f) Hard bake on hotplate at 130°C for 1 minute.

(g) Flood UV expose using clear mask.

(h) Develop in AZ 327 for 40 seconds.

3. AZ 9260: Used for RIE etch mask and mounting.

    (a) Solvent clean wafers.

    (b) Spin adhesion promoter HMDS for 30 seconds, same speed as resist spin.

    (c) Spin 9260 resist for 5 seconds"spread", followed by 30 seconds:

        i. @ 4k rpm for 7 μm thickness.

        ii. @ 2k rpm for 10 μm thickness.

    (d) For spin speeds $\leq$2k rpm, rest wafer horizontally for 20 minutes in closed wafer carrier (retains solvents).

    (e) Soft bake on hotplate at 110°C for:

        i. 2.5 minutes if spun at 4k rpm.

        ii. 4.5 minutes if spun at 2k rpm.

    (f) Rest wafer horizontally for 20 minutes.

    (g) Align and UV expose for:

        i. 45 seconds if spun at 4k rpm.

        ii. 120 seconds if spun at 2k rpm.

    (h) Develop in AZ 400k:DI, 1:3 for 1-2 minutes.

    (i) Mount on carrier wafer:

        i. Spin 4 inch wafer with HMDS, 9260 at desired speed for desired thickness.

        ii. Mount sample wafer, tapping lightly to seat sample in wet resist.

        iii. Hard bake in oven for:

A. 30 minutes at 90°C to outgas mounting resist.

B. Then reset oven temperature and bake for 45 minutes at 110°C.

B.4 Wafer Handling

1. Thin Wafer Mounting: Used to mount 100 μm and 200 μm wafers for ease of handling.
   (a) If using a glass slide, scribe it so that it will fit on the wafer carriers used in the thin film machines.
   (b) Clean glass slide or carrier wafer piece by solvent cleaning process.
   (c) Spin carrier with 1827 resist at 2k rpm as described above.
   (d) Mount thin wafer sample. Tap down lightly around edges.
   (e) Softbake on hotplate at 80° for 2 minutes to outgas solvent and air bubbles between sample and carrier.
   (f) Hardbake on hotplate at 130° for 2 minutes.

B.5 Wet Anisotropic Etching

1. TMAH Etching: Used to etch vias to connect CPW and microstrip ground planes, cavities presented in Chapter 4, alignment cavities for glass microsphere alignment as presented in Chapters 5 and 6. Etching performed in EECS 3440 laboratory.
   (a) Wafer Preparation
      i. Pattern features on oxide wafer by using 1827 resist as described above.
      ii. Etch oxide from features using buffered hydroflouric acid (BHF).
      iii. Remove resist in heated PRS.

iv. Rinse wafer in DI quench tank for at least 10 minutes.

v. Dip wafer in BHF for 30 seconds to remove any native oxide.

vi. Rinse but do not dry wafer.

vii. Place wafer in DI in covered container to slow native oxide growth while transporting to fabrication lab.

(b) TMAH Etch

i. Heat 25wt.% TMAH to 85°C in large glass beaker on hotplate using temperature immersion probe.

ii. Immerse wafer in solution and cover. Etch rates are typically 27 to 36 μm/hour, depending on feature size, number of samples and volume of TMAH used.

iii. After etch has completed, remove wafer, rinse and dry with N_2 gun..

iv. If etch is not finished, solution may be held idle at 65°C, where it will not fume or break down. Once the TMAH solution has cooled to room temperature, it will no longer etch silicon.

2. KOH Etching: Used to etch vias to connect CPW and microstrip ground planes, slots in 100 μm wafers as presented in Chapter 4. Etching performed in EECS 3440 laboratory.

(a) Wafer Preparation: identical to that presented for TMAH etching above.

(b) KOH Etch

i. Slowly add 300 g KOH pellets to 600 mL of DI in large glass beaker on a hotplate with temperature immersion probe.

ii. Agitate solution.

iii. Process is exothermic. Wait for temperature to stabilize, then turn on the hotplate and heat to 65°C.

iv. Immerse wafers in solution and cover. Etch rates are typically 30μm/hour, depending on feature size and number of samples.

v. After etch has completed, remove wafer, rinse and dry with N_2 gun.

B.6 Transmission Line Definition and Wafer Metallization

1. Gold Plating: Performed in EECS 3440 laboratory.
   (a) Fill glass beaker with Orotemp-24 gold plating solution sufficient to cover sample.
   (b) Agitate solution, heat to 55°C with temperature immersion probe.
   (c) Remove teflon cathode holder, rinse in first rinse beaker.
   (d) Mount sample on teflon cathode holder.
   (e) Replace teflon cathode holder, adjusting sample immersion level in the solution.
   (f) Attach leads to cathode and anode.
   (g) Turn on power source and meter. Select DC current and "auto".
   (h) Adjust power source until meter reads current as desired per plating area and plating time.
   (i) After plating, rinse teflon cathode holder with sample still attached. Remove sample and dry with N_2 gun.
2. CPW-Microstrip Definition
   (a) Deposit seed layer by evaporating Ti/Au/Ti, 500/1000/500 $\AA$.
   (b) Pattern transmission lines by using 1827 resist as described above.
   (c) Etch top Ti layer in HF:DI, 1:10. Rinse.
   (d) Gold plate to desired thickness using process described above.
   (e) Remove resist in acetone or heated photoresist strip (PRS).
   (f) Rinse acetone-soaked wafer in IPA, rinse PRS-soaked wafer in DI quench tank for at least 10 minutes.

(g) Dry with N_2 gun.

(h) Etch top Ti layer. Rinse and dry.

(i) Etch Au in gold etchant. Rinse and dry.

(j) Etch bottom Ti layer. Rinse and dry.

3. Alignment Marks, Slot/Ground Plane Definition by Lift-Off Process

(a) Pattern features by using 5214 resist as described above.

(b) Evaporate Ti/Au, 500/2000 $\mathring{A}$, over resist layer.

(c) Lift-off unwanted metallization using acetone or heated PRS.

(d) Rinse acetone-soake wafer in IPA, rinse PRS-soaked wafer in DI quench tank for at least 10 minutes.

(e) Dry with N_2 gun.

(f) If slot/ground plane, gold plate to desired thickness.

4. Slot/Ground Plane Definition by Etching Process

(a) Deposit seed layer by evaporating Ti/Au, 500/1000 $\mathring{A}$.

(b) Pattern slot by using 1827 resist as described above.

(c) Etch slot: Au in gold etchant, Ti in HF:DI, 1:10.

(d) Remove resist in acetone or heated PRS.

(e) Rinse acetone-soake wafer in IPA, rinse PRS-soaked wafer in DI quench tank for at least 10 minutes.

(f) Dry with N_2 gun.

(g) Gold plate to desired thickness.

5. Metallizing Cavity and Thin Slot Wafers

(a) Flood sputter seed layer on both sides for best step coverage of cavity sidewalls, Ti/Au, 500/2000 $\mathring{A}$.

(b) Flood evaporate seed layer on both sides of thin slot wafers, Ti/Au, 500/2000 $\mathring{A}$.

(c) Gold plate to desired thickness.

Appendix C

The Z- and Chirp-Z Transforms

This appendix provides a brief summary of the z-transform as the basis for the chirp-z transform. Whereas the Laplace transform reduces constant coefficient linear differential equations to linear algebraic equations, the z-transform reduces constant coefficient linear difference equations to linear algebraic equations. It aids the analysis of discrete time signals as the Laplace does for continuous time signals.

Given a continuous function $f(t)$ and its sampled output $f_s(t)$ sampled every T seconds, $f_s(t)$ can be given as

$$\begin{aligned} f_s(t) &= f(t)d(t) \\ &= T\sum_{n=0}^{\infty} f(nT)\delta(t-nT) \end{aligned} \tag{C.1}$$

where $d(t)$ is a periodic impulse train function of impulses spaced T apart and $\delta(t-nT)$ is the Dirac delta function occurring at $t = nT$, see Fig. C.1. Taking the Laplace transform of both sides yields

$$F_s(s) = \sum_{n=0}^{\infty} f(nT)e^{-nTs} \tag{C.2}$$

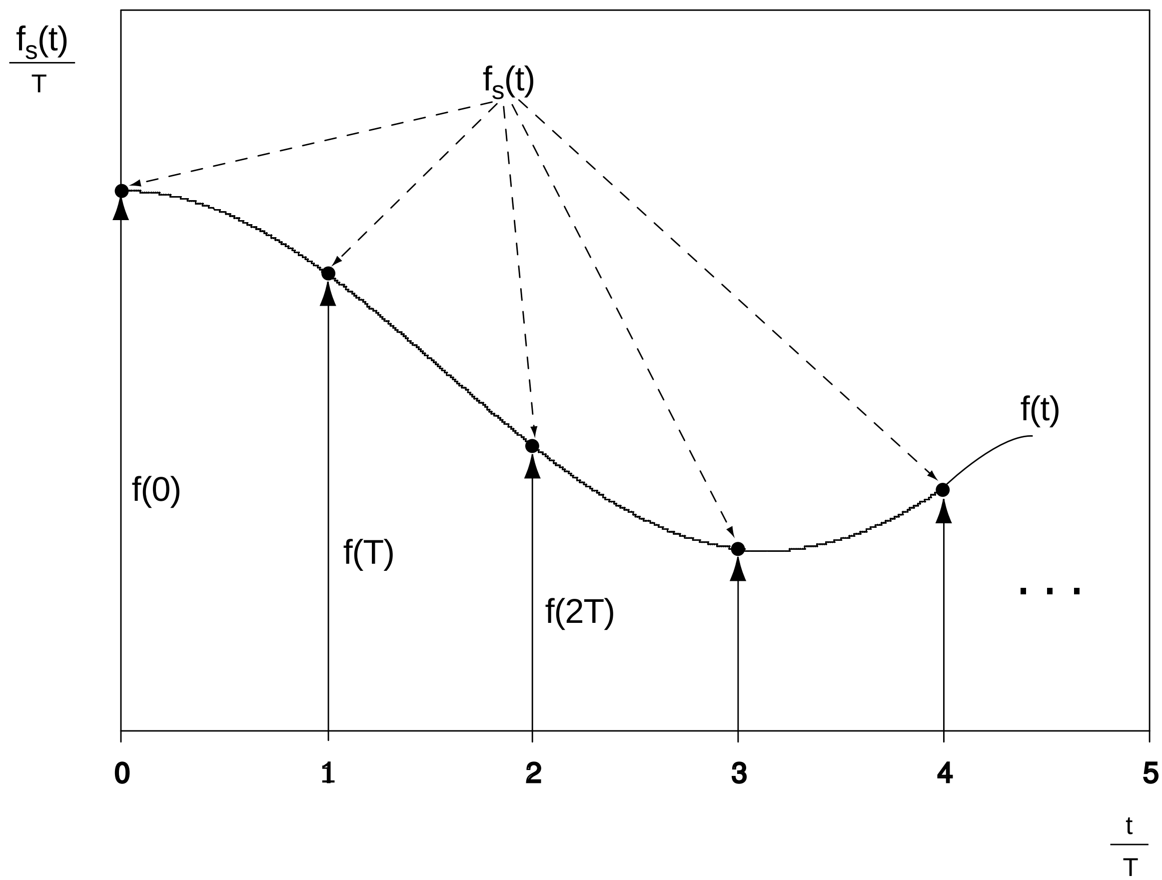

Figure C.1: Sampled function $f_s(t)$.

where the T coefficient is suppressed. The substitution of $z = e^{sT}$ yields

$$\mathcal{Z}[f_s(t)] = F(z) = F_s(s)|_{s=\frac{1}{T}ln(z)} = \sum_{n=0}^{\infty} f(nT)z^{-n} \tag{C.3}$$

an algebraic expression in z, where $F(z)$ is the z-transform of $f_s(t)$. The summation can be restricted, without loss of generality, to samplings consisting of N finite points,

$$F(z) = \sum_{n=0}^{N-1} f(nT)z^{-n} \tag{C.4}$$

Performing the Laplace transform on the impulse train along a straight line in the complex frequency s-plane corresponds to performing the z-transform of the sequence along a contour in the complex frequency z-plane. The s-plane maps into the z-plane in the following manner.

- Points on the $j\omega$ axis map to points on the unit circle in the z-plane, as

$$z = e^{st} = e^{jwt} \tag{C.5}$$

has unity magnitude and phase angle ωT.

- Points in the left-hand plane, where $s = -\alpha + j\beta \quad (\alpha > 0)$, map to points inside the unit circle in the z-plane, as

$$z = e^{(-\alpha + j\beta)T} = e^{-\alpha T} e^{j\beta T} \tag{C.6}$$

has a magnitude less than unity.

- Points in the right-hand plane map to points outside the unit circle in the z-plane, as

$$z = e^{(\alpha + j\beta)T} = e^{\alpha T} e^{j\beta T} \tag{C.7}$$

has a magnitude greater than unity.

Poles in the z-plane have the following characteristics. On the unit circle, they correspond to oscillating sampled time functions, except for poles at $z = 1$, which correspond to constant or increasing functions. Inside the unit circle, they correspond to sampled time functions that decrease exponentially with increasing time. Outside the unit circle, they correspond to sampled time functions that increase exponentially with time. This is important when considering passive filters. The transmission poles and zeroes of the filter transfer function are the complex frequencies where the function is infinite and zero, respectively. The poles are the natural frequencies of the system. In the pole-zero diagram, all transmission poles (attenuation zeros) must lie in the left half of the complex plane or on the $j\omega$ axis. Otherwise, the resonances would increase exponentially in magnitude and energy, which cannot occur in a passive resonant circuit [63, 96, 104].

Computing the z-transform at a discrete set of points z_k produces evenly spaced points along the chosen contour in the z-plane. The N-point DFT of the sequence is evaluated at each point along the contour, designated by the subscript k. In light of this, equation C.4 becomes

$$F(z_k) = \sum_{n=0}^{N-1} f(nT) z_k^{-n} \tag{C.8}$$

A general contour can be chosen by writing z_k as

$$\begin{aligned} z_k &= AW^{-k}, \quad \text{where} \quad k = 0, 1 \ldots M-1 \\ A &= A_o e^{j2\pi\theta_o} \\ W &= W_o e^{j2\pi\phi_o} \end{aligned} \tag{C.9}$$

For the case of $A = 1$, $M = N$ and $W = e^{-j2\pi/N}$, $F(z_k)$ reduces to the DFT. W governs the rate of spiral, A_o and θ_o determine the starting point radius and angle, and ϕ_o determines the interval spacing of the contour in the z-plane. Furthermore,

$$z_k^{-n} = A^{-n} W^{nk} \tag{C.10}$$

and by making use of the equality [105]

$$nk = \frac{n^2 + k^2 - (k-n)^2}{2} \tag{C.11}$$

the expression for $F(z_k)$ can be written as a convolution which can be evaluated by an FFT,

$$F(z_k) = \sum_{n=0}^{N-1} W^{k^2/2}(f(nT)A^{-n}W^{n^2/2})W^{-(k-n)^2/2}, \quad k = 0, 1 \ldots M-1 \qquad \text{(C.12)}$$

Define $g(n)$

$$g(n) = f(nT)A^{-n}W^{n^2/2} \qquad \text{(C.13)}$$

and exchange indices, then

$$F(z_k) = W^{n^2/2} \sum_{k=0}^{N-1} g(k)W^{-(n-k)^2/2}, \quad n = 0, 1 \ldots M-1 \qquad \text{(C.14)}$$

$W^{n^2/2}$ is a complex exponential with linearly increasing frequency. A similar waveform used in radar systems is referred to as a chirp signal, hence the name chirp-z transform [95, 96, 106, 107].

One disadvantage of this chirp-z method is that it may be slower than the fast Fourier transform. However, its strength lies in several advantages. The chirp-z transform is more flexible than the FFT in that it allows computing the transform along a more general contour. This contour can be a spiral which revolves in or out with respect to the origin, and it can lie closer to the poles of the system, improving the resolution of the poles. It can have an arbitrary starting point, and an arbitrary range. In comparison, the frequency range of the DFT is restricted by the sampling frequency. Additionally, as given in [96],

1. The number of time samples does not have to equal the number of samples of the z-transform.
2. Neither M nor N need be a power of 2.
3. The angular spacing of the z_k is arbitrary.

BIBLIOGRAPHY

BIBLIOGRAPHY

[1] J. Papapolymerou, J.-C. Cheng, J. East, and L. P. B. Katehi, "A micromachined high-Q X-band resonator," *IEEE Microwave and Guided Wave Letters*, vol. 7, no. 6, pp. 168–170, June 1997.

[2] J. F. Harvey and E. R. Brown, "Forward," *IEEE Trans.Microwave Theory and Tech.*, vol. 46, no. 11, pp. 1817–1819, November 1998.

[3] M. Yap, Y.-C. Tai, W. R. McGrath, and C. Walker, "Silicon micromachined waveguides for millimeter-wave and submillimeter-wave frequencies," in *Proc. of the 3rd International Symposium on Space Terahertz Technology*, Ann Arbor, MI, March 1992, pp. 316–323.

[4] I. C. Hunter, B. Jarry, and P. Guillon, "Microwave filters - applications and technology," *IEEE Trans. Microwave Theory and Tech.*, vol. 50, no. 3, pp. 794–805, March 2002.

[5] L. P. B. Katehi, G. M. Rebeiz, and C. T.-C. Nguyen, "MEMS and si-micromachined components for low-power, high-frequency communications systems," in *IEEE MTT-S Int. Microwave Symp. Dig.*, vol. 1, Baltimore, MD, June 1998, pp. 331–333.

[6] A. R. Brown, "High-Q integrated micromachined components for a 28 GHz front-end transceiver," Ph.D. dissertation, University of Michigan, Ann Arbor, MI, 1999.

[7] L. P. B. Katehi and P. Battacharya, "System on a chip proposal," University of Michigan, Ann Arbor, MI, Tech. Rep., August 1997.

[8] R. F. Drayton, "The development and characterization of self-packages using micromachining techniques for high-frequency circuit applications," Ph.D. dissertation, University of Michigan, Ann Arbor, MI, 1995.

[9] S. V. Robertson, "Micromachined W-band circuits," Ph.D. dissertation, University of Michigan, Ann Arbor, MI, 1997.

[10] K. J. Herrick, "W-Band three-dimensional integrated circuits utilizing silicon micromachining," Ph.D. dissertation, University of Michigan, Ann Arbor, MI, 2001.

[11] J. B. Muldavin, "High-isolation inductively-tuned X-band MEMS shunt switches," in *IEEE MTT-S Int. Microwave Symp. Dig.*, vol. 1, Boston, MA, June 2000, pp. 169–172.

[12] N. S. Barker, "Distributed MEMS transmission-line BPSK modulator," *IEEE Microwave and Guided Wave Letters*, vol. 10, no. 5, pp. 198–200, May 2000.

[13] A. Margomenos, S. Valas, M. I. Herman, and L. P. B. Katehi, "Isolation in three-dimensional integrated circuits," in *IEEE MTT-S Int. Microwave Symp. Dig.*, vol. 3, Boston, MA, June 2000, pp. 1875–1878.

[14] J. P. Becker, "Multilevel finite ground coplanar line transitions for high-density packaging using silicon micromachining," in *IEEE MTT-S Int. Microwave Symp. Dig.*, vol. 1, Boston, MA, June 2000, pp. 303–306.

[15] C. Kudsia and M. V. O'Donovan, "A light weight graphite fiber epoxy composite (GFEC) waveguide multiplexer for satellite systems," in *Proc. 4th European Microwave Conf.*, Montreaux, Switzerland, September 1973.

[16] J. D. Rhodes, "The generalized direct-coupled cavity linear phase filter," *IEEE Trans. Microwave Theory and Tech.*, vol. 18, no. 6, pp. 308–313, June 1970.

[17] S. J. Fiedziuszko, "Dual-mode dielectric resonator loaded cavity filters," *IEEE Trans. Microwave Theory and Tech.*, vol. 30, no. 9, pp. 1311–1316, September 1982.

[18] S. V. Robertson, L. P. B. Katehi, and G. M. Rebeiz, "W-Band microshield low-pass filters," in *IEEE MTT-S Int. Microwave Symp. Dig.*, June 1994, pp. 625–628.

[19] T. M. Weller, L. P. B. Katehi, and G. M. Rebeiz, "High performance microshield line components," *IEEE Trans. Microwave Theory and Tech.*, vol. 43, no. 3, pp. 534–543, March 1995.

[20] ——, "A 250-GHz microshield bandpass filter," *IEEE Microwave and Guided Wave Letters*, vol. 5, no. 5, pp. 153–155, May 1995.

[21] S. V. Robertson, L. P. B. Katehi, and G. M. Rebeiz, "Micromachined self-packaged W-band bandpass filters," in *IEEE MTT-S International Microwave Symposium Digest*, Orlando, FL, May 1995, pp. 1543–1546.

[22] T. M. Weller, K. J. Herrick, and L. P. B. Katehi, "Quasi-static design technique for mm-wave micromachined filters with lumped elements and series stubs," *IEEE Trans. Microwave Theory and Tech.*, vol. 45, no. 6, pp. 931–937, June 1997.

[23] D. M. Pozar, *Microwave Engineering*. Reading, MA: Addison-Wesley, 1990.

[24] P. Blondy, A. R. Brown, D. Cros, and G. M. Rebeiz, "Low-loss micromachined filters for millimeter-wave communication systems," *IEEE Trans. Microwave Theory and Tech.*, vol. 46, no. 12, pp. 2283–2288, December 1998.

[25] A. R. Brown and G. M. Rebeiz, "Micromachined micropackaged filter banks," *IEEE Microwave and Guided Wave Letters*, vol. 8, no. 4, pp. 158–160, April 1998.

[26] K. Takahashi *et al.*, "K-band receiver front-end IC integrating micromachined filter and flip-chip assembled active devices," in *IEEE MTT-S International Microwave Symposium Digest*, Anaheim, CA, June 1999, pp. 229–232.

[27] C.-Y. Chi and G. M. Rebeiz, "A low-loss 20 GHz micromachined bandpass filter," in *IEEE MTT-S Int. Microwave Symp. Dig.*, Orlando, FL, May 1995, pp. 1531–1534.

[28] A. R. Brown and L. Harle, "Integrated filters and diplexers," University of Michigan, JPL/CISM Advisory Meeting, Tech. Rep., August 1998.

[29] *HP85180A High-Frequency Structure Simulator, version 2.0.55*, Ansoft Corp., Pittsburgh, PA, 1999.

[30] *Advanced Design Systems 2002*, Agilent Technologies Corp., Palo Alto, CA, 2002, http://eesof.tm.agilent.com/.

[31] *Zeland's IE3D, version 5.01*, Zeland Software, Fremont, CA, 1998.

[32] *Picoprobe*, GGB Industries, Naples, FL, www.ggb.com.

[33] "Product Note 8510-8A - Agilent network analysis applying the 8510 TRL calibration for non-coaxial measurements," Agilent Technologies Corp., 2000, Palo Alto, CA.

[34] R. B. Marks and D. F. Williams, *Multical v1.00*, NIST, Boulder, CO, August 1995.

[35] R. B. Marks, "A multiline method of network analyzer calibration," *IEEE Trans. Microwave Theory and Tech.*, vol. 39, no. 7, July 1991.

[36] G. T. A. Kovacs, *Micromachined Transducers Sourcebook*. WCB/McGraw Hill, 1998.

[37] J. P. Becker, "Silicon micromachined waveguide transitions and three-dimensional lithography for high frequency packaging," Ph.D. dissertation, University of Michigan, Ann Arbor, MI, 2001.

[38] *Reactive Ion Etcher System*, Surface Technology Systems Ltd., Newport, UK, www.stsystems.com.

[39] J. P. Becker, Y. Lee, J. R. East, and L. P. B. Katehi, "A finite ground coplanar line-to-silicon micromachined waveguide transition," *IEEE Trans. Microwave Theory and Tech.*, vol. 49, no. 10, pp. 1671–1676, October 2001.

[40] A. A. Ayón, "Time-multiplexed deep etching," *IEEE Trans. Microwave Theory and Tech.*, vol. 49, no. 10, pp. 1671–1676, October 2001.

[41] H. Ashraf, J. K. Bhardwaj, S. Hall, J. Hopkins, A. M. Hynes, I. Johnston, S. Mcauley, G. Nicholls, L. Atabo, M. E. Ryan, and S. Watcham, "Advances in deep anisotropic silicon etch processing for MEMS," Surface Technology Systems Ltd., Newport, UK, Tech. Rep., 2000.

[42] J. K. Bhardwaj, H. Ashraf, and A. McQuarrie, "Dry silicon etching for MEMS," in *Symp. on Microstructures and Microfabricated Sys.* Montreal, CA: Electrochemical Society, May 1997.

[43] T. Ellis, J.-P. Raskin, L. P. B. Katehi, and G. M. Rebeiz, "A wideband CPW-to-microstrip transition for millimeter-wave packaging," in *IEEE MTT-S Int. Microwave Symp. Dig.*, vol. 2, Anaheim, CA, June 1999, pp. 629–632.

[44] K. C. Gupta, R. Garg, I. Bahl, and P. Bhartia, *Microstrip Lines and Slotlines*, 2nd ed. Norwood, MA: Artech House, 1996.

[45] S. B. Cohn, "Slotline on a dielectric substrate," *IEEE Trans. Microwave Theory and Tech.*, vol. 17, pp. 768–778, 1969.

[46] T. E. van Deventer, "Characterization of two-dimensional high frequency microstrip and dielectric interconnects," Ph.D. dissertation, University of Michigan, Ann Arbor, MI, 1992.

[47] A. R. Brown, December 2002, Radiation Laboratory, University of Michigan, personal communication.

[48] A. R. Brown, P. Blondy, and G. M. Rebeiz, "Microwave and millimeter-wave high-Q micromachined resonators," *Int. J. on RF and Microwave CAE*, vol. 9, pp. 326–337, 1999.

[49] L. Harle, J. Papapolymerou, J. East, and L. P. B. Katehi, "The effects of slot positioning on the bandwidth of a micromachined resonator," in *Proc. 28th European Microwave Conference*, vol. 2, Amsterdam, NE, October 1998, pp. 664–666.

[50] L. Harle and L. P. B. Katehi, "A vertically integrated micromachined filter," *IEEE Trans. Microwave Theory and Tech.*, vol. 50, no. 9, pp. 2063–2068, September 2002.

[51] G. P. Gauthier, L. P. B. Katehi, and G. M. Rebeiz, "W-Band finite ground coplanar waveguide (FGCPW) to microstrip line transition," in *IEEE MTT-S Int. Microwave Symp. Dig.*, vol. 1, Baltimore, MD, June 1998, pp. 107–109.

[52] D. Pavlidis and H. L. Hartnagel, "The design and performance of three-line microstrip couplers," *IEEE Trans. Microwave Theory and Tech.*, vol. 24, no. 10, pp. 631–640, October 1976.

[53] S. Yamamoto, T. Azakami, and K. Itakura, "Coupled strip transmission line with three center conductors," *IEEE Trans. Microwave Theory and Tech.*, vol. 14, no. 10, pp. 446–461, October 1966.

[54] N. L. VandenBerg and L. P. B. Katehi, "Broadband vertical interconnects using slot-coupled shielded microstrip lines," *IEEE Trans. Microwave Theory and Tech.*, vol. 40, no. 1, pp. 81–88, January 1992.

[55] J.-C. Cheng, N. I. Dib, and L. P. B. Katehi, "Theoretical modeling of cavity-backed patch antennas using a hybrid technique," *IEEE Trans. Antennas and Propagation*, vol. 43, no. 9, pp. 1003–1013, September 1995.

[56] D. M. Pozar and S. D. Targonski, "Improved coupling for aperture coupled microstrip antennas," *Electronics Letters*, vol. 27, no. 13, pp. 1129–1131, June 1991.

[57] R. F. Harrington, *Time-Harmonic Electromagnetic Fields.* McGraw-Hill, 1961.

[58] R. E. Collin, *Foundations for Microwave Engineering.* New York: McGraw Hill, 1992.

[59] W. R. McGrath, C. Walker, M. Yap, and Y.-C. Tai, "Silicon micromachined waveguides for millimeter-wave and submillimeter-wave frequencies," *IEEE Microwave and Guided Wave Letters*, vol. 3, no. 3, pp. 61–63, March 1993.

[60] S. V. Robertson, L. P. B. Katehi, and G. M. Rebeiz, "Micromachined W-band filters," *IEEE Trans. Microwave Theory and Tech.*, vol. 44, no. 4, pp. 598–606, April 1996.

[61] C.-Y. Chi and G. M. Rebeiz, "Conductor-loss limited stripline resonator and filters," *IEEE Trans. Microwave Theory and Tech.*, vol. 44, no. 4, pp. 626–630, April 1996.

[62] R. F. Drayton, R. M. Henderson, and L. P. B. Katehi, "Monolithic packaging concepts for high isolation in circuits and antennas," *IEEE Trans.Microwave Theory and Tech.*, vol. 46, no. 17, pp. 900–906, July 1998.

[63] G. Matthaei, L. Young, and E. M. T. Jones, *Microwave Filters, Impedance-Matching Networks, and Coupling Structures.* New York: McGraw-Hill, 1964.

[64] J. Helszajn, *Synthesis of Lumped Element, Distributed and Planar Filters.* Berkshire, UK: McGraw-Hill, 1990.

[65] K. A. Zaki and C. Chen, "Coupling of non-axially symmetric hybrid modes in dielectric resonators," *IEEE Trans. Microwave Theory and Tech.*, vol. 35, no. 12, pp. 1136–1142, December 1987.

[66] N. A. McDonald, "Electric and magnetic coupling through small apertures in shield walls of any thickness," *IEEE Trans. Microwave Theory and Tech.*, vol. 20, no. 10, pp. 689–695, October 1972.

[67] E. L. Ginzton, *Microwave Measurements*. New York: McGraw-Hill, 1957.

[68] *EV501 Wafer Bonding System*, Electronic Visions Group, Shaerding, Austria, www.ev-global.com.

[69] K. J. Herrick and L. P. B. Katehi, "RF W-band wafer-to-wafer transition," *IEEE Trans. Microwave Theory and Tech.*, vol. 49, no. 4, pp. 600–608, April 2001.

[70] S. Wolf and R. N. Tauber, *Silicon Processing for the VLSI Era: Volume 1 - Process Technology*. Sunset Beach, CA: Lattice Press, 1986.

[71] S. Wolf, *Silicon Processing for the VLSI Era: Volume 2 - Process Integration*. Sunset Beach, CA: Lattice Press, 1990.

[72] M. Hill, J. Papapolymerou, and R. Ziolkowski, "High-Q micromachined resonant cavities in a K-band diplexer configuration," *IEE Proceedings - Microwaves, Antennas and Propagation*, vol. 148, no. 5, pp. 307–312, October 2001.

[73] J.-F. Liang, X.-P. Liang, K. A. Zaki, and A. E. Atia, "Dual-mode dielectric or air-filled rectangular waveguide filters," *IEEE Trans. Microwave Theory and Tech.*, vol. 42, no. 7, pp. 1330–1336, July 1994.

[74] H.-C. Chang and K. A. Zaki, "Evanescent-mode coupling of dual-mode rectangular waveguide filters," *IEEE Trans. Microwave Theory and Tech.*, vol. 39, no. 8, pp. 1307–1312, August 1991.

[75] Duke Scientific Corp., Palo Alto, CA, www.dukescientific.com.

[76] *Microwave Plasma Systems*, TePlaAG, Hans-Riedl-Str. 5, D-85622 Feldkirchen, www.tepla.com.

[77] D. Kajfez, "Q-factor measurement techniques," *RF Design*, pp. 56–68, August 1999.

[78] J. R. Pierce, "Guided-wave frequency range transducer," January 1953, U.S. Patent 2,626,990.

[79] R. M. Kurzrok, "General three-resonator filters in waveguide," *IEEE Trans. Microwave Theory and Tech.*, vol. 14, no. 1, pp. 46–47, January 1966.

[80] ——, "General four-resonator filters at microwave frequencies." *IEEE Trans. Microwave Theory and Tech.*, vol. 14, no. 6, pp. 295–296, June 1966.

[81] E. C. Johnson, “New developments in designing bandpass filters,” *Electron. Ind.*, pp. 87–94, January 1964.

[82] J. D. Rhodes, “The theory of generalized interdigital networks,” *IEEE Trans. Circuit Theory*, vol. 16, no. 8, pp. 280–288, August 1969.

[83] ——, “A low-pass prototype network for microwave linear phase filters,” *IEEE Trans. Microwave Theory and Tech.*, vol. 18, no. 6, pp. 290–301, June 1970.

[84] ——, “The generalized interdigital linear phase filter,” *IEEE Trans. Microwave Theory and Tech.*, vol. 18, no. 6, pp. 301–307, June 1970.

[85] A. E. Atia and A. E. Williams, “Narrow-bandpass waveguide filters,” *IEEE Trans. Microwave Theory and Tech.*, vol. 20, no. 4, pp. 258–265, April 1972.

[86] ——, “Non-minimum-phase optimum-amplitude bandpass waveguide filters,” *IEEE Trans. Microwave Theory and Tech.*, vol. 22, no. 4, pp. 425–431, April 1974.

[87] A. E. Williams, “A four-cavity elliptic waveguide filter,” *IEEE Trans. Microwave Theory and Tech.*, vol. 18, no. 12, pp. 1109–1114, December 1970.

[88] R. Levy and S. B. Cohn, “A history of microwave filter research, design and development,” *IEEE Trans. Microwave Theory and Tech.*, vol. 32, no. 9, pp. 1055–1067, September 1984.

[89] S.-J. Jao, R. R. Bonette, and A. E. Williams, “Generalized dual-plane multicoupled line filters,” *IEEE Trans. Microwave Theory and Tech.*, vol. 41, no. 12, pp. 2182–2189, December 1993.

[90] J.-F. Liang, K. A. Zaki, and R. Levy, “Dual-mode dielectric-loaded resonators with cross-coupling flats,” in *IEEE MTT-S Int. Microwave Symp. Dig.*, vol. 2, Orlando, FL, May 1995, pp. 509–511.

[91] R. Levy, “Filters with single transmission zeros at real or imaginary frequencies,” *IEEE Trans. Microwave Theory and Tech.*, vol. 24, no. 4, pp. 172–181, April 1976.

[92] ——, “Generalized rational function approximation in finite intervals using Zolotarev functions,” *IEEE Trans. Microwave Theory and Tech.*, vol. 18, no. 12, pp. 1052–1064, December 1970.

[93] “Application Note 1287-8: Simplified filter tuning using time domain,” Agilent Technologies Corp., 2001, Palo Alto, CA.

[94] “Application Note 1287-10: Advanced filter tuning using time domain transforms,” Agilent Technologies Corp., 2001, Palo Alto, CA.

[95] R. G. Huenemann, “Bandlimited Iinterpolation,” www.flash.net/bobgh/bandlimited.htm.

[96] L. R. Rabiner, R. W. Schafer, and C. M. Rader, "The chirp-z transform algorithm and its application," *Bell System Technical Journal*, vol. 48, no. 5, pp. 1249–1292, May-June 1969.

[97] *HP 8753C Vector Newtork Analyzer Manual*, Hewlett-Packard Co., 1989.

[98] D. Peroulis, February 2003, Radiation Laboratory, University of Michigan, personal communication.

[99] J. A. G. Malherbe, *Microwave Transmission Line Filters.* Norwood, MA: Artech House, 1979.

[100] S. B. Cohn, "Microwave bandpass filters containing high-Q dielectric resonators," *IEEE Trans. Microwave Theory and Tech.*, vol. 16, no. 4, pp. 218–227, April 1968.

[101] A. Bailey, W. Foley, M. Hageman, C. Murray, A. Piloto, K. Sparks, and K. Zaki, "Miniature LTCC filters for digital receivers," in *IEEE MTT-S Int. Microwave Symp. Digest*, vol. 2, Denver, CO, June 1997, pp. 999–1002.

[102] S. Q. Scrantom, J. C. Lawson, and L. Liu, "LTCC technology: where we are and where we're going II," in *IEEE MTT-S Int. Topical Symp. on Technologies for Wireless Applications*, Vancouver, Canada, February 1999, pp. 193–200.

[103] C.-H. Lee, S. Chakrabory, A. Sutono, S. You, D. Heo, and J. Laskar, "Broadband highly integrated LTCC front-end module for IEEE 902.11a WLAN applications," in *IEEE MTT-S Int. Microwave Symp. Digest*, vol. 2, Seattle, WA, June 2002, pp. 1045–1048.

[104] H. J. Blinchikoff and A. I. Zverev, *Filtering in the Time and Frequency Domains.* New York: Wiley and Sons, 1976.

[105] L. I. Bluestein, "A linear filtering approach to the computation of the Discrete Fourier Transform," *1968 Northeast Electronics Research and Engineering Meeting Record*, no. 10, pp. 218–219, November 1968.

[106] L. R. Rabiner and B. Gold, *Theory and Application of Digital Signal Processing.* Englewood Cliffs, NJ: Prentice-Hall, 1975.

[107] W. D. Oliver, "The Singing Tree: A novel interactive musical interface," Master's thesis, Massachusetts Institute of Technology, Cambridge, MA, 1997.